Tailoring of Magnetic Anisotropy and Interfacial Spin Dynamics



Alexander Baker

Wadham College

University of Oxford

A thesis submitted for the degree of

Doctor of Philosophy

Hilary 2016

Abstract

Spin transfer in magnetic multilayers offers the possibility of a new generation of ultra-fast, low-power spintronic devices. New ways to control the resonance frequency and damping in ultrathin films are actively sought, fuelling study of the precessional dynamics and interaction mechanisms in such samples. One effect that has come under particular scrutiny in recent years is the spin-transfer torque, wherein a flow of spins entering a ferromagnet exerts a torque on the magnetisation, inducing precession. A flow of spin angular momentum is usually generated through a spin-polarised electrical current, but a promising alternative is the pure spin current emitted by a ferromagnet undergoing ferromagnetic resonance (FMR). This allows spins to be transferred without a net charge flow. The physics of the generation, transmission and absorption of pure spin currents is a developing field, and holds great promise for both industrial applications and as a means to study fundamental physical phenomena in exotic materials.

This thesis presents an investigation into the magnetodynamics of ferromagnetic thin films and heterostructures grown by molecular beam epitaxy and studied using vector-network analyser ferromagnetic resonance (VNA-FMR), x-ray magnetic circular dichroism, vibrating sample magnetometry and x-ray detected ferromagnetic resonance (XFMR). Particular attention is paid to the anisotropy of damping processes that occur in thin films, and the different coupling mechanisms that can exist across non-magnetic spacer layers in spin valves and magnetic tunnel junctions.

It is first shown that the static and dynamic magnetic properties of thin Fe films can be effectively tailored by dilute doping with Dy impurities, which introduces a sizeable anisotropy of Gilbert damping. The mechanism underlying this effect is discussed, as is the concurrent modification of the spin and orbital contributions to the magnetic moment.

The focus then turns to magnetodynamics of ferromagnetic films coupled across a nonmagnetic spacer layer, examining how different materials permit different interactions. First, an insulating MgO layer is used to separate the FM layers; it is found that this attenuates a spin current in under 1 nm, but permits a static interaction for at least 2 nm. XFMR measurements are used to ascertain the different contributions of the two interactions, and shed light on their interplay. Next, the same techniques are applied to spin valves with a spacer layer of the topological insulator (TI) Bi_2Se_3. TIs are the subject of much attention in the physics community, as they hold the potential for dissipationless transport, extremely high spin-orbit torques, and a host of novel physical effects. Here, their ability to absorb and transmit a pure spin current is studied, testing their suitability for incorporation into existing device schemata. VNA-FMR measurements confirm that the TI functions as an efficient angular momentum sink. XFMR measurements, however, demonstrate the presence of a weak interaction between the two ferromagnets, able to persist up to at least 8 nm, and possibly mediated by the topological surface state.

Finally, the angle-dependence of spin pumping through a Cr barrier is examined, finding that a strong anisotropy of spin pumping from the source layer can be induced by an angular dependence of the total Gilbert damping parameter in the spin sink layer. VNA-FMR measurements show that anisotropy is suppressed above the spin diffusion length in Cr, which is found to be 8 nm, and is independent of static exchange coupling in the spin valve. XFMR results confirm induced precession in the spin sink layer, with isotropic static exchange and an anisotropic dynamic exchange.

Taken together, these studies provide an insight not only into the magnetisation dynamics of thin films (and ways to modify them) but a demonstration of the power of ferromagnetic resonance techniques, and their applicability across materials and concepts. The results offer valuable information on the transmission and absorption of spin currents by different materials, and several mechanisms by which enhanced spin torques and angular control of damping may be realized for next-generation spintronic devices.

For Meghan

This is not a story of incredible heroism, or merely the narrative of a cynic; at least I do not mean it to be. It is a glimpse of several lives that ran parallel for a time, with similar hopes and convergent dreams. – Ernesto Guevara

Acknowledgements

A thesis is by its nature a collaborative endeavour, and I have been extremely fortunate as regards the company in which I have found myself. Anything of merit contained within these pages can be attributed to the exceptional colleagues, collaborators, and friends I have had along the way; any mistakes are entirely my own.

First thanks must, of course, go to my supervisors: Professors Thorsten Hesjedal and Gerrit van der Laan. They have guided my research at macro and micro levels, provided me with innumerable opportunities to learn, and been excellent company to boot. Thorsten is to be thanked in particular for training me in the operation of the LaMBE in the Clarendon. We spent many hours struggling with its peculiarities and personality quirks, it is probably remarkable that all three of us are still standing at the end of it. Gerrit has been a constant source of advice and aid on beamtimes, and discussions with him on the subject of static and dynamic interactions lead directly into the work presented in chapters 6 and 8. For this and so much more, my thanks to both of them.

Throughout my research, Dr. Adriana Figueroa-Garcia has provided incomparable support. Whether it be improving our measurement kit, advising me on how to interpret and present data, or chasing down problems at 2 am on a beamtime, I could not have asked for a more supportive post-doc to work with. I must also thank Dr. Leigh Shelford, who first taught me the fundamentals of FMR, and who provided excellent company on many XFMR beamtimes.

The staff of beamline I10 have allowed me to make it a home from home. Dr. Paul Steadman, Dr. Alexey Dobrynin, Dr Peter Bencok, and Dr. David Burn have provided able and friendly assistance, as well as letting me use their SQUID-VSM. Mark Sussmuth must be singled out from this group, for his peerless technical support and good humour. At the ALS in Berkeley, Prof. Elke Arenholz, Dr. Padraic Shafer and Dr. Alpha N'Diaye always had huge smiles and were willing to help

at the most unsociable hours. For their assistance on XFMR beamtimes, I must also thank Dr. Stuart Cavill, Chris Love, Dr. Gavin Stenning, and Rob Valkass. I also thank the staff of I05, in particular Dr. Moritz Hoesch and Jon Riley, for hosting the μ-MBE in their rooms and helping with numerous maintenance tasks.

In the office and the lab I have shared the travails with some good friends: (Dr.) Liam Collins-McIntyre, Shilei Zhang, Piet Schönherr, Liam Duffy and (Dr.) Sara Harrison. Always standing by with a helping hand or a joke, I could not have asked for better labmates. Though I was not there as much as I would have liked, the fine people of the Clarendon lab were likewise excellent company at coffee and tea, and took the bizarre confections I brought in with, if not actual relish, good-humoured resignation.

I must thank my parents, Deb and Adrian, for their varied and unstinting support, and for instilling what work ethic I can claim to have. Finally, I thank Meghan for her unquestioning and unequalled support in so many ways, and for being so understanding of the fractured schedule my studies have required me to keep. I could not have done this without her, and would not care to have tried.

Contents

1 Introduction **1**

1.1 Magnetism of Thin Films and Heterostructures 1

1.2 Why Ferromagnetic Resonance? 3

1.3 Outline of the Thesis 5

2 Theoretical Background **7**

2.1 Basic Energy Terms of Ferromagnetism 7

2.1.1 Exchange Energy 9

2.1.2 Demagnetisation Energy 10

2.1.3 Magnetocrystalline Anisotropy Energy 11

2.1.4 Zeeman Energy 12

2.2 Magnetisation Dynamics 12

2.2.1 The Landau-Lifshitz-Gilbert Equation 13

2.2.2 Equilibrium Orientation of Magnetisation 14

2.2.3 The Resonance Condition 16

2.2.4 Static Exchange Coupling 18

2.3 Magnetisation Damping 19

2.3.1 Gilbert Damping 19

2.3.2 Non-Gilbert Damping 20

2.3.3 Spin Pumping 21

2.4 X-Ray Magnetic Circular Dichroism 25

2.4.1 Sum Rules 26

3 Experimental Techniques **30**

3.1 Molecular Beam Epitaxy 30

3.1.1 Reflection High Energy Electron Diffraction 37

3.2 Vector-Network Analyser Ferromagnetic Resonance 40

3.3 SQUID Vibrating Sample Magnetometry 43

3.4 X-Ray Magnetic Circular Dichroism 46

3.5 X-Ray Detected Ferromagnetic Resonance 48

4 Engineering of Magnetic Properties using Rare Earth Dopants 54
4.1 Motivation 54
4.2 Sample Fabrication 56
4.3 Magnetometry and Magetocrystalline Anisotropy Parameters 58
4.4 Angle-Dependent Gilbert Damping 60
4.5 Determination of Spin and Orbital Magnetic Moments 63
4.6 Conclusion 65

5 Micromagnetic Modelling of Coupled Magnetodynamics 67
5.1 Motivation 67
5.2 OOMMF 68
5.2.1 Simulating FMR 69
5.2.2 Isolated Layers 70
5.2.3 Coupled Layers 71
5.3 Determination of the AC Magnetic Susceptibility Tensor 76
5.3.1 Dynamic Susceptibility of an Isolated Layer 76
5.3.2 Modelling Dynamic and Static Exchange 81
5.4 Conclusion 85

6 Suppression of Spin Pumping by an Insulating Barrier 87
6.1 Motivation 87
6.2 Sample Fabrication 88
6.3 Static Exchange Coupling 89
6.4 Structural Characterisation of the MgO Barriers 92
6.5 VNA-FMR Measurements of Gilbert Damping 94
6.6 Layer Resolved Magnetodynamics 97
6.7 Conclusion 100

7 Spin Pumping in Topological Insulators 102
7.1 Motivation 102
7.1.1 What is a Topological Insulator? 104
7.2 Sample Fabrication 106
7.3 Coupling Across a Topological Insulator 109
7.3.1 Gilbert Damping as a Function of TI Thickness 109
7.3.2 Layer-Resolved Magnetodynamics 112
7.4 Anti-Damping Torques from Simultaneous Resonance 117

7.4.1 Vector Network Analyser Measurements . . . 119
7.4.2 Layer-Resolved Measurements . . . 122
7.5 Temperature Dependence of Spin Pumping . . . 124
7.6 Conclusion . . . 126

8 Anisotropy Imprinting Through Spin Pumping 128
8.1 Motivation . . . 128
8.1.1 Angular Control of Spin Pumping . . . 129
8.2 Sample Fabrication . . . 131
8.3 Determining the Static Exchange . . . 131
8.4 Spin Pumping Through a Cr Barrier . . . 136
8.4.1 Attenuation of a Pure Spin Current in Cr . . . 137
8.4.2 Angular Dependence of Spin Pumping . . . 137
8.5 Layer-Resolved Magnetodynamics . . . 141
8.6 Conclusion . . . 145

9 Conclusion 147
9.1 Summary of Results . . . 148
9.2 Perspective and Outlook . . . 150

A Derivation of the AC Magnetic Susceptibility with Static and Dynamic Exchange Coupling 152

B List of of Abbreviations and Acronyms 159

C Publications Arising from this Work 161

References 164

List of Figures

2.1 Diagram of Thin Film Coordinate System 9
2.2 Schematic of Precession of Magnetisation 13
2.3 Magnetic Susceptibility Across Resonance 17
2.4 Illustration of Spin Pumping 22
2.5 Schematic of the X-ray Magnetic Circular Dichroism Effect 27

3.1 Photographs of the LaMBE 33
3.2 Photograph of the μ-MBE 34
3.3 Cutaway view of the μ-MBE growth chamber 35
3.4 Picture of an Effusion cell 36
3.5 Diagram of an Electron Beam Evaporator 37
3.6 Schematic of a RHEED Gun 38
3.7 RHEED Patterns of $Co_{50}Fe_{50}$ 40
3.8 Schematic of VNA-FMR Setup 41
3.9 Photographs of the Portable Octupole Magnet System 42
3.10 Example Kittel Curves 44
3.11 SQUID-VSM Operating Principle 45
3.12 Schematic of the XFMR Experimental Setup 50

4.1 RHEED Images of Thin Fe Film Doped with Dy 57
4.2 XRD Measurement of a Thin Fe Film Doped with Dy 58
4.3 Hystersis Loops of Dy-doped Fe Thin Films 59
4.4 Angular Dependence of Resonance Field for Dy-doped Fe 60
4.5 Angular Variation of Gilbert Damping for Dy-doped Fe 61
4.6 XAS and XMCD Spectra for Dy-doped Fe 64
4.7 Calculated Spin and Orbital Moments as a Function of Dy Content 65

5.1 Precession of Magnetisation and Associated FMR Spectrum 70
5.2 Micromagnetic Simulation of a CoFe Film 71
5.3 FMR Spectrum of a Weakly Coupled CoFe/NiFe Bilayer 72

5.4 Kittel Curves for a CoFe/NiFe Bilayer 73
5.5 FMR Spectra of an Exchange-Coupled CoFe/NiFe Bilayer 74
5.6 Resonances Plotted Across the Depth of the Bilayer 75
5.7 Dynamic Susceptibility of an Iron Thin Film 79
5.8 Static Coupling: Amplitude and Phase of Precession 83
5.9 Dynamic Coupling: Amplitude and Phase of Precession 84
5.10 Combined Effects of Static and Dynamic Coupling 85

6.1 Hysteresis loops of Trilayers with MgO Spacers 90
6.2 XMCD Hysteresis loops of Trilayers with MgO Spacers 91
6.3 Static Exchange Coupling in MgO Trilayers 92
6.4 Structural Characterisation of the MTJs 94
6.5 Gilbert Damping as a Function of MgO Thickness 95
6.6 Amplitude and Phase of Precession for $t_{\mathrm{MgO}} = 1$ nm 97
6.7 Amplitude and Phase of Precession for $t_{\mathrm{MgO}} = 2$ nm 99

7.1 Bandstructure of a Topological Insulator 105
7.2 Ferromagnet-Topological Insulator-Ferromagnet Heterostructure . . 107
7.3 Angular Dependence of Resonance of TI-FM Heterostructure 108
7.4 Gilbert Damping as a Function of TI layer Thickness 111
7.5 Precession of Ni Magnetisation Across Resonance at 4 GHz 113
7.6 Amplitude and Phase of Precession for $t_{\mathrm{TI}} = 4$, 8 nm 114
7.7 Amplitude and Phase of Precession for $t_{\mathrm{TI}} = 20$ nm 115
7.8 Evolution of Overlapping Resonances 118
7.9 Outline of Fitting of Overlapping Resonances. 120
7.10 Resonant Linewidths as a Function of Mode Separation: VNA-FMR 121
7.11 Overlapping Resonances Measured by XFMR 123
7.12 Resonant Linewidths as a Function of Mode Separation: XFMR . . 124
7.13 Gilbert Damping as a Function of Temperature 126

8.1 Hysteresis Loops of Cr Spin Valves 132
8.2 XMCD Hysteresis Loops of Cr Spin Valves 133
8.3 Example Kittel Curves of Cr Spin Valves 134
8.4 Fitted VNA-FMR Data of Cr Spin Valves 136
8.5 Spin Pumping as a Function of Cr Thickness 138
8.6 Decay Gilbert Damping Along the Easy and Hard Axes 139
8.7 Gilbert Damping as a Function of External Field Angle 140
8.8 Amplitude and Phase of Precession for $t_{\mathrm{Cr}} = 1$ nm 142

8.9 Angle-Resolved Phase of Precession of CoFe for $t_{\mathrm{Cr}} = 1$ nm 143
8.10 Fitted Phase Variation Across Resonance 144

Chapter 1

Introduction

1.1 Magnetism of Thin Films and Heterostructures

Throughout the twentieth century electronic devices revolutionised our way of life and lead to a heady pace of technological change. More recently the demand for ever-faster device operation and ever-greater memory capacity has driven the magnetics community to search for new physical concepts and device schemata that exploit them. Leaving behind "electronics", technologies based on the charge of the electron, the emerging paradigm is "spintronics" [1, 2], technologies incorporating the spin of the electron, a quantum property that promises faster, more stable and ever smaller devices.

Perhaps the first true spintronic innovation was the discovery of giant magnetoresistance (GMR) in 1988 [3, 4], earning Albert Fert and Peter Grünberg the 2007 Nobel prize. Together with the subsequent discovery of tunneling magnetoresistance in magnetic tunnel junctions (MTJs) [5], the first spin valve read heads and magnetic random access memory (MRAM) devices were developed [6, 7]. Data

storage has been revolutionised by these concepts, as the drive for miniaturisation leads to ever-greater information densities. A wide variety of mechanisms to write data have been proposed, including heat assisted MRAM [8] and magnetic switching [9, 10], but perhaps the most promising is the use of spin-transfer torque (STT) [11–13]. When a spin polarised current is passed through a magnet, the interaction of the angular momentum of the flowing electrons with the static magnetisation exerts a torque, inducing precession. If this torque is sufficiently large it can reverse the magnetisation, rewriting stored data [10]. This provides one motivation for the study of magnetodynamics and interfacial spin dynamics in heterostructures.

A second motivation arises from the need for faster and faster write operations. As the speed of device operation increases to the GHz range, the magnetic relaxation properties of the system become important [14, 15]. Energy loss mechanisms arising from spin orbit coupling [14], sample imperfections [16, 17], interactions with impurities or dopants [18, 19], and even the ejection of spins into neighbouring layers must be considered [20–23]. High quality thin film samples are required for such studies, as they allow experiments to access the intrinsic properties of such processes in a controlled environment. The use of single crystal samples also allows one to study the angular variation of damping mechanisms, studying how they can relate to the lattice, the co-ordination of defects or the magnetocrystalline anisotropy [16]. Comparatively little work exists to date on such effects, but if the anisotropy of damping can be tailored it offers new possibilities for device optimisation, as well as revealing deeper information about the underlying magnetic relaxation mechanisms.

This thesis presents an investigation of the magnetodynamics of thin films grown by molecular beam epitaxy (MBE) and studied by vector-network analyser ferromagnetic resonance (VNA-FMR), x-ray magnetic circular dichroism (XMCD),

vibrating sample magnetometry (VSM) and x-ray detected ferromagnetic resonance (XFMR). High quality samples consisting of single layers or trilayers based on ferromagnet – non-magnet – ferromagnet structures were grown on MgO (001) substrates. These samples were used to study coupling across non-magnetic barriers, paying attention to how they can be modified, and the angle-dependent damping processes that arise.

Throughout this research the goal has been to study how the anisotropy of magnetodynamics might be manipulated, and how two magnetic layers separated by a spacer layer interact and influence one another. Though they appear separate concepts, they can be studied in the same way, and by the final chapter it will be shown that they can come together to yield valuable insights into spin transfer and coupled magnetodynamics. While the research has been conducted from a perspective of basic science, aiming to understand the fundamental physics driving the observations, every effort has been made to ensure that work is directed in technologically relevant channels, and to contextualise the findings in their potential for device applications.

1.2 Why Ferromagnetic Resonance?

It is important to consider not just why this investigation was performed, but also why a specific approach was chosen. Here, broadband VNA-FMR was widely used as both a standard characterisation technique to check the quality of samples, and as a detailed probe of magnetodynamics and spin transfer. The question is then what advantages are unique to broadband FMR over, for example, SQUID magnetometry (which is employed here in a supportive role) [24], inverse spin Hall effect (ISHE) [25, 26] or magnetotransport techniques [27]?

The key advantage offered by broadband FMR is its versatility. Few other tech-

niques can offer such powerful characterisation of both static and dynamic magnetic properties [28], especially when the extension of x-ray detection is incorporated [15,29]. Further, it does not require patterning of samples into measurement geometries such as Hall bars, or the application of electrical contacts to the sample surface. In this way, VNA-FMR has a high-throughput, is non-destructive and uses samples with other standard characterisation techniques.

When studying the coupling mechanisms between magnetic layers in a heterostructure, the choice of technique also determines which interactions are accessible. While many magnetic measurement techniques can detect the presence of a static coupling, for example through a change in the shape of the hysteresis loop [30] or a shift in resonance field [31, 32], the dynamic interaction of spin pumping occurs when the magnetic layer is precessing, most commonly when the resonance condition is fulfilled [22]. FMR-based techniques such as VNA-FMR, or ISHE are therefore required. ISHE is a sensitive technique, as in measuring the voltage induced by the absorption of spins it is a direct probe of the presence of spin pumping [25, 33]. VNA-FMR, in contrast can only indirectly measure spin pumping, and does not provide layer-specific information as it averages over the whole stack. This limitation is alleviated, however, by performing XFMR [29, 34]. This technique will be explored in more detail in section 3.5, but in brief it uses an experimental configuration similar to VNA-FMR, in combination with a synchrotron light source, to perform a time-resolved version of x-ray magnetic circular dichroism. This allows layer-resolved measurements of the amplitude and phase of precession. The high degree of temporal and spatial resolution yields information unavailable to few other techniques, allowing, for example, separation of different coupling mechanisms [15,28,32,35] or clean measurements of overlapping resonances [15, 28].

Broadband FMR is a technique in which conceptual and experimental simplicity

are combined with with high sensitivity and straightforward extension to more advanced measurements. It is well-suited to study the effects of magnetic anisotropy on magnetodynamics, offering insights into how these traits might be tailored and optimised towards spintronic applications. It allows precise determination of the strength and nature of coupling mechanisms in magnetic heterostructures and, by extension into XFMR, the interfacial spin dynamics induced by long-range interactions.

Beyond VNA-FMR, other characterisation techniques were employed to confirm findings or provide additional information. By measuring hysteresis loops, VSM provides an alternative measure of saturation magnetisation and coupling in trilayers [28, 30], as well as probing magnetocrystalline anisotropy. A significant portion of the research presented here was conducted at synchrotrons, sources of intense, coherent light of tunable energy and polarisation [36]. This affords an element-specific probe of magnetisation through XMCD [37, 38], as well as allowing determination of the relative contributions of spin and orbital angular momentum [39, 40].

1.3 Outline of the Thesis

The investigation presented in this thesis focuses on methods to manipulate the anisotropy and spin transfer properties of ferromagnetic thin films and heterostructures. The aim is to present a comprehensive, multi-technique study of the spin dynamics of a variety of systems, utilising both lab and synchrotron methods to develop a thorough understanding of the underlying physics. All samples were grown by the author (with the exception of the topological insulator layers used in chapter 7) using molecular beam epitaxy. The primary technique employed throughout the research was ferromagnetic resonance, used to determine both

static and dynamic magnetic properties, with particular attention paid to Gilbert damping and spin pumping in spin valves. The work is presented as a series of individual projects, linked by the common theme of magnetodynamics and spin transfer.

Chapter 2 gives an introduction to the pertinent theory, paying particular attention to the mechanisms underlying ferromagnetic resonance and the spin pumping effect, along with a more general background on magnetism in thin films and the x-ray magnetic circular dichroism effect. Building on this foundation, chapter 3 details the experimental techniques used to fabricate and study the samples. Chapter 4 concerns a study of how dilute Dy doping of Fe thin films can modify the angular dependence of Gilbert damping. Chapter 5 gives further detail on the modelling used throughout the thesis, in particular how exchange-coupled multilayers can be simulated. From this, chapter 6 studies the coupled magnetodynamics of ferromagnetic layers separated by a thin MgO barrier, studying the suppression of spin pumping by an insulating layer. Chapter 7 is dedicated to a study of spin pumping in the novel materials class of topological insulators, aiming to exploit the exotic surface state. Chapter 8 takes elements from all previous chapters to present evidence of angle-dependent spin pumping in spin valves with a Cr interlayer. Finally, chapter 9 provides a summary of the work to date, and presents an outlook onto the prospects and challenges suggested by the findings.

Chapter 2

Theoretical Background

This chapter outlines the fundamental theoretical concepts that underpin both the physical phenomena and the experimental techniques employed to investigate them. Later chapters will build upon this foundation to fit particular requirements, but the information presented here applies to all aspects of the work. First, the energy terms associated with ferromagnetic thin films are discussed, outlining their origins and effects. With this grounding, the equation of motion for ferromagnetic resonance is introduced and explained, paying particular attention to the resonance condition. Damping processes are considered, with particular attention being paid to spin pumping, which features prominently in several chapters. Finally, the x-ray magnetic circular dichroism effect is discussed, including the magneto-optical sum rules that allow determination of spin and orbital contributions to the total magnetic moment.

2.1 Basic Energy Terms of Ferromagnetism

Before describing the dynamic properties of the magnetisation, it is instructive to consider the contributions towards the total energy, and their microscopic origin.

As in bulk samples one must take into account the Zeeman, exchange and magnetocrystalline anisotropy energies, but in thin films the demagnetisation tensor and interface effects are also important. The definition of a "thin" film is somewhat loose, but it can be said to be bounded from below by the magnetic exchange length, l_{ex}. Films below this are more commonly termed "ultra-thin", and act as a single macrospin. The exchange length is given by [41]:

$$l_{\mathrm{ex}} = \left(\frac{2A}{\mu_0 M_{\mathrm{s}}^2} \right)^{1/2} , \tag{2.1}$$

where A is the exchange constant of the magnetic material and M_{s} the saturation magnetisation. In Co, for example, $l_{\mathrm{ex}} = 3.5$ nm. The maximum thickness of a "thin" film is harder to define, but a practical definition can be reached by considering the fabrication techniques employed in film growth. The films studied in this work are grown by molecular beam epitaxy (MBE), which usually has a growth rate of < 0.1 Å/s. Therefore, in order to conserve time and preserve film quality, films are typically $t < 100$ nm, and often much less.

To find the total energy associated with magnetism in the film we sum over the individual contributions, as:

$$E_{\mathrm{tot}} = E_{\mathrm{ex}} + E_{\mathrm{demag}} + E_{\mathrm{anis}} + E_{\mathrm{Zeeman}} + \ldots , \tag{2.2}$$

with the energy terms here being exchange, demagnetisation, anisotropy and Zeeman energies, respectively. Contributing energies are chosen based on the nature of the sample; other terms, such as interlayer exchange or exchange bias, can be included in the same way.

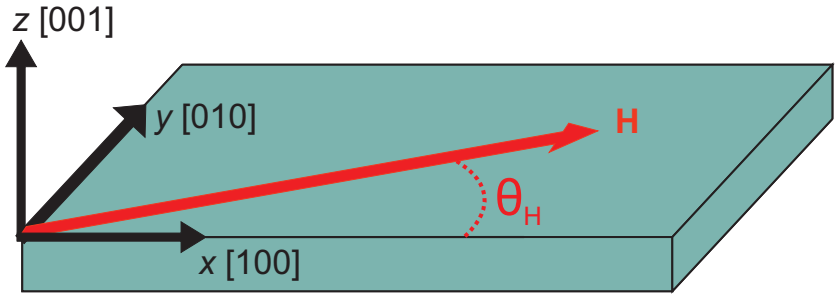


Figure 2.1: The coordinate systems used in this work, with respect to the crystalline axes of the (cubic) thin films. Principal Cartesian directions are always oriented with the crystalline axes, with z being out of the plane of the film. $\boldsymbol{H}$ denotes the applied magnetic field, and θ_{H} the angle it makes with the x axis.

2.1.1 Exchange Energy

The exchange energy is responsible for the formation of ferromagnetic (or antiferromagnetic) order, acting between the magnetic moments of adjacent atoms in the crystal lattice. Its origin is the overlap of the electronic wavefunctions, arising from the Coulomb interaction and the Pauli exclusion principle. Considering two neighbouring atoms with spins S_i, S_j, there is an energy difference between parallel or antiparallel alignment. Taking the Heisnberg interaction to couple N atoms we have the total energy:

$$E_{\mathrm{ex}} = -2\sum_{i<j}^{N} J_{\mathrm{i,j}}(S_i \cdot S_j) \ , \tag{2.3}$$

where $J_{\mathrm{i,j}}$ represents the exchange integral. For ferromagnetic order $J_{\mathrm{i,j}} > 0$, while for antiferromagnetic order $J_{\mathrm{i,j}} < 0$. This summation is commonly restricted to nearest-neighbours only, as the overlap of wavefunctions is a short range effect. While other, long-range, exchange mechanisms exist, the standard Coulomb interaction is the most important for the samples studied herein.

Taking the continuum approximation for a large scale sample, one assumes the length scale for variation of magnetisation is sufficiently large to ignore the atomic

structure. The total energy is then obtained by the integral:

$$E_{\text{ex}} = \frac{A}{M_{\text{s}}} \int_V (\nabla \boldsymbol{M})^2 \mathrm{d}V \ , \tag{2.4}$$

where the exchange constant $A = nJS^2/a$, with a the lattice constant, S the magnitude of the spin, and n a factor arising from crystal structure.

2.1.2 Demagnetisation Energy

The magnetic dipole interaction is a long range effect: the interaction of each magnetic moment with the dipole field of every other magnetic moment. The demagnetising field arises from the divergence of the overall magnetisation, and is largest in the case when the local magnetisation is aligned perpendicular to the edge of the sample, creating a magnetic pole. The energy of the demagnetising field is reduced through the formation of magnetic domains in the material. Though it is rather weaker than the exchange interaction, its long range makes it important, and in the confined geometries of thin films its effects are considerable. The interaction tends to oppose the formation of a uniform magnetic state, hence its name, and has the form:

$$E_{\text{demag}} = -\frac{\mu_0}{2} \int_V \boldsymbol{M} \cdot \boldsymbol{H}_{\text{demag}} \mathrm{d}V \ , \tag{2.5}$$

with $\boldsymbol{H}_{\text{demag}}$ the demagnetising field, and the integration running over the whole sample volume, V. Determining $\boldsymbol{H}_{\text{demag}}$ is in general challenging, requiring numerical integration. Fortunately, analytical solutions exist in the case of homogeneously magnetised ellipsoids where $\boldsymbol{H}_{\text{demag}} = \text{-}N \cdot \boldsymbol{M}$, and this can be used to approximate a thin film. Here N is the (dimensionless) demagnetising tensor, which controls orientation and strength of the demagnetising field. This tensor can be diagonalised when the magnetisation is along one of the principal axes, and

the sum of the diagonal elements satisfies $N_{xx} + N_{yy} + N_{zz} = 1$. For an infinite thin film in the $x - y$ plane the diagonal elements are $N_{xx} \approx N_{yy} \approx 0$, $N_{zz} \approx 1$, effectively constraining the magnetisation to lie in the plane of the film, unless there is a significant external field or perpendicular magnetic anisotropy.

2.1.3 Magnetocrystalline Anisotropy Energy

The magnetisation in a crystalline ferromagnet has preferred orientations, termed the easy axes, due to the spin-orbit interaction. The spin moment of the electron couples to the orbital moment, whose symmetry is determined by the underlying symmetry of the lattice. This causes certain crystallographic directions to be more energetically favourable than others. All ferromagnetic materials discussed in this thesis have a cubic crystal structure, leading to a four-fold anisotropy with a typical easy axis in the [100] direction, and a hard axis in the [110] direction. An additional in-plane uniaxial (two-fold) anisotropy can also arise due to chemical interactions with the substrate or mechanical strain during growth. Furthermore, the reduced symmetry at an interface enhances the spin-orbit interaction, and can also lead to an out-of-plane uniaxial anisotropy, which in certain cases leads to films having their easy axis of magnetisation oriented out of the plane. The magnetocrystalline anisotropy energy is:

$$E_{\text{anis}} = -\frac{K_C^{\parallel}}{2}(\alpha_x^4 + \alpha_y^4) - \frac{K_C^{\perp}}{2}\alpha_z^4 - K_U^{\parallel}\frac{(\boldsymbol{n}\cdot\boldsymbol{M})^2}{M_{\text{s}}^2} - K_U^{\perp}\alpha_z^2 \,, \tag{2.6}$$

where $\alpha_{x,y,z}$ are the direction cosines with respect to the [100], [010], and [001] axes, and $K_C^{\parallel}$, $K_C^{\perp}$, $K_U^{\parallel}$, $K_U^{\perp}$ are the in-plane and out-of-plane cubic and unixial anisotropy constants, respectively. In all cases in this work it is sufficient to consider the in-plane components, as magnetisation is confined to the plane of the film.

2.1.4 Zeeman Energy

In the presence of an external magnetic field, $\boldsymbol{H}$, an energy term arises due to the interaction of the magnetization and the external field:

$$E_{\text{Zeeman}} = -\mu_0 \int_V \boldsymbol{M} \cdot \boldsymbol{H} \qquad . \tag{2.7}$$

The Zeeman energy acts to align the magnetic field and the magnetisation, and is the parameter that is most readily varied in typical FMR experiments.

2.2 Magnetisation Dynamics

In a ferromagnetic resonance experiment a time dependent field with frequency typically in the GHz range is used to excite precession in a ferromagnetic material, while a static bias field combined with internal fields of the material defines an equilibrium orientation of magnetisation. When studying FMR we are primarily concerned with the resonance frequency, which relates to the internal energy of the system, and the resonance linewidth, which is governed by energy loss mechanisms. The combination of different energy terms discussed in the previous section leads to an effective field [14]:

$$\boldsymbol{H}_{\text{eff}} = -\frac{1}{\mu_0} \nabla_M E_{\text{tot}} \ , \tag{2.8}$$

the functional derivative of the total energy with respect to the magnetisation. This is the effective field which drives FMR, linking the resonance frequency to the different energetic contributions within the sample. Such magnetodynamics are described by the Landau-Lifshitz-Gilbert (LLG) equation [42].

As the central technique of this thesis, the following sections examine the theoretical concepts of FMR in greater detail. First, the LLG is introduced and

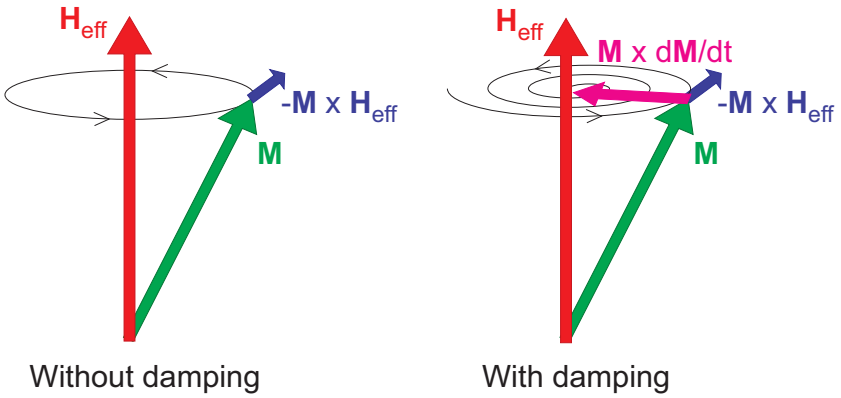


Figure 2.2: Forces acting on magnetisation as it undergoes undamped (left) and damped (right) precession. Without damping the magnetisation will precess indefinitely, but in its presence the magnetisation vector spirals in to align with the effective field.

discussed, outlining its component terms. Next, the equilibrium orientation of the magnetisation is considered, the direction about which the magnetisation precesses during FMR. With this, the resonance condition is derived from a macrospin approximation, yielding the Kittel equation for resonance frequency. After this, the relaxation mechanisms that lead to magnetisation damping are explored, including intrinsic Gilbert damping, and the phenomenon of spin pumping, which modifies the LLG with additional terms [22, 43].

2.2.1 The Landau-Lifshitz-Gilbert Equation

In the classical limit the spin dynamics of a ferromagnet are governed by the Landau-Lifshitz equation of motion, describing the precession of the magnetisation about an effective field arising from internal and external fields. This formulation does not include a damping term, and would therefore lead to continuous precession. In practice, such motion is typically damped over a period of tens of nanoseconds. There are several formulations that add a damping term, the most widely used being Gilbert's addition of a phenomenological damping parameter, in analogy to viscous drag. We then have the Landau-Lifshitz-Gilbert

equation [42, 44]:

$$\frac{d\boldsymbol{m}}{dt} = -\gamma \left[\boldsymbol{m} \times \boldsymbol{H}_{\text{eff}}\right] + \alpha \left[\boldsymbol{m} \times \frac{\partial \boldsymbol{m}}{\partial t}\right] , \tag{2.9}$$

with γ the gyromagnetic ratio, $\boldsymbol{m}$ is the unit magnetisation vector of the material, $\boldsymbol{H}_{\text{eff}}$ the effective magnetic field (through which the various energy terms discussed in section 2.1 enter the equation), and α the dimensionless Gilbert damping parameter. Note that this form of the damping preserves the length of the magnetisation vector, making it unsuitable for describing damping mechanisms such as two magnon scattering. Damping is discussed in more detail in section 2.3.

2.2.2 Equilibrium Orientation of Magnetisation

In order to determine the FMR frequency one must first identify the equilibrium orientation of the magnetisation. When the external bias field is aligned along an easy axis the magnetisation and field are collinear, but this is not in general the case. Rather, the internal fields of the sample can lead to a canting of the magnetisation away from the bias field; a misalignment of several degrees is possible. This is important not just when calculating the resonance frequency, but also when determining precessional damping. The effect of field dragging caused by magnetisation canting leads to an angle-dependent contribution to the total damping within a sample.

To determine the equilibrium condition of the magnetisation we minimise the free energy, F, such that:

$$\frac{\partial F}{\partial \phi} = 0 , \tag{2.10}$$

where ϕ is the in-plane angle.

For the case of a cubic system, with the magnetisation confined to the plane of the film at an angle ϕ_{M}, this is:

$$\frac{\partial F}{\partial \phi} = \mu_0 MH \sin[\phi_{\mathrm{M}} - \phi_{\mathrm{H}}] - K_{\mathrm{U}} \sin[2(\phi_{\mathrm{M}} - \phi_{\mathrm{U}})] + \frac{1}{2} K_{\mathrm{C}} \sin[4(\phi_{\mathrm{M}} - \phi_{\mathrm{C}})] = 0 \ , \quad (2.11)$$

where ϕ_{H} is the angle of the external field, ϕ_{C} the angle of the magnetocrystalline cubic easy axis, and ϕ_{U} the angle of the magnetocrystalline uniaxial easy axis. Here M and H are the magnitudes of the magnetisation and external field, respectively, $K_{\mathrm{U}||}$ the in-plane two-fold (uniaxial) anisotropy constant and K_{C} the in-plane four-fold (cubic) anisotropy constant. This equation must be solved numerically, or one can instead make the substitution $\Delta\phi = \phi_{\mathrm{M}} - \phi_{\mathrm{H}}$, the misalignment of the magnetisation from the external field, then expand in terms of $\Delta\phi$. Discarding terms above those linear in the expansion of $\Delta\phi$, one arrives at:

$$\Delta\phi \approx \frac{K_{\mathrm{C}} \sin[4(\phi_{\mathrm{M}} - \phi_{\mathrm{C}})] - 2K_{\mathrm{U}} \sin[2(\phi_{\mathrm{M}} - \phi_{U})]}{-2\mu_0 MH - 4K_{\mathrm{C}} \cos[4(\phi_{\mathrm{M}} - \phi_{\mathrm{C}})] + 4K_{\mathrm{U}} \cos[2(\phi_{\mathrm{M}} - \phi_{U})]} \ . \quad (2.12)$$

Retaining terms up to second order in $\Delta\phi$ this is the quadratic formula:

$$\begin{aligned} \Delta\phi &\approx \frac{-b + \sqrt{b^2 - 4ac}}{2a}, \\ a &= -4K_{\mathrm{C}} \sin[4(\phi_{\mathrm{M}} - \phi_{\mathrm{C}})] - 2K_{\mathrm{U}} \sin[2(\phi_{\mathrm{M}} - \phi_{U})] \ , \\ b &= 2K_{\mathrm{C}} \cos[4(\phi_{\mathrm{M}} - \phi_{\mathrm{C}})] - 2K_{\mathrm{U}} \cos[2(\phi_{\mathrm{M}} - \phi_{U})] + \mu_0 MH \ , \\ c &= \frac{1}{2} K_{\mathrm{C}} \sin[4(\phi_{\mathrm{M}} - \phi_{\mathrm{C}})] - K_{\mathrm{U}} \sin[2(\phi_{\mathrm{M}} - \phi_{U})] \ , \end{aligned} \quad (2.13)$$

which can be solved to find the equilibrium condition of the magnetisation.

2.2.3 The Resonance Condition

The condition for ferromagnetic resonance is derived using the macro-spin approximation, wherein all spins are assumed to undergo coherent precession. This approach implicitly neglects the contribution of the exchange interaction to the magnetisation dynamics. Further, it is not strictly true that all spins precess coherently in a material undergoing FMR, particularly in the case of coupled multilayers or patterned samples. However, this approximation is very useful as it allows the resonance condition to be derived using a simple variational approach that captures the key features of FMR.

In the case of small perturbations, and including a correction for Gilbert damping, the resonance frequency is found using [45]:

$$\left(\frac{\omega}{\gamma}\right)^2 = \frac{1+\alpha^2}{\left[M\sin(\theta)\right]^2}\left[\frac{\partial^2 F}{\partial\theta^2}\frac{\partial^2 F}{\partial\phi^2} - \left(\frac{\partial^2 F}{\partial\theta\partial\phi}\right)^2\right] , \tag{2.14}$$

with $\gamma = g\mu_B/\hbar$ the gyromagnetic ratio. Again restricting the magnetisation to lie in-plane, this reduces to [14, 45, 46]:

$$\begin{aligned}\left(\frac{\omega}{\gamma}\right)^2 = \left(1+\alpha^2\right)\Bigg[&\mu_0 M + \mu_0 H\cos\left[\phi_M - \phi_H\right] + \frac{K_C}{2M}\left(3+\cos\left[4\left(\phi_M-\phi_C\right)\right]\right) + \\ &\frac{K_U}{M}\left(1-\cos\left[2\left(\phi_M-\phi_U\right)\right]\right)\Bigg] \\ \Bigg[&\mu_0 H\cos\left[\phi_M-\phi_H\right] + \frac{2K_C}{M}\left(\cos\left[4\left(\phi_M-\phi_C\right)\right]\right) - \\ &\frac{2K_U}{M}\cos\left[2\left(\phi_M-\phi_U\right)\right]\Bigg] .\end{aligned} \tag{2.15}$$

This is the Kittel equation [47], which is used to extract material parameters from the resonant fields measured in an FMR experiment.

An alternative approach to determining the resonance condition is to use harmonic solutions of a linearised version of the LLG to find the AC magnetic susceptibility

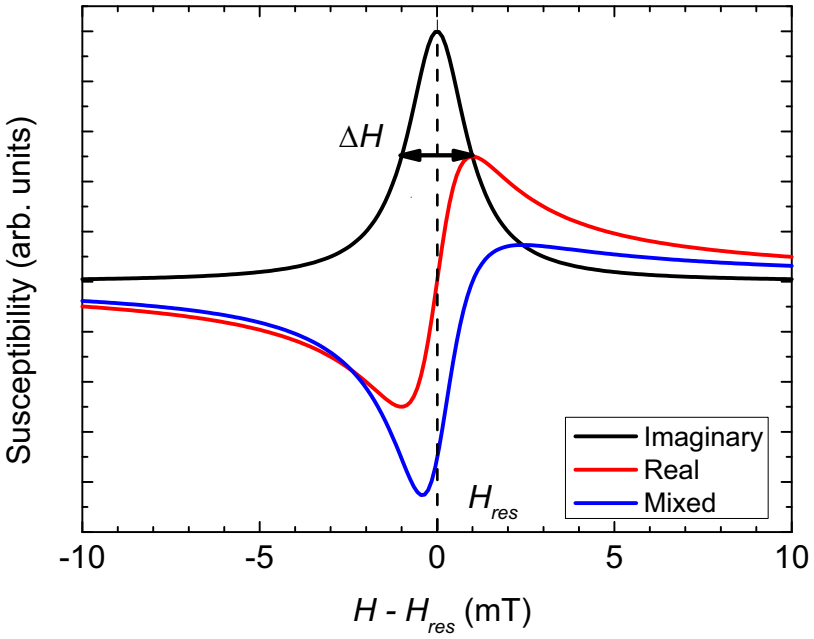


Figure 2.3: Illustration of pure real (black), pure imaginary (red) Lorentzians, and an equal mixing of the two, $\epsilon = 45$.

tensor, further details of this technique can be found in chapter 5 and Appendix A. This method yields real and imaginary components of AC susceptibility, which give the lineshape of the resonance as a Lorentzian:

$$Im[\chi(H)] = A\frac{\Delta H}{\Delta H^2 + (H - H_{\rm res})^2} \tag{2.16}$$

$$Re[\chi(H)] = A\frac{H - H_{\rm res}}{\Delta H^2 + (H - H_{\rm res})^2}\ , \tag{2.17}$$

where A is a scaling constant for the amplitude of the resonance, ΔH is the Half-Width at Half-Maximum (HWHM) of resonance.

In the ideal case, an FMR experiment measures the imaginary component of the susceptibility. However, due to losses in the cabling and correlations between the magnetodynamics and the exciting pulse shape, the actual result is a combination of real and imaginary components known as an asymmetric Lorentzian:

$$y(H) = A \cdot \frac{\Delta H\cos(\epsilon) + (H - H_{\rm res})\sin(\epsilon)}{\Delta H^2 + (H - H_{\rm res})^2}\ . \tag{2.18}$$

Here ϵ is the mixing angle: for $\epsilon = 0$ the resonance is purely the imaginary component, while for $\epsilon = \frac{\pi}{2}$ it is purely real.

2.2.4 Static Exchange Coupling

The static interlayer exchange coupling is a general term for any interaction that acts to (anti-)align the magnetisations of the two layers in a spin valve. Examples of such interactions include Ruderman-Kittel-Kasuya-Yosida (RKKY), superexchange, Néel or orange peel coupling, and direct exchange through a discontinuous spacer layer. In the case of the Cr spin valves studied in chapter 8, for example, the coupling between the two magnetic layers is RKKY, wherein conduction electrons provide an interaction mechanism through the hyperfine interaction with the nuclear spins. The presence of a static interaction modifies the LLG equation with an additional term [32, 35]:

$$-\frac{\partial \boldsymbol{m}^i}{\partial t} = \boldsymbol{m}^i \times \left[\gamma^i \boldsymbol{H}^i_{\text{eff}} + \beta^i M^j_{\text{s}} \boldsymbol{m}^j - \alpha^i_0 \frac{\partial \boldsymbol{m}^i}{\partial t}\right], \tag{2.19}$$

where β is the interlayer exchange, and i, j index magnetic layers. The interlayer exchange is defined as [31, 35, 48]:

$$\beta_i = \frac{A_{\text{ex}}}{M^i_{\text{s}} d^i} \cos(\phi^i_{\text{M}} - \phi^j_{\text{M}}), \tag{2.20}$$

with A_{ex} the interlayer exchange constant, d the thickness of the magnetic layer, and ϕ_{M} the equilibrium orientation of magnetisation. The sign of A_{ex} determines whether the interaction favours parallel (positive) or antiparallel (negative) alignment.

2.3 Magnetisation Damping

The study of magnetic relaxation processes in thin films and nanoscale devices has become increasingly important in recent years, spurred by the interest in phenomena such as spin-transfer torques and vortex core dynamics [6,49]. Relaxation of the excited magnetic state can proceed by a number of different mechanisms, including coupling to the crystal lattice [14], dissipation into the magnetic subsystem through two magnon scattering [17, 50], and spin pumping [22, 43]. The resonance linewidth functions as a sensitive probe of damping, and many studies have examined the interplay of layer structure, crystal quality and magnetisation alignment in determining the precessional damping [51–54].

Broadly speaking, damping processes can be separated into two types - Gilbert and non-Gilbert. Gilbert-type damping processes preserve the length of the magnetisation vector, as they do not redistribute energy within the magnetic subsystem. More pragmatically, they depend linearly on microwave frequency. Examples of such processes include phonon drag, itinerant electron processes and spin-pumping. Non-Gilbert damping processes preserve only the z-component of the magnetisation vector, and their magnitude has a non-linear frequency dependence. An important example of non-Gilbert damping is two magnon scattering, wherein the $k = 0$ magnon, the FMR mode, scatters into degenerate magnon states with $k \neq 0$.

2.3.1 Gilbert Damping

The resonance linewidth, ΔH, has both intrinsic (Gilbert) and extrinsic (non-Gilbert) contributions, and is given by [55]

$$\Delta H = \frac{4\pi f}{\gamma}\alpha + \Delta H_0 \ , \tag{2.21}$$

with α the (dimensionless) Gilbert damping parameter and ΔH_0 the extrinsic broadening. Gilbert damping in pure metals is primarily caused by the spin orbit interaction, scattering the excitations from phonons or magnons [56]. Ultimately, this mechanism allows transfer of energy from the spin subsystem of the sample to the lattice. There are several mechanisms by which it may be enhanced, for example, through the introduction of rare earth impurities [19,57,58], the presence of an adjacent rare earth layer [59], or through spin pumping, wherein angular momentum is pumped out of an on-resonance ferromagnetic layer [21].

2.3.2 Non-Gilbert Damping

Extrinsic broadening in equation (2.21) arises from imperfections in the sample, for example magnetic inhomogeneities, or the presence of defects that break translational symmetry. Extrinsic damping processes typically do not conserve the magnitude of the magnetisation vector. Perhaps the most important non-Gilbert damping mechanism is two magnon scattering, wherein the k=0 magnon that is the FMR mode scatters from a defect within the sample to form degenerate magnon states with $k \neq 0$ [16]. For this to occur, the spin wave dispersion must allow for the formation of degenerate states. Further, the character of the spin waves that can be excited is determined by the distribution of the defects that act as scattering centres within the sample. The wavelength of the excited spin waves is related to the length scale of the defects – long wavelength spin waves require the presence of defects on the order of hundreds of nanometres. Two magnon scattering has a non-linear frequency dependence, and can have a significant in-plane angular variation, depending on the co-ordination of scattering sites within the magnetic layer [17, 54]. Its contribution was found to be negligible in the structures studied in this thesis, and will not be discussed further.

2.3.3 Spin Pumping

The generation and detection of spin currents is at the foundation of spintronics, being integral to many proposals for new memory and logic devices [6, 7, 12, 13, 57]. The pure spin current emitted by a ferromagnet undergoing FMR [20] is one candidate for generating such currents, and offers the opportunity to study these effects in the absence of a charge current. A spin current can persist across a normal metal, and in a trilayer structure either return to the first FM/NM interface, or else flow through to a second NM/FM interface. If it is not reflected here, it crosses the interface and is absorbed by the FM, inducing precession through the STT [11]. A cartoon of the spin pumping effect is shown in Fig. 2.4. Such spin pumping can be observed by measuring increased damping (through increased FMR linewidth) due to outflow of angular momentum from the source FM [21, 43], by inverse spin Hall effect in the sink layer [33], or layer-specific measurements of precession or spin accumulation using x-ray magnetic circular dichroism (XMCD) [15, 60, 61]. A brief outline of the theory of spin pumping is given below, highlighting its effects on the magnetodynamics, and the observable quantities it influences.

As the magnetisation of a ferromagnetic layer precesses on resonance it acts as a spin battery, generating a pure spin current transverse to the axis about which it precesses. When the FM layer is thicker than the ferromagnetic coherence length, a pure spin current can be driven into an adjacent NM layer. This is shown schematically in Fig. 2.4(a). The pumped spin momentum that enters the NM layer, $\boldsymbol{I}_{\mathrm{sp}}$, is determined by the spin mixing conductance, $g_{\uparrow\downarrow}$ as [23]:

$$\boldsymbol{I}_{\mathrm{sp}} = \frac{\hbar}{4\pi}\mathrm{Re}(g_{\uparrow\downarrow})\left[\boldsymbol{m} \times \frac{\partial \boldsymbol{m}}{\partial t}\right] . \tag{2.22}$$

If the spin-flip relaxation rate in the adjacent NM layer is smaller than the pumping

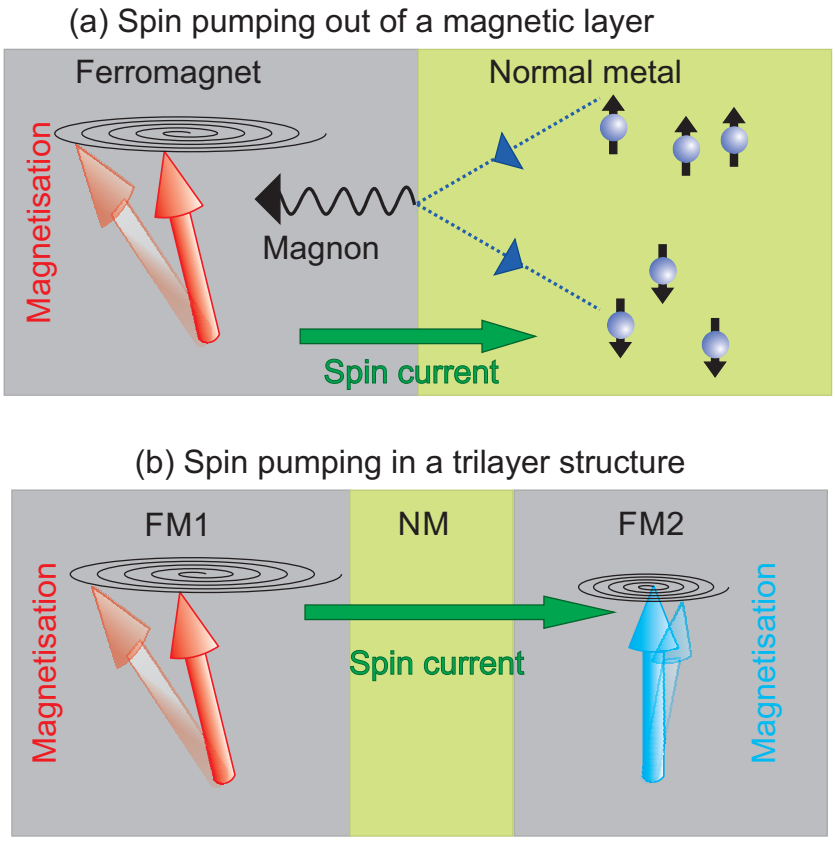


Figure 2.4: Illustration of the concept of spin pumping in a bilayer (a) and a trilayer structure (b). In the first case, spins are ejected by the precessing magnetisation and lead to a build up of angular momentum in the adjacent nonmagnetic layer, causing an increase in damping. In the second case, the spins pumped across the nonmagnetic spacer reach the second ferromagnetic layer, and there induce precession through the spin transfer torque.

rate a total spin angular momentum $\boldsymbol{s}$ builds up in the NM layer, and spin-backflow occurs. This leads to a backflow current, back into the FM layer [20]:

$$\boldsymbol{I}_{\text{back}} = \frac{\tilde{g}_{\uparrow\downarrow}}{2\pi n} \left[\boldsymbol{s} - \boldsymbol{m}(\boldsymbol{m}) \cdot \boldsymbol{s}\right] \ , \tag{2.23}$$

with n the one-spin density of states. Therefore, the total spin momentum leaving the FM layer is reduced by the amount flowing back into it from the normal metal. The penetration of the spin current into the NM spacer layer is governed by the

scattering lifetimes of conduction electrons, and is given by [22]:

$$\delta_{sp} = D \cdot \tau_{sf} = v_{\mathrm{F}} \sqrt{\tau_{sf} \tau_m / 3} \ , \tag{2.24}$$

where D is the diffusion coefficient in the normal metal, v_{F} the Fermi velocity in the NM layer, and τ_{sf} and τ_m the NM layer's spin-flip and momentum scattering times, respectively.

The increased flow of spin momentum out of the FM layer acts as an additional channel for energy loss, leading to an increase in damping. This damping is linear with resonant frequency, and can thus be described in the same terms as Gilbert damping. The contribution to total damping due to spin pumping can be isolated by comparison with bare FM layers. In a FM/NM system the spin-pumping contribution to damping is [23]:

$$\begin{aligned} \alpha_{sp} = & \left[1 - \frac{(1 + e^{-2kd}) \frac{1}{2} v_{\mathrm{F}}}{\left(Dk + \frac{1}{2} v_{\mathrm{F}} + e^{-2kd} \right) \left(\frac{1}{2} v_{\mathrm{F}} - Dk \right)} \right] \\ & \times \frac{g \mu_{\mathrm{B}}}{4 \pi M_s} \tilde{g}_{\uparrow\downarrow} \frac{1}{d} \ , \end{aligned} \tag{2.25}$$

where $k = 1/\delta_{sp}$ and d the thickness of the FM layer. As the thickness of the NM layer increases, the spin current that it can absorb also increases, in turn increasing damping in the FM. However, once $t_{\mathrm{NM}} > \delta_{sp}$, α_{sp} saturates to its maximum value.

In the case of a FM1/NM/FM2 structure, the second FM layer acts as a spin sink for the spin current driven out of the first FM layer. The absorbed spin current exerts a torque on the static magnetisation in FM2, which can lead to precession of magnetisation even when the resonance condition is not met. Figure 2.4(b) shows this process schematically. The addition of a second scattering interface and a high-efficiency spin sink modifies the spin pumping equations significantly.

In this case the LLG becomes [15]:

$$-\frac{\partial \boldsymbol{m}^i}{\partial t} = \boldsymbol{m}^i \times \left[\gamma^i \boldsymbol{H}^i_{\text{eff}} - (\alpha^i_0 + \alpha^i_{ii})\frac{\partial \boldsymbol{m}^i}{\partial t}\right] + \alpha^i_{ij}\boldsymbol{m}^j \times \frac{\partial \boldsymbol{m}^j}{\partial t}, \tag{2.26}$$

where the subscript denotes the magnetic layer number, α^i_0 the intrinsic Gilbert damping parameter, α^i_{ii} damping due to angular momentum pumped out of layer i, and α^i_{ij} (anti-)damping due to angular momentum driven into layer i from layer j. The anti-damping torque is only significant when both layers are simultaneously on-resonance, otherwise $\partial \boldsymbol{M}^j/\partial t \approx 0$ and its effects are negligible.

The additional damping in a trilayer is defined as [62]:

$$\alpha_{sp} = \left[1 - \frac{\left[\left(Dk + \frac{1}{2}v_{\text{F}}\right) + e^{-2kd}\left(Dk - \frac{1}{2}v_{\text{F}}\right)\right]\frac{1}{2}v_{\text{F}}}{\left(Dk + \frac{1}{2}v_{\text{F}}\right)^2 + e^{-2kd}\left(Dk - \frac{1}{2}v_{\text{F}}\right)^2}\right] \times \frac{g\mu_{\text{B}}}{4\pi M_s}\tilde{g}_{\uparrow\downarrow}\frac{1}{d}\ , \tag{2.27}$$

which, in the limit of ballistic transport, simplifies to [15]:

$$\alpha_{sp} = \frac{g\mu_{\text{B}}}{4\pi M}\tilde{g}_{\uparrow\downarrow}\frac{1}{d}\ . \tag{2.28}$$

Damping is highest when the spin current can cross the spacer layer and be efficiently absorbed by the second FM layer. As the thickness of the spacer layer increases the spin pumping decreases due to increasing backflow. The increase in damping reaches its minimum value when the spacer layer is thicker than the spin coherence length, and no current reaches FM2 [23].

2.4 X-Ray Magnetic Circular Dichroism

X-ray Magnetic Circular Dichroism (XMCD) is a powerful tool for chemical and magnetic characterisation, capable of identifying, for example, atomic valences, site occupation and spin and orbital moments through application of the much celebrated sum rules (see section 2.4.1). The absorption of light by a material is governed by its wavelength and the available energy level transitions within the sample. X-ray absorption spectra (XAS) measurements are performed by sweeping the energy of the x-ray photons and observing the regions of maximum absorption, when the incident light corresponds to a given core-level transition in the atoms. These regions are known as absorption edges, and are typically referred to in the spectroscopic notation, e.g. $L_{2,3}, M_{4,5}$ etc. In this way XAS and XMCD are element-selective techniques, as each edge corresponds uniquely to one element. This can be exploited to probe specific layers in a magnetic heterostructure.

In the $3d$ transition metals that are the central subject of this thesis, the $L_{2,3}$ edge corresponds to the transition from spin-split $2p_{\frac{1}{2},\frac{3}{2}}$ core states to the $3d$ valence states. When the incident x-rays are circularly polarised there is an extra selection rule, $\Delta m_j = \pm 1$, which results in a different transition probability for left- and right-circularly polarised light into the unoccupied states valence band. This effect is comparable to the Faraday or Kerr effects, but much stronger as the spin-orbit interaction is larger in the core level than in the optical region, at tens of eV, compared to less than 100 meV [38]. In this way, the transition probability depends on both the helicity of the incoming light and the magnetic state of the illuminated material. The XMCD is defined as the difference between two XAS measurements performed with opposite magnetisations or x-ray helicities, as:

$$\mathrm{XMCD}(E) = \mu^{-}(E) - \mu^{+}(E) \ , \tag{2.29}$$

where $\mu^-(E)$ and $\mu^+(E)$ are the absorption coefficients with left and right circularly polarized light, respectively, as a function of incident photon energy. The XMCD is therefore sensitive to the difference in the density of empty states with different spin moment.

To understand XMCD, it is instructive to consider a two-step approach, in a monoelectronic atomic picture [63]: in a $3d$ metal, the $2p$ core state is spin split with $j = 3/2$ (L_3) and $j = 1/2$ (L_2), with the spin and orbital angular moments having parallel and antiparallel coupling, respectively. When absorbing an x-ray photon with helicity ± 1, the helicity vector is parallel (antiparallel) to the $2p$ orbital angular moment. There is therefore a preferential excitation of electrons of spin up (down) direction. The excited electron then moves to an unoccupied state in the $3d$ valence band. In a magnetic material the density of states in the $3d$ band is different for the two spin orientations. This process is illustrated schematically in Fig. 2.5. As the transition probability is related to the available states, the resulting XMCD spectrum has a net negative L_3 and positive L_2 peak. In this way, absorption of light depends upon the helicity of the incident light and the magnetisation of the sample: reversing either will reverse the XMCD spectrum. The intensity of the XMCD effect scales as the dot product of the magnetisation vector and the polarisation vector of the x-rays, thus if the magnetisation is perpendicular to the beam direction no XMCD is observed.

2.4.1 Sum Rules

One of the most powerful aspects of XMCD is its ability to independently determine spin and orbital contributions to total magnetic moment, through the use of the sum rules. Originally derived by Thole *et al.* [40] and Carra *et al.* [39], they relate the area under the XAS and XMCD spectra to the spin, $m_{\mathrm{S}} = -2\mu_{\mathrm{B}}\langle S_Z\rangle/\hbar$

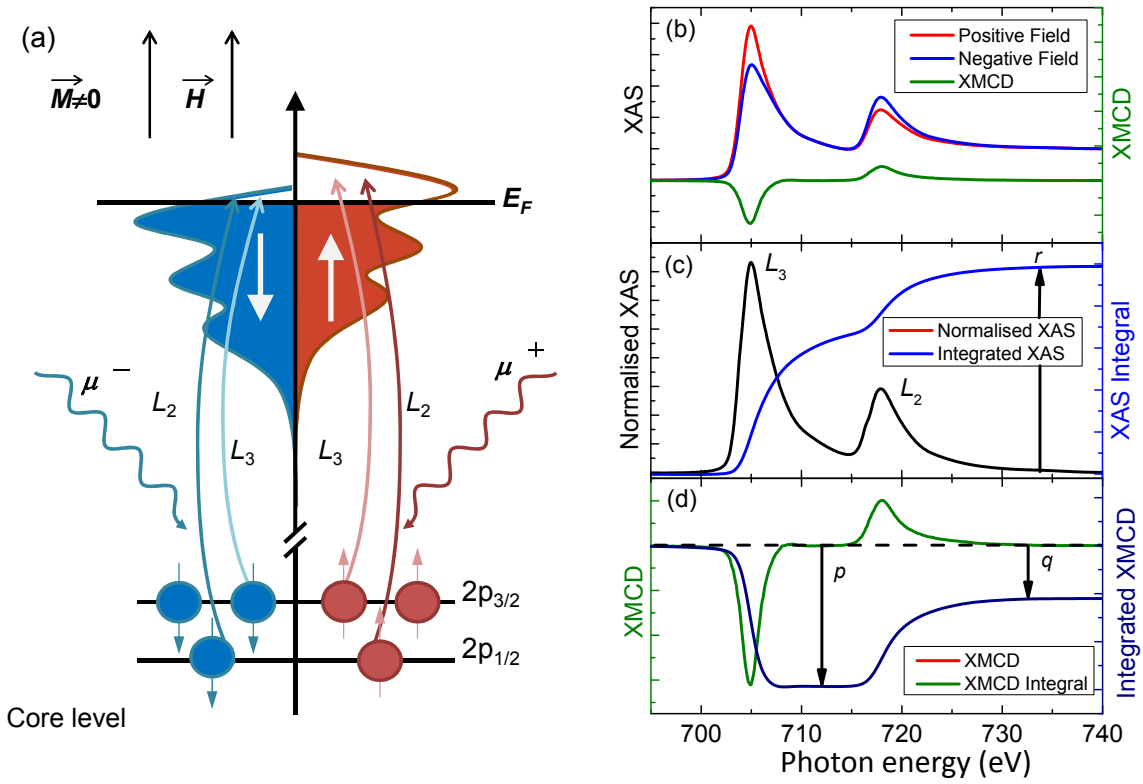


Figure 2.5: (a) Schematic of the energy level processes involved in XMCD, wherein a circularly polarised photon excites a spin polarised electron from the $2p$ level. Right panel shows the XAS and XMCD spectra measured for an Fe thin film. In (b), energy is swept over the $L_{2,3}$ absorption edges at fixed helicity with two directions of the external field, and the difference in absorption is the dichroism arising from selective absorption of polarised photons. (c) shows the average absorption of x-rays, and the integrated absorption as required by the XMCD sum rules. In (d), the XMCD is again plotted, along with its cumulative integral, with the quantities p and q required for the sum rules marked. Figure after Ref. [24].

and orbital, $m_{\mathrm{L}} = -\mu_{\mathrm{B}}\langle L_Z\rangle/\hbar$ magnetic moments. These necessary integrals are:

$$\begin{aligned} p &= \int_{L_3} (\mu^- - \mu^+)\mathrm{d}E \\ q &= \int_{L_3} (\mu^- - \mu^+)\mathrm{d}E + \int_{L_2} (\mu^- - \mu^+)\mathrm{d}E \\ r &= \int_{L_3+L_2} (\mu^- + \mu^+)\mathrm{d}E \ . \end{aligned} \tag{2.30}$$

In practical terms p and q are the XMCD integrals over the L_3 and the combined L_3 + L_2 edges, respectively, and r the integral over the sum of positive and negative field spectra over the L_3 + L_2 edges. Figure 2.5 shows the cumulative integrals of the XAS and the XMCD, indicating typical definitions for the extraction of p, q, r. A background that takes into account transitions into higher states or into the continuum must be subtracted before calculating r. This is usually approximated by a hyperbolic step function at each absorption edge [64].

The sum rule for orbital moment is expressed as:

$$\frac{m_L}{n_h} = -\frac{4}{3}\frac{q}{r} \ , \tag{2.31}$$

with n_h the number of holes. In the case of the spin sum rule, one must also consider the dipolar term, m_D, which depends on the inter-atomic dipole operator, $\langle T_Z\rangle$. However, in the case of undistorted cubic symmetry it is normal to assume that the angle averaged $\langle T_Z\rangle$ is much less than m_S. The sum rule for spin moment is then:

$$\frac{m_S}{n_h} = -2\left(\frac{3p-2q}{r}\right) \ . \tag{2.32}$$

It is also common to consider the ratio of spin to orbital moments, as it is independent of n_h:

$$\frac{m_L}{m_S} = \frac{1}{(9/2)(p/q)-3} \ . \tag{2.33}$$

As it is non-trivial to determine n_h, values of m_L and m_S are commonly expressed as magnetic moment per d-hole, along with the m_L/m_S ratio.

Chapter 3

Experimental Techniques

This chapter describes the experimental techniques employed over the course of the thesis investigation. Sample fabrication is described first, detailing the general operating principles of molecular beam epitaxy and reflection high energy diffraction, as well as specific information about the particular systems used. Next, ferromagnetic resonance is considered, building from the theoretical framework outlined in the previous chapter to cover the vector-network analyser technique. SQUID magnetometry, the other magnetic characterisation tool employed, is explained next. Following this, the focus shifts to measurements performed at synchrotron facilities, outlining the principles of synchrotron radiation as well as the particulars of the techniques employed: x-ray absorption spectroscopy, x-ray magnetic circular dichroism, and x-ray detected ferromagnetic resonance.

3.1 Molecular Beam Epitaxy

High quality magnetic thin films and heterostructures were prepared using molecular beam epitaxy (MBE) [65–67], an ultra high vacuum (UHV) growth technique that allows precise control of film thickness, composition, and interface quality.

The concept is based on assembling a crystal through direct deposition of constituent atoms, achieving superior purity through the use of ultrahigh vacuum conditions and low energy deposition [68–70]. MBE has been extensively applied to the synthesis and investigation of a wide range of materials [71], including complex oxides [72], semiconductor devices [73], and magnetic tunnel junctions [74]. The technique allows unmatched thickness and composition control, and it can be applied to thin-film structures both close to [75] and far away [76] from thermodynamic equilibrium. MBE is therefore an indispensable tool at the forefront of materials research and surface science.

As a UHV technique MBE requires a sophisticated chamber design to maintain pressures better than 1×10^{-9} Torr, and to allow operation of growth, characterisation and sample manipulation in this environment. Such pressures are typically achieved through the use of turbomolecular pumps, aided by a liquid nitrogen cryoshroud, which reduces the kinetic energy of free gas molecules to further reduce the chamber pressure. UHV is required due to the extremely low growth rates employed in MBE, which are often less than 0.1Å/s. Strict control of chamber pressure throughout growth limits the impurities that are incorporated into the film during growth, which is beneficial from the standpoint of both chemical purity and crystalline order.

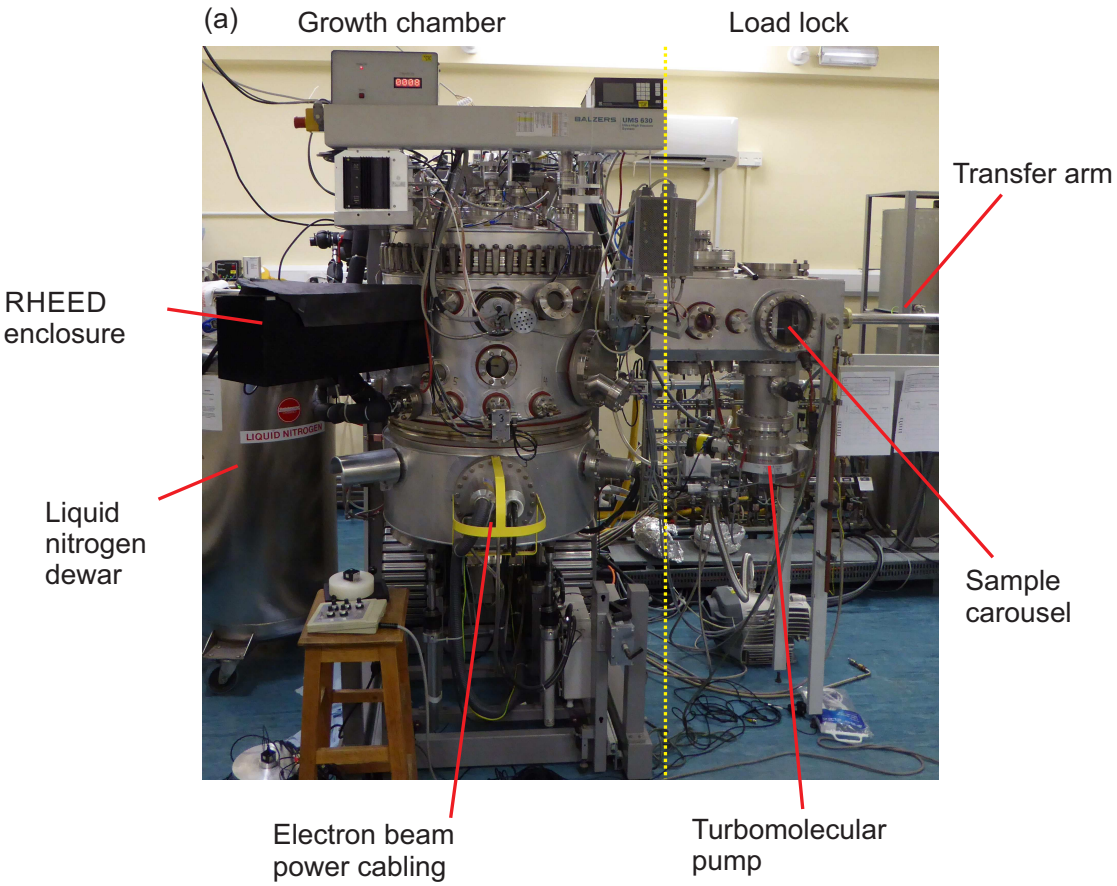
Three MBE systems were used over the course of this thesis: the Lanthanide MBE (LaMBE) in the Clarendon lab, Oxford [77]; the micro-MBE (μ-MBE) [78] on beamline I05 at Diamond Light Source; and a chalcogenide MBE in the Research Complex at Harwell. The LaMBE is a venerable Balzers UMS 630 system, equipped with three effusion cells and three electron-beam evaporators, with a quartz crystal microbalance for growth rate calibration, and a reflection high energy electron diffraction (RHEED) system for sample characterisation during growth. The μ-MBE is a newly developed system (Createc Fischer) that was

installed and commissioned over the course of this thesis. It houses 8 high temperature effusion cells, a beam flux monitor for growth rate calibration and a miniaturised RHEED. The topological insulator layers used in chapter 7 were grown in a dedicated chalcogenide MBE. However, this system was not operated by the author, and for further details the interested reader is referred to Ref. [79]. Despite several technical differences between the systems, the core operating principles are the same. Aside from noting which system was used for which sample series, no great distinction will be drawn between them.

The LaMBE is shown in Fig. 3.1, and is composed of two chambers: a load-lock and growth chamber. New substrates are mounted on holders and introduced to the system at the load lock, which has a storage carousel for up to 6 samples. Due to its comparatively small volume, the load lock can be pumped to a pressure of 5×10^{-8} Torr in about 12 hours. From here, samples are transferred to the growth chamber using the manipulator arm. The exterior of the μ-MBE is shown in Fig. 3.2. It is composed of three chambers: a load-lock and growth chamber (a cutaway is shown in Fig. 3.3) as in the case of the LaMBE, but with an additional sample storage chamber with a carousel for up to 12 samples. The load-lock in this case is much smaller, capable of reaching 5×10^{-8} Torr in a mere 30 minutes, thanks to the use of an integrated heating lamp to desorb water. Only one sample at a time can be introduced in this manner. From here the sample is transferred to the storage chamber, which also provides an interface with the preparation chamber of the HR-ARPES branchline [80].

The substrate is affixed to a sample holder by means of tantalum clips or a vacuum compatible bonding agent such as indium, ensuring good thermal contact with the holder. The holder is designed to facilitate transfer of the sample through the UHV environment, using manipulator arms in conjunction with storage racks.

In addition to capacitance pressure gauges, both chambers are fitted with residual



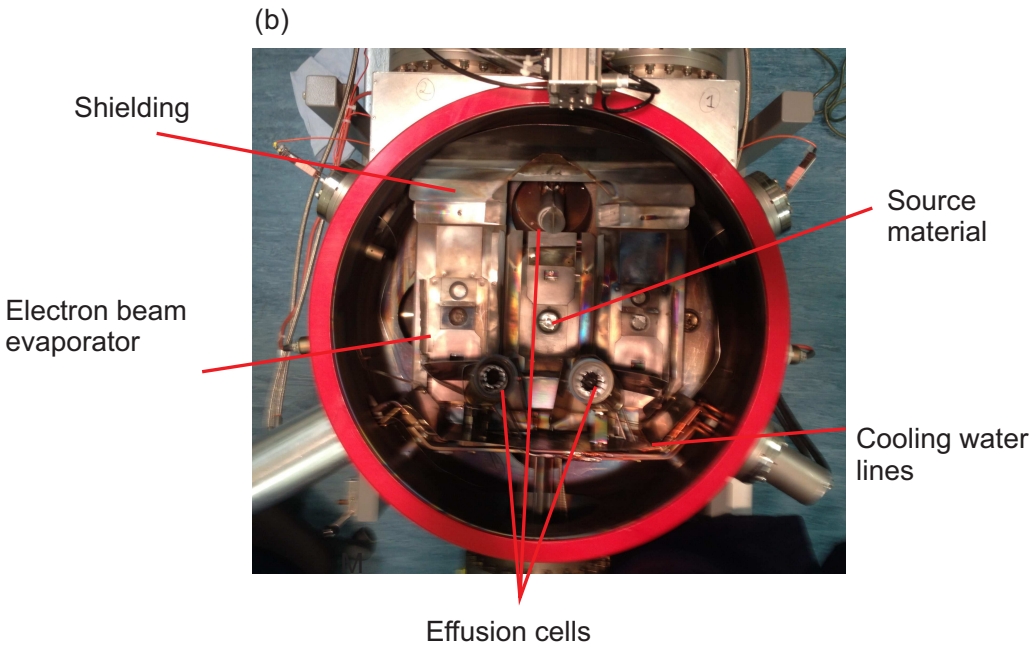


Figure 3.1: (a) Picture of the exterior of the LaMBE in the Clarendon, showing the growth and load-lock chambers, labelling key components. (b) Photograph of the interior of the growth chamber of the LaMBE during routine servicing, labelling the effusions cells and electron beam evaporators.

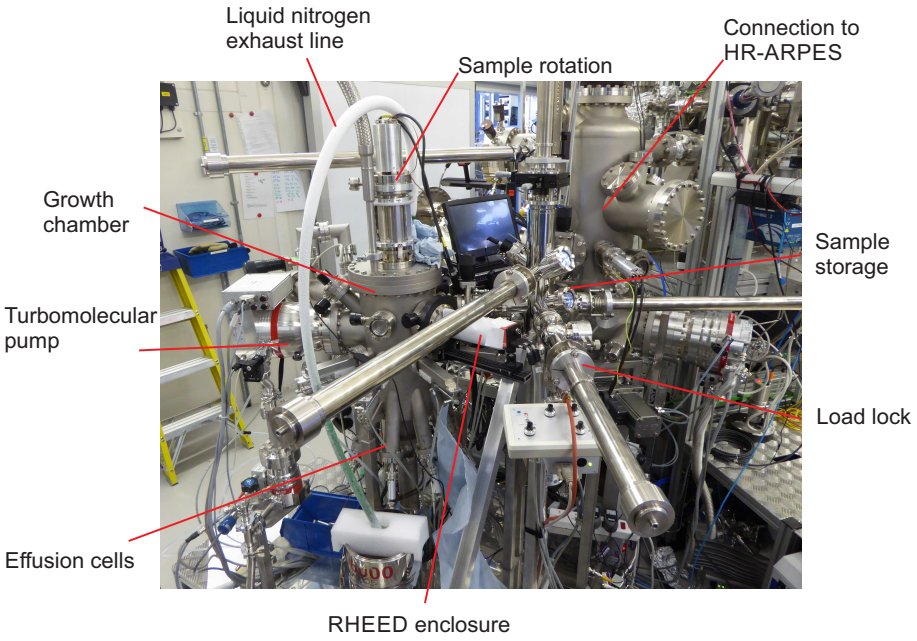


Figure 3.2: Photograph of the exterior of the μ-MBE, labelling the three chambers and their key components. The image captures the tight geometry of the chamber, which allows for fast pump times, but can be logistically challenging on occasion.

gas analysers (RGAs), which employ quadrupole mass spectrometry to determine which molecules are contributing to the background pressure of the system. This is particularly useful when using a new source material, as significant quantities of water, hydrogen and hydrocarbons can be present, and must be removed by protracted heating of the cell before sample growth can commence. The RGA identifies which impurities are present. An RGA can also function as a leak-tester, searching for leaks around new seals using He gas sprayed around the chamber exterior.

An effusion cell consists of a non-reactive crucible holding the desired source material, surrounded by a heater filament and monitored by a thermocouple in equilibrium with the crucible. Heat shields wrapped around the cell reduce radiative heating, both to reduce heat loss from the crucible and to protect the surroundings. A picture of a typical effusion cell is shown in Fig. 3.4. Temperature is controlled through the filament current, which resistively heats the crucible. Care must be

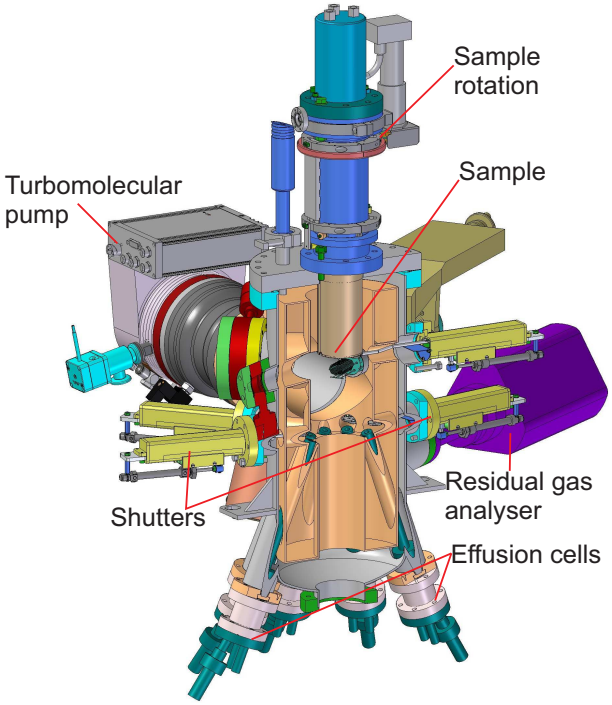


Figure 3.3: Cutaway view of the μ-MBE growth chamber, showing sample stage and heater (blue, top), linear shutters (yellow), residual gas analyser (purple) and effusion cells (turquoise, bottom). The cooling shroud fills most of the chamber volume. Figure from Ref. [78].

taken when ramping temperature in order to prevent damage to the cell, and to allow for different thermal conductivities at different temperatures. Effusion cells are monitored by electronic temperature controllers (Eurotherm) employing proportional-integral-differential control to maintain a stable temperature, and safe rates of change of temperature. Cells are typically water-cooled, though some chamber designs make use of the cryoshroud, or heat dissipation through connections to the chamber. When the source material inside the crucible is heated sufficiently, the material sublimes or evaporates, forming a gas that emanates from the mouth of the cell as a collimated beam, directed towards the substrate.

Deposition from electron beam evaporators follows a similar principle. The source material is placed in a water-cooled copper crucible, and a beam of electrons is directed onto its surface by the applied magnetic field provided by permanent magnets. A schematic of such an evaporator is shown in Fig. 3.5. This produces

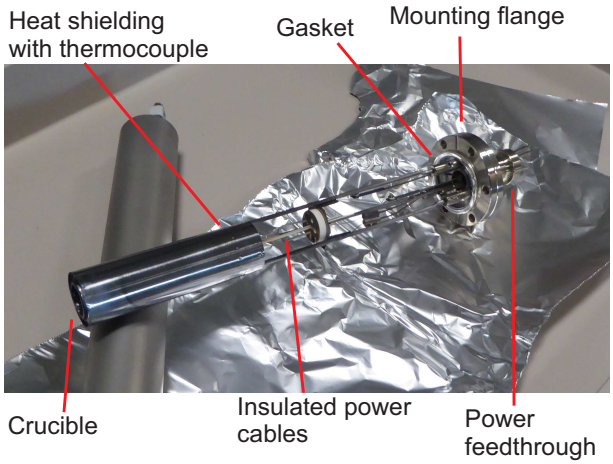


Figure 3.4: Picture of a typical effusion cell, showing key components such as heat shielding, crucible, and mounting flange.

significant localised heating, so the beam is swept across the sample to avoid boring a hole straight through materials which sublime rather than melt. Instead of using a physical focussing mechanism as with the long, thin crucible of an effusion cell, the electron beam evaporators use a cross-beam mass spectrometer to detect and focus the beam of atoms. This has the added advantage of rejecting impurities that may be present in the material, as the quadrupole mass spectrometer discriminates based on the mass of the atoms. However, this approach can be problematic when co-evaporating elements of similar mass, for example Ni and Fe, or an element that has an integer multiple of another's mass, for example Si and Fe.

During growth the substrate is heated to an elevated temperature of several hundred degrees Celsius to promote growth of high quality crystals. The increased temperature ensures that the material deposited by the incident molecular beams has sufficient energy to reorganise and form an ordered crystal structure. In the ideal case of perfect epitaxial deposition a complete monolayer of atoms is formed before growth of the next layer commences, so-called Frank-van der Merwe, or layer-by-layer growth [67]. This requires good matching of the lattice constants of the deposited material and the substrate, in order to alleviate epitaxial strain, as well as correct choice of growth rates and substrate temperature. Overheat-

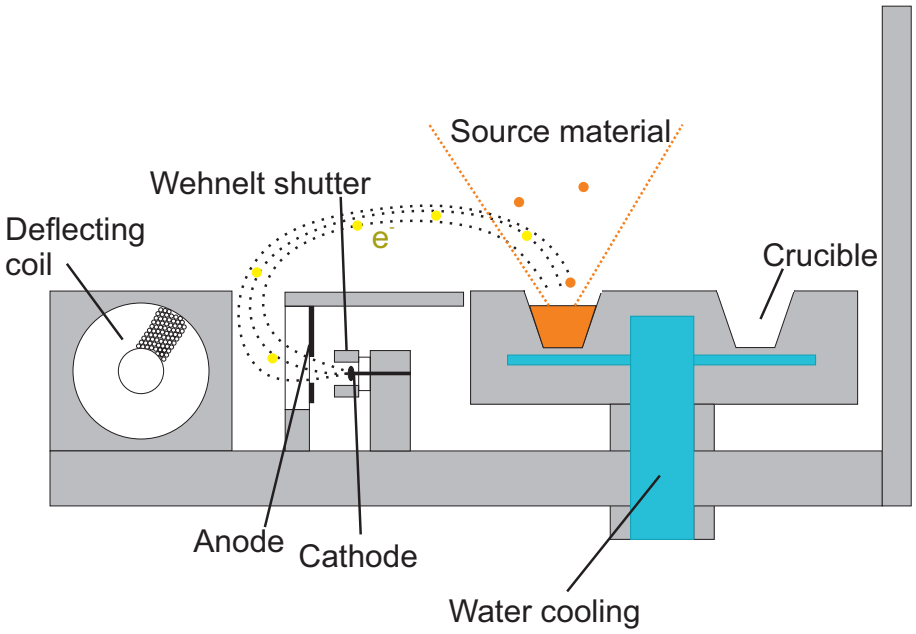


Figure 3.5: Diagram of a crucible electron beam evaporator system, showing the cathode (electron source), Wehnelt cylinder for electron beam focussing and deflector coil, which directs the electron beam towards the source material. Heating is highly localised, so beam position is swept over the extent of the source material to ensure homogeneous power distribution. The resulting molecular beam is focussed and monitored by a cross-beam quadrupole mass spectrometer.

ing can lead to undesirable reactions with the substrates or even sublimation of the deposited material back into the chamber. If the temperature is too low the atoms do not have sufficient energy to reorganise into the ideal structure, leading to 3D or polycrystalline growth, or even an amorphous material in the extreme case. The nature of the growth is monitored in real-time using RHEED; further details are given in section. 3.1.1. If the footprint of the molecular beams is of comparable size to the substrate, the sample stage is continuously rotated during growth to ensure an even thickness across the extent of the sample.

3.1.1 Reflection High Energy Electron Diffraction

To achieve high quality samples, it is important to be able to obtain information on crystal structure in real time throughout the growth process. RHEED is

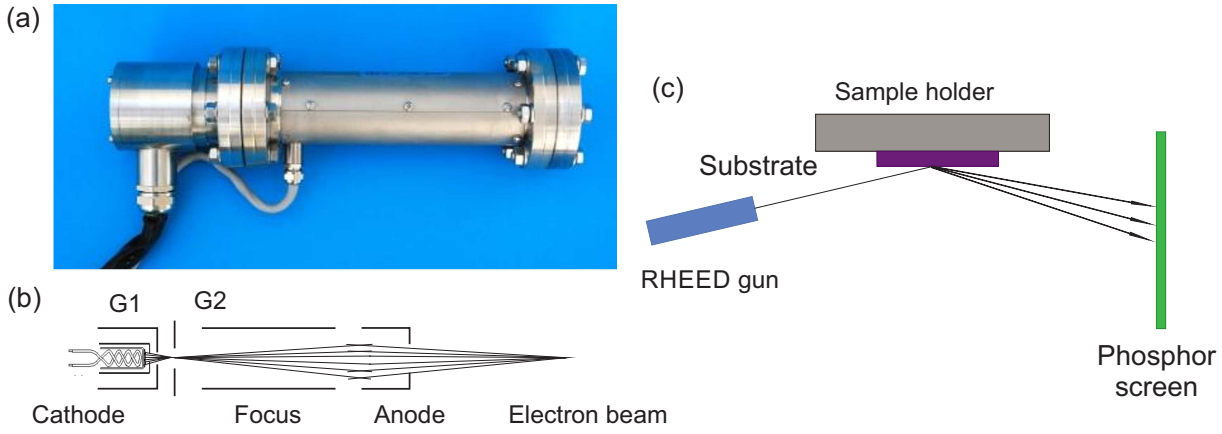


Figure 3.6: Gassler GmbH 15 keV compact RHEED gun (a) based on DN 40 CF for the μ-MBE system and design of the electron optics (b). Electrons are extracted from the hot cathode (H) by the accelerating voltage G2, while the beam current is controlled by the voltage at the small aperture Wehnelt cap G1. They are then focussed, and the beam is directed by magnetic coil pairs outside the vacuum. A schematic of geomerty of RHEED system is shown in (c). Figure after Ref. [78].

ideally suited to this purpose, as it provides information on crystal quality, surface roughness, growth mode, growth rate, reconstructions and alignment of the crystal.

A RHEED gun utilises thermal emission of electrons from a hot cathode, accelerated by a high voltage (typically tens of keV) and focussed by a magnetic lens, which also acts to steer the beam. The high energy electrons are incident upon the sample at grazing incidence, where they are diffracted by the crystal lattice, and impact upon a phosphor screen to produce an image of the diffraction pattern. This is typically monitored by a camera in a dark enclosure, to allow recording of RHEED patterns throughout growth. The arrangement for the RHEED in the μ-MBE is shown in Fig. 3.6.

Due to the geometry employed, the electrons probe only the first few monolayers of the sample, making RHEED a surface-sensitive technique. In this way, measurements over the course of growth sample the film at discrete points throughout the structure, rather than producing an average over the whole thickness. The

film surface functions as a two-dimensional grating for the incoming electrons. The periodic 2D lattice can be thought of as a series of lattice rods in reciprocal space, with constructive interference occurring when these rods intersect the Ewald sphere. This results in 2D streaks on the phosphor screen, rather than points, as the high energy of the electrons causes the diameter of the sphere to be significantly larger than the spacing of the rods and lattice vibrations and crystal imperfections cause the lattice rods to have finite thicknesses [67]. The de Broglie wavelength of the electrons is typically 0.1 Å. Example RHEED patterns for a $Co_{50}Fe_{50}$ film grown in the LaMBE are shown in Fig. 3.7.

While a high quality epitaxial film will lead to a RHEED pattern composed of thin streaks, in the case of samples with imperfections the RHEED pattern distorts. For example, if a 3D growth mode has lead to the formation of islands on the surface of the film, the streaks break up into discrete spots as the assumption of electrons diffracting through a perfect 2D lattice is no longer valid. Similarly, if the sample becomes polycrystalline the streaks are smeared out into concentric circles as the film becomes isotropic in the plane of the sample. Finally, if the film quality deteriorates further and all structure is lost in an amorphous film, the incident electrons are randomly scattered, and no discernible pattern is observed.

In this way RHEED analysis has great utility, allowing real time monitoring of sample quality throughout growth. Further information can be gathered by rotating the sample, as this allows the electron beam to interrogate different crystallographic directions, and identify the orientation of the film relative to the substrate.

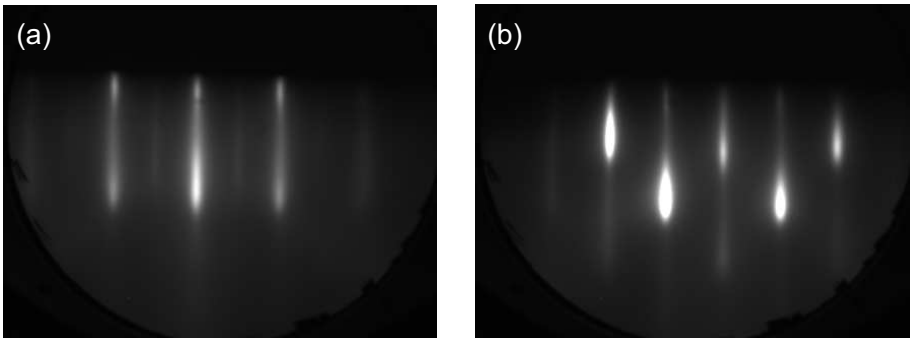


Figure 3.7: RHEED patterns taken from the surface of an as-grown epitaxial film of $Co_{50}Fe_{50}$ showing the (a) 0° and (b) 45° azimuths with respect to the [100] direction of the MgO (001) substrate.

3.2 Vector-Network Analyser Ferromagnetic Resonance

A vector network analyser (VNA) is a type of radio frequency (RF) equipment used to output and monitor RF signals of variable frequency and power. The Rhode & Schwartz ZVB20 VNA used in this thesis has a frequency range of 10 MHz to 20 GHz, and a dynamic range of 120 dB. In short, a VNA combines a microwave generator with a lock-in amplifier to provide phase-sensitive detection of its signals, allowing measurement of amplitude and phase of the microwaves. With two ports, each capable of acting as an emitter or a receiver, the VNA allows measurement of four S-parameters of the scattering matrix of what is connected. If the ports are labelled 1 and 2, the S-parameters are then S_{11} and S_{22} measuring reflection, and S_{12} and S_{21} measuring transmission. With its ability to quickly measure transmission across a wide frequency range, a VNA is an ideal tool to perform FMR experiments. Directing the microwaves through the sample, absorption is at a maximum when the FMR condition (see section 2.2.3) is met, and the VNA measures reduced transmission.

For FMR measurements, samples were placed face-down on a coplanar waveguide (CPW) of characteristic impedance 50 Ω, in the so-called flip-chip measurement

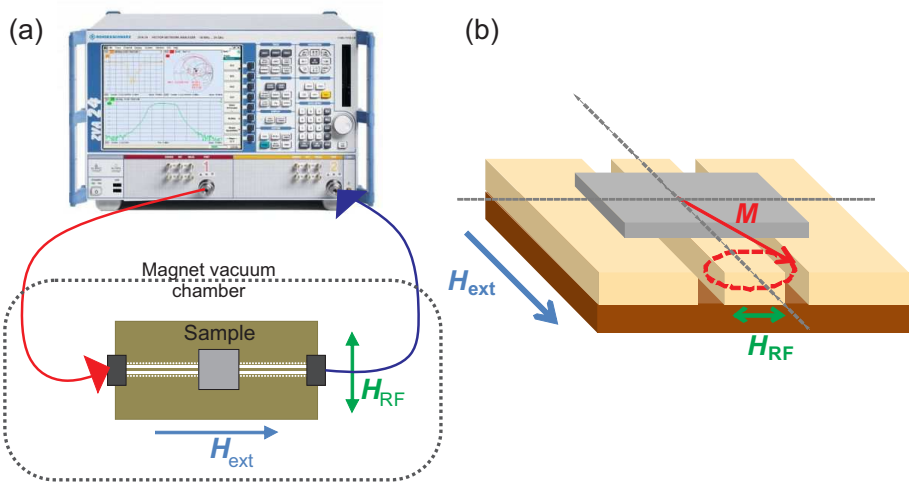


Figure 3.8: Schematic of the experimental VNA-FMR setup, showing (a) the VNA, sample mounted on the CPW and RF connection lines; and (b) detailed view of the sample mounted on the signal line of the CPW. The orthogonal DC external field and RF excitation field lead to precession of the sample magnetisation.

geometry [81]. The CPW has signal line width 1.1 mm, separated from the ground planes by a gap of 200 μm. As the metallic thin films under consideration are conducting, the CPW immediately beneath the sample was insulated using a single layer of teflon tape, to prevent electrical contact between signal and ground. Such a thin layer of teflon does not significantly attenuate the RF field produced by the microwave current. The CPW is connected to the VNA using coaxial cables with insulation and SMA (SubMiniature version A) connectors, to shield the microwaves from noise sources and prevent input and output lines affecting one another. End-launch connectors were used to contact the CPW. A diagram of the measurement setup, with the sample and CPW, is shown in Fig. 3.8.

All VNA-FMR measurements described in this thesis were performed in the Magnetic Spectroscopy Group's portable octupole magnet system (POMS, shown in Fig. 3.9), which allows the external static field to be applied in any direction. This has the great advantage of enabling the full angular variation of resonant frequency or linewidth to be measured without moving the sample. Due to the configuration of the driving torque, however, the signal quality decreases as the

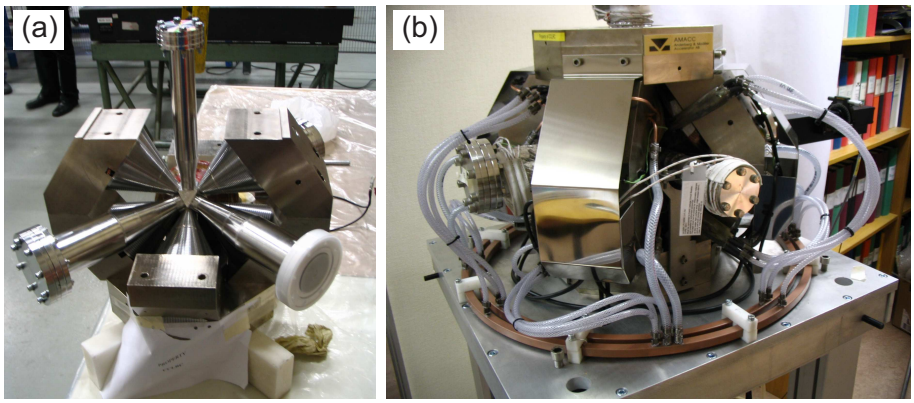


Figure 3.9: Pictures of the Portable Octupole Magnet System, showing (a) the exposed central six-way cross and magnet poles and (b) the whole assembly, with water cooling and external casing.

orientation of the external bias field and the RF stimulus approaches collinear. No FMR is observed when the external field is parallel to the RF, and maximum FMR is observed when they are perpendicular. Though POMS is capable of applying magnetic fields of up to 0.9 T, the highest field typically employed is ∼0.4 T, above which the resonant frequency of the films tend to exceed the 20 GHz limit of the VNA. The pole pieces of the magnet are situated around a 6-way vacuum cross, making the whole measurement system vacuum compatible, with two turbomolecular pumps backed by a scroll pump allowing it to reach 1×10^{-6} Torr in approximately one hour. This allows the chamber to be attached to a beamline for XMCD measurements (see below for more details), or cooled using liquid helium for low temperature FMR.

Measurements were performed by fixing the external field and sweeping the RF stimulus applied from 0.5 GHz to 20 GHz, recording the transmission. In this way the resonance frequency at a given field can be determined. However, due to losses in the cabling, the actual signal from the sample is not visible in such a measurement, and is instead obtained by subtracting this data from high field reference data, where the resonance of the sample is above 20 GHz. As the losses in the cabling are practically field-independent, this approach allows the resonance

to be identified. By putting together many measurements of transmission as a function of frequency at different fields, a field-frequency-transmission map showing the Kittel curves of the resonance can be built up, examples of such maps are shown in Fig. 3.10. While the VNA can be calibrated to remove the effects of the cabling, the necessity for the whole arrangement to be both vacuum compatible and portable makes this rather impractical. However, a significant improvement in data quality can be obtained by changing the approach. At a fixed frequency, the data quality of transmission as a function of external field is much better. Rather than requiring the frequency to be fixed and field to be swept (a much more time consuming process), high quality data can be obtained from field-frequency-transmission maps simply by searching for resonant field at a fixed frequency. This also makes determination of Gilbert damping from linewidth mathematically more convenient. Details of the procedure to extract resonance field and linewidth can be found in section 2.2.3. A series of such measurements performed at different angles of the applied magnetic field allows the anisotropy parameters of the film to be determined, using the Kittel equation, equation (2.15).

3.3 SQUID Vibrating Sample Magnetometry

A magnetometer measures the magnetisation of a material, as a function of temperature and applied external field. A vibrating sample magnetometer (VSM) operates by oscillating the sample under test within a set of pick up coils, wherein a current is induced proportional to the magnetisation. The sensitivity of a VSM is directly related to how accurately the voltage can be measured. A SQUID-VSM uses a superconducting quantum interference device (SQUID) for this purpose, providing an extremely sensitive probe of magnetisation. A diagram of the SQUID-VSM operating principle is shown in Fig. 3.11. The superconducting mea-

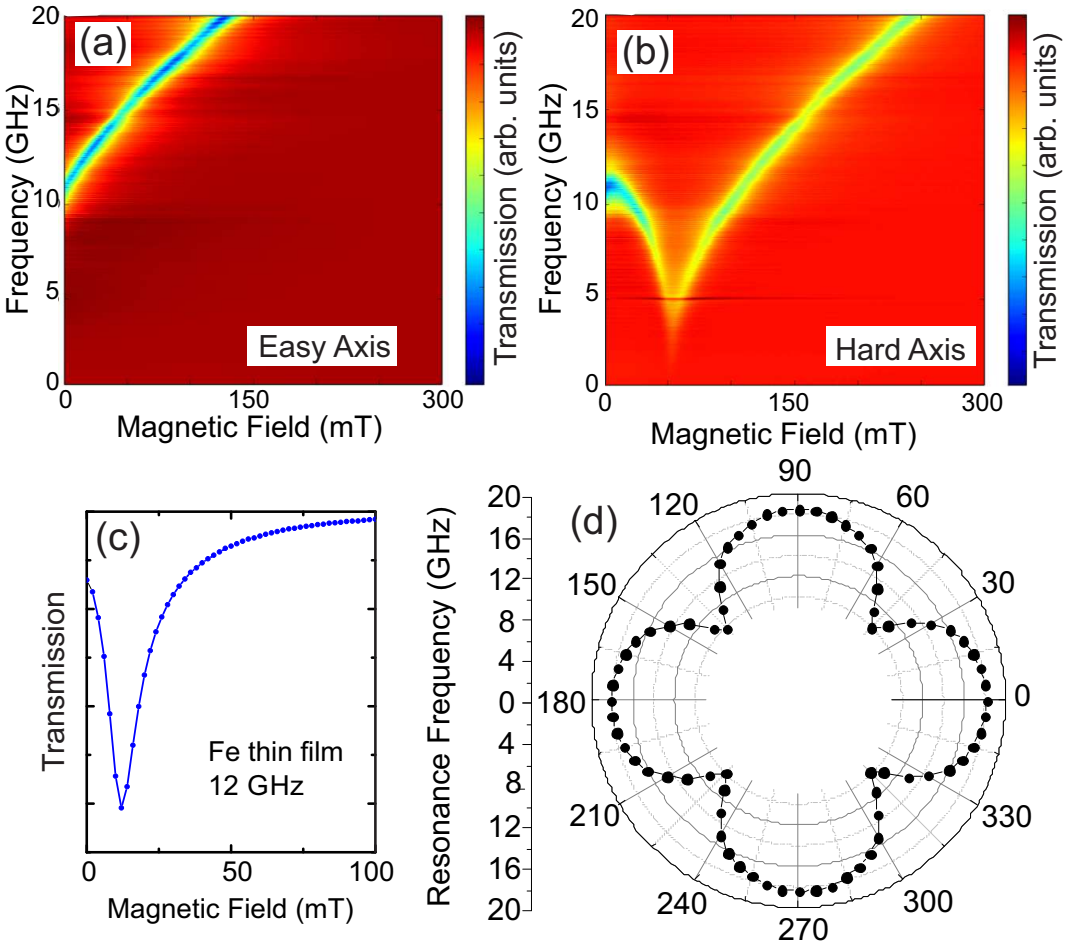


Figure 3.10: Example FMR measurements on a 65 nm Fe film. Top row shows field-frequency transmission maps for the easy (a) and hard (b) axes. A single field sweep at 12 GHz is plotted in (c), with the resonance evident at about 15 mT. Fixed field angle dependence of resonance frequency is shown in (d), with an external field of 100 mT. The four-fold cubic anisotropy is evident in the lobes at 90° increments.

surement coils, together with the SQUID input coil, form a closed superconducting loop, therefore the change of magnetic flux within the detection coils caused by oscillation of the sample produces a current in the detection circuit. This current is directly proportional to the change in magnetisation. The Josephson junction is a highly linear current-to-voltage converter, allowing accurate determination of the magnetic moment.

In this thesis SQUID-VSM measurements were performed in a Quantum Design MPMS 3, SQUID-VSM (situated on Beamline I10, Diamond Light Source), which

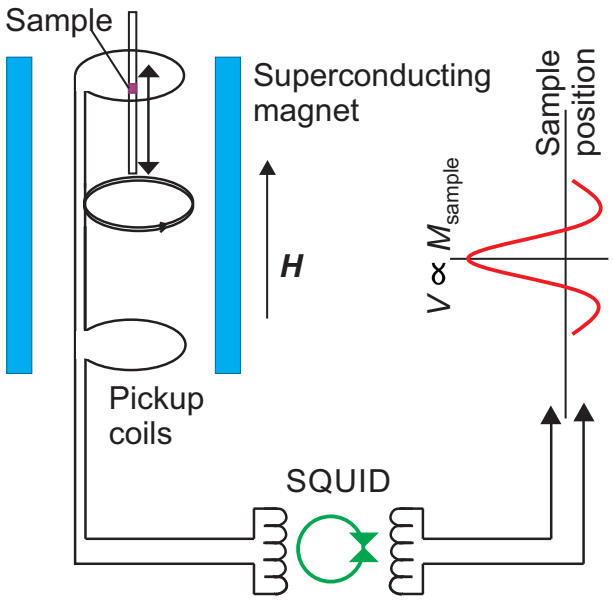


Figure 3.11: Schematic of a SQUID-VSM measurement system. Figure after Ref. [24].

is capable of applying a magnetic field up to 7 T along the axis of vibration. The MPMS also provides the ability to cool the sample to cryogenic temperatures of 1.5 K. Thin film samples were mounted on a quartz rod using GE varnish, these provide a diamagnetic background that must be removed from any measurement data before it can be properly analysed. This was achieved by linear fits to high-field regions of the hysteresis loop, or by comparison with measurements of bare substrates.

The primary SQUID-VSM measurements performed in this work were magnetic hysteresis loops to determine coercive field, saturation magnetisation, and, in the case of multilayers, the nature and strength of the static interlayer exchange coupling. Hysteresis loops were typically recorded along two in-plane directions, offset by 45°, to capture the magnetic reversal behaviour along the magnetocrystalline easy and hard axes.

3.4 X-Ray Magnetic Circular Dichroism

XMCD is an element- and site-specific probe of magnetic order, utilising circularly polarised synchrotron radiation at tunable energies. The theoretical background for the technique is described in section 2.4; this section will concentrate on practical aspects of performing the technique. XMCD measurements used in this thesis were performed at two synchrotrons: beamline I10 of Diamond Light Source (DLS) and beamline 6.3.1 of the Advanced Light Source (ALS). These are soft-xray beamlines, with a maximum energy on the order of 1.5 keV. The x-rays are easily attenuated, and all measurements must be performed at UHV.

A synchrotron is a machine that accelerates electrons to nearly the speed of light, whereupon they are directed into an orbit within a central storage ring and kept at a constant velocity. The storage ring is at ultra-high vacuum, and uses quadrupole and sextupole magnets to steer and focus the electron beam. Once in the ring, electrons can circulate for an extended period of time, typically on the order of hours.

A charged particle will emit radiation when it is accelerated, according to the relativistically-correct Liénard-Wiechert potential [36]. In a synchrotron this is used to produce high-intensity x-rays of a particular wavelength. There are two main methods for this process. In the first case, when the electrons encounter a curved section of the storage ring their path is altered by dipole (or bending) magnets; the resulting acceleration causes them to emit light. In the second case, an insertion device is placed on one of the straight sections of the ring, and uses an array of magnets to produce a periodic field that causes the electrons to oscillate perpendicular to the direction of travel. The periodicity of the perturbation correlates with the wavelength of the emitted light, when the Lorentz contraction of the relativistic electrons and the Doppler shift is taken into account. Insertion

devices use constructive interference of the emitted light to produce a beam of much higher intensity than bending magnets. In either case, the x-rays emitted from the electrons are directed out from the storage ring and into the beamline, which passes the light through a monochromator, focussing mirrors and diagnostics before reaching the experimental hutch, where the measurement equipment is situated.

The absorption of x-rays by the sample can be measured in several ways. In total electron yield (TEY) mode electrical contact is made to the sample surface and the photoelectrons generated by the incident photons measured. Due to the limited electron escape depth TEY is a surface-sensitive technique, with a probe depth in the soft x-ray regime typically on the order of ∼3-5 nm. The XMCD sum rules [38–40] can be readily applied to TEY data, making it a popular detection mechanism. Fluorescence yield (FY) mode uses a photodiode placed in the measurement chamber to measure photons emitted as electrons of lower binding energy fill the vacated core hole. It offers a significantly deeper probe depth than TEY, interrogating the entire profile of thin film samples. Unfortunately, FY amplitude is low in the soft x-ray region of the transition metal $L_{2,3}$ edges, and can be limited by geometrical considerations in chamber design. Finally, x-ray excited optical luminescence of the substrate offers an attractive detection method for suitable substrates. In this technique, x-rays that pass through the film are absorbed by the substrate, wherein the recombination of trapped excitons leads to emission of visible light. The MgO substrates widely used for growth of magnetic heterostructures have a particularly strong optical emission line, visible even to the naked eye. Placing a photodiode directly behind the sample therefore permits measurement of the film's XAS, as the intensity of x-rays reaching the substrate is dictated by the absorption within the film.

XMCD measurements on beamline 6.3.1 of the ALS use a 2 T electromagnet, where

the beam pipe passes through the pole pieces of the magnet, giving a field parallel to the beam. Beamline 6.3.1 uses a bending magnet, and is capable of fast energy scanning to quickly acquire XAS measurements at a fixed polarisation. XMCD is performed by reversing the magnetic field direction and repeating the XAS. The beamline is optimised for a single polarisation (usually circular negative), thereby achieving almost 100 % polarisation. XMCD measurements on beamline I10 at DLS use the Magnetic Spectroscopy Group's portable octupole magnet system, mounted behind the RASOR scattering chamber. POMS can apply a field of up to 0.9 T in any direction for short periods, with 0.5 T continuous field. In the case of I10, XMCD measurements were performed by reversing the magnetic field at every energy point.

3.5 X-Ray Detected Ferromagnetic Resonance

While VNA-FMR is a versatile characterisation tool, it is somewhat limited in that it provides a measurement over the whole sample. While this is not a problem when studying a single layer, it can be troublesome for the case of magnetic heterostructures such as spin valves, as it is unable to separate contributions from individual layers. This drawback can be addressed by combining the dynamic sensitivity of FMR with the element- (and thus layer-) selectivity of XMCD to perform x-ray detected ferromagnetic resonance (XFMR) [15, 29, 34].

The electrons in a storage ring of a synchrotron do not propagate in a continuous beam, rather they travel in bunches of a given pulse width. The x-rays delivered to the beamline have a repetition rate correlated to the arrival of bunches at the insertion device. At both Diamond and the ALS this repetition rate is 499.65 MHz, with a pulse width of 30 ps and 70 ps, respectively. Stroboscopic measurements of magnetisation dynamics can therefore be performed at integer multiples of this

frequency; enabling time-dependent precession of magnetisation to be determined at the picosecond timescale.

Static XMCD is defined as the difference between the two x-ray absorption spectra recorded with the helicity vector of the circular polarization parallel and antiparallel respectively to an external magnetic field [38]. The XMCD signal is proportional to the projection of the helicity vector, which is along the beam direction, $\hat{k}$, onto the magnetisation $\boldsymbol{M}$, such that $I_{\mathrm{XMCD}} \propto \hat{k} \cdot \boldsymbol{M}$. XMCD spectra generated by reversing either the magnetic field or the circular polarisation are equivalent. In XFMR, the energy and polarisation of the incoming light are fixed, and small oscillations of the magnetisation as the material undergoes FMR are measured by monitoring I_{XMCD}.

The sample is mounted on a CPW and driven by an applied RF field while under a static external field. At Diamond POMS is used (on beamline I10) to apply the magnetic field, while at the ALS the vector magnet on beamline 4.0.2 is used [82]. The use of a vector magnet is especially convenient, as it allows static XMCD to be measured with $\boldsymbol{H}_{\mathrm{ext}}$ parallel to the x-ray beam, and XFMR to be measured with $\boldsymbol{H}_{\mathrm{ext}}$ orthogonal to the beam and RF field, which is required for phase-resolved XFMR. A schematic of the measurement setup and detection circuit is shown in Fig. 3.12.

There are two approaches to measure XFMR, the time-averaged longitudinal geometry [34, 84], and the time-resolved transverse geometry [29]. Longitudinal XFMR detects the shortening of the magnetisation vector along the direction of the x-ray beam as the sample is driven at the FMR condition. It detects a signal of magnitude $\Delta M_{\mathrm{z}} = M_0[1 - \cos\theta] \approx \frac{1}{2} M_0 \theta^2$, with θ the cone angle of precession. The advantage of such a time-averaged measurement is that it does not require synchronising with the x-ray arrival, and can thus be performed at any frequency. It is useful when measuring overlapping resonances, but does not offer the more

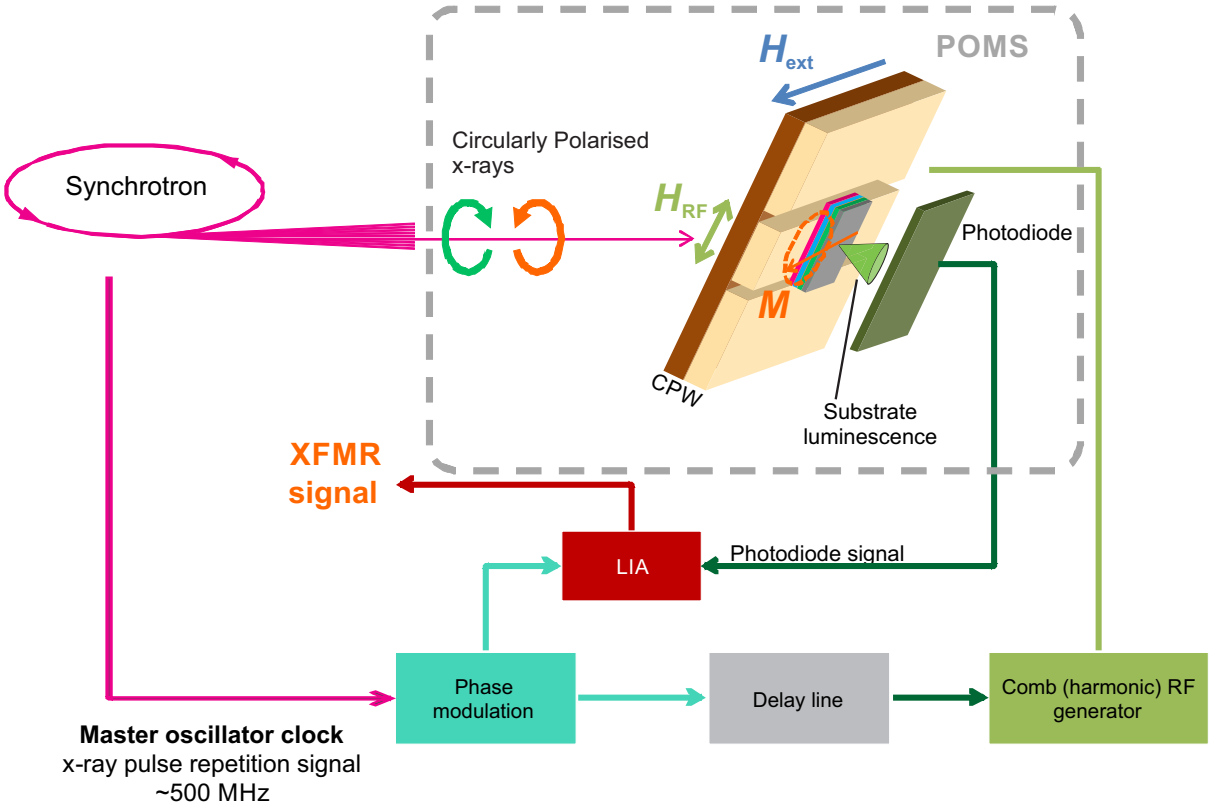


Figure 3.12: Schematic of the XFMR setup in transverse geometry used for the layer-specific characterization of the magnetization dynamics of the magnetic heterostructure. The sample is placed face-down on a CPW (within the vector magnet that provides the static magnetic field) and incident circularly polarized x-rays pass through a hole in the signal line. The precession of magnetisation of the stack about $\boldsymbol{H}_{\mathrm{ext}}$ is driven by the RF field, $\boldsymbol{h}_{\mathrm{RF}}$. The cone angle of precession is exaggerated for clarity; its typical magnitude is $\sim 1°$. The applied field $\boldsymbol{H}_{\mathrm{ext}}$ is perpendicular to both x-ray beam direction and $\boldsymbol{h}_{\mathrm{RF}}$. The different components of the XFMR electronic signal circuitry, RF excitation circuit, and x-ray detection system are also shown. The delay line enables the phase shifting of the RF oscillation with respect to the x-ray pulses with 0.5 ps step resolution. Figure taken from Ref. [83].

detailed phase information available to time-resolved measurements.

Throughout this work, time-resolved XFMR was employed as it provides greater insight into the precessional dynamics. In this geometry $\boldsymbol{H}_{\text{ext}}$ is applied perpendicular to the incident x-ray beam, and variation in I_{XMCD} probes the oscillating component of the Larmor precession with magnitude $M_{\text{y}} = M_0 \sin\theta \approx M_0\theta$, a factor of $2/\theta$ larger than that in the longitudinal geometry. On resonance, θ is typically 0.6°, meaning that the dynamic XMCD observed is approximately 1% of that observed in static measurements. Measurements are performed at close to grazing incidence, in order to maximise the projection of magnetisation precession along the direction of the beam.

For the stroboscopic measurements, the RF excitation must be a harmonic of the x-ray pulse frequency, limiting the available frequencies. The higher harmonics are provided by a comb generator (Atlantic Microwave) driven by the master oscillator of the synchrotron. Typical frequencies used in the measurements are 4, 8 and 10 GHz. A programmable delay line is used to phase-shift the delay between RF excitation (pump) and x-ray pulse arrival (probe), with a step resolution of ∼0.5 ps. However, the practical limit on step size is given by the jitter on the RF signal, which is usually ∼3 ps. Coupled with increasing power losses at higher frequencies, this imposes an upper limit on excitation frequencies of 12 GHz.

XMCD is detected by x-ray excited optical luminescence of the substrate, using a photodiode mounted directly behind the sample. Lock-in amplifier (LIA) detection of the time-varying signal is necessary to be able to measure the small amplitude of precession, using a LIA while modulating the phase of the driving RF through 180°. In this way the LIA measures the XMCD between opposite points on the cone of precession, ensuring the largest possible signal.

The x-rays are incident upon the sample through a small hole drilled in the signal

line of the CPW. The x-ray beam has an incidence angle of 35° with respect to the plane of the sample, ensuring that the XMCD probes in-plane precession. Smaller incidence angles would yield a larger signal, but are impractical as such rotation causes the footprint of the beam to be larger than the hole, or to be partially blocked by the CPW itself. Unlike VNA-FMR measurements, where the CPW is insulated beneath the sample, the film surface is in direct contact with both the signal and ground in XFMR. This maximises RF power delivered to the sample, thereby maximising cone angle and resulting XMCD. Connecting signal and ground in such a manner causes considerable microwave losses, particularly at high frequencies. This is not a serious concern, however, as long as cone angle of precession is maximised at the desired frequency.

Two types of measurement are possible in the transverse geometry. In the first, termed a field scan, the delay between RF excitation and x-ray arrival is fixed, while the magnetic field strength is swept. The delay is increased by one quarter oscillation, and the field sweep is repeated. This measures the real and imaginary components of transverse susceptibility, from which phase and amplitude of precession can be determined. This approach is used when the dynamic XMCD signal is large. In the second method, termed a delay scan, the static field is fixed and the delay is swept, producing a sine curve of precession of magnetisation. Amplitude and phase of precession can be obtained directly by fitting this curve. The field is then changed, and the process repeated, in steps over the resonance condition. This method is much more time consuming than field scans, but enables significantly weaker signals to be measured. With phase and amplitude of precession across resonance the relative contributions of each layer to the resonances can be determined, observing induced precession in the nominally off-resonance layer. Further, modelling of the AC magnetic susceptibility tensor allows the separate contributions of Gilbert damping and spin pumping damping to be directly

measured, more details of which can be found in section 5.

Chapter 4

Engineering of Magnetic Properties using Rare Earth Dopants

4.1 Motivation

The development of spintronic devices utilising spin transfer torque requires a mechanism for robust manipulation of both the static and dynamic properties of ferromagnetic (FM) thin films [6,7,57]. One attractive route for such optimisation is the use of rare earth (RE) dopants, which can significantly increase the Gilbert damping parameter of the film [85–87]. Due to the antiferromagnetic coupling of the RE impurities to the host lattice [88], there is an accompanying reduction in saturation magnetization (M_s) [18,87]. Much effort has been expended to develop this approach, from the perspective of device applications as well as fundamental investigations [18, 85–88]. Woltersdorf *et al.* [58] showed that the increase in damping can be explained by the "slow relaxing" RE impurity model developed by van Vleck and Orbach [89], whereby transitions between the exchange-split $4f$

RE states lead to a locally fluctuating field that acts on the FM $3d$ states. The interaction of this field with the magnetisation of the FM lattice acts to damp precession, and has an anisotropy related to the separation of the FM and RE states. Recently, Zhang *et al.* [88] and Luo *et al.* [87] showed that the dopants also modify the g-factor and the orbital- to spin-moment ratio, m_l/m_s, using x-ray magnetic circular dichroism (XMCD) on Gd-doped Fe films and Nd-doped $Ni_{81}Fe_{19}$, respectively. Similarly, Tb dopants can enhance the spin-orbit coupling of $Ni_{81}Fe_{19}$ thin films, leading to an increased magnitude of the anomalous Hall effect [90].

Previous studies, for example in Refs. [18, 86], found that the source of the magnetic moment in the RE impurity plays a key role in determining the damping enhancement. In the case of Gd, for example, the entire magnetic moment is due to spin, and no increase in damping was observed [18]. This work supports the notion that increased damping does not originate from a microstructural effect, as different dopants should nevertheless affect the crystal structure in the same way. However, subsequent studies, such as those in Ref. [88], have found evidence that Gd can increase the relaxation rate in $Ni_{81}Fe_{19}$ thin films, implying that there are additional complications.

This chapter focusses on a study into the static and dynamic properties of thin (5 nm) epitaxial Fe films, doped with low concentrations (0.1 – 5%) of Dy without loss of crystal quality. In contrast to previous works [87,88] this doping is achieved without loss of structural quality, aiming to develop a detailed understanding of the underlying physical processes. This also points towards future use of RE-doped ferromagnets in, for example, all-epitaxial magnetic tunnelling structures. The presence of Dy impurities acts to increase the Gilbert damping in the films, as has previously been demonstrated, but here the anisotropy of the increased damping is studied in greater detail, seeking to understand how the introduction

of rare earth impurities affects the relaxation rate within the films.

The structural properties of the films were initially characterised with RHEED and XRD, to confirm that the presence of dopants did not affect crystal quality. The static magnetic properties were studied with SQUID-VSM and VNA-FMR, with the latter also being used to determine the Gilbert damping. XMCD measurements were performed at the Fe $L_{2,3}$ absorption edges on beamline 6.3.1 of the Advanced Light Source, and the sum rules applied in order to determine the spin and orbital contributions to magnetic moment [19].

4.2 Sample Fabrication

Thin films of Dy-doped Fe were prepared in the LaMBE [77]. The MgO(001) substrates were solvent-cleaned in trichloroethylene, isopropanol, and methanol, then annealed in UHV at 700°C to obtain smooth surfaces. They were then cooled to 250°C for film growth. Fe and Dy (99.99% purity) were co-evaporated in the desired stoichiometry from an electron beam and effusion cell, respectively, to achieve $Fe_{1-x}Dy_x$ films with a thickness of 5 nm. The growth rate was 0.2 Å/s. The samples were then annealed at 350°C before an amorphous, 3-nm-thick Si capping layer was deposited at room temperature to prevent oxidation of the magnetic layer.

The growth rates were calibrated using a quartz crystal microbalance, and the Fe flux was kept constant using a cross-beam mass spectrometer. The sample quality was monitored using *in-situ* reflection high energy electron diffraction. The RHEED images in Fig. 4.1 show the annealed MgO(001) surface (a), and Dy-doped Fe films (c-h) exhibiting epitaxial growth. In (b) an undoped Fe film is shown for comparison, and (i) shows the amorphous Si cap. At 10% Dy content the RHEED pattern becomes much weaker and shows evidence of the formation of a secondary

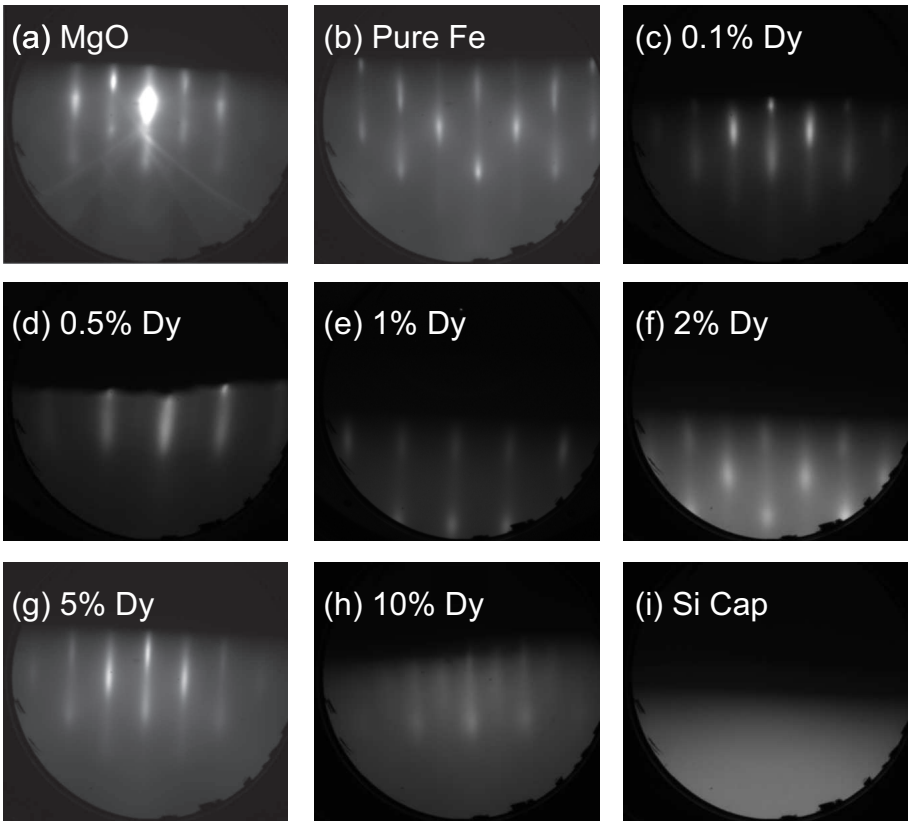


Figure 4.1: RHEED patterns measured during growth of the $Fe_{1-x}Dy_x$ thin film samples. (a) shows the annealed MgO (001) surface, while (b) shows a reference pattern of an undoped Fe thin film. Panels (c – h) show increasing percentages of Dy doping, from 0.1% up to 10%, at which point the weak pattern and secondary streaks indicate a degradation of crystal quality. The diffuse image from the amorphous Si cap is shown in (i).

phase. The deterioration of the RHEED pattern for $x \geq 0.1$ suggests that higher Dy concentrations will lead to polycrystalline or amorphous films. This doping limit coincides with the stoichiometry of $Fe_{17}Dy_2$, which is the first compound encountered in the binary phase diagram on the low Dy concentration end [91]. The epitaxial relationship of the system is $Fe_{1-x}Dy_x(001)[100]\|MgO(001)[110]$, i.e., the Dy-doped Fe lattice is rotated by 45° in-plane, as is also the case in undoped bcc-Fe films [92]. *Ex-situ* x-ray diffraction (XRD) was performed to characterise the structural properties of the films. Measurements were performed on a Bruker D8 four-circle diffractometer using Cu $K_{\alpha 1}$ radiation. The incident beam was restricted by a 0.4 mm beam limiting slit. Figure 4.2 shows a 2θ-ω scan

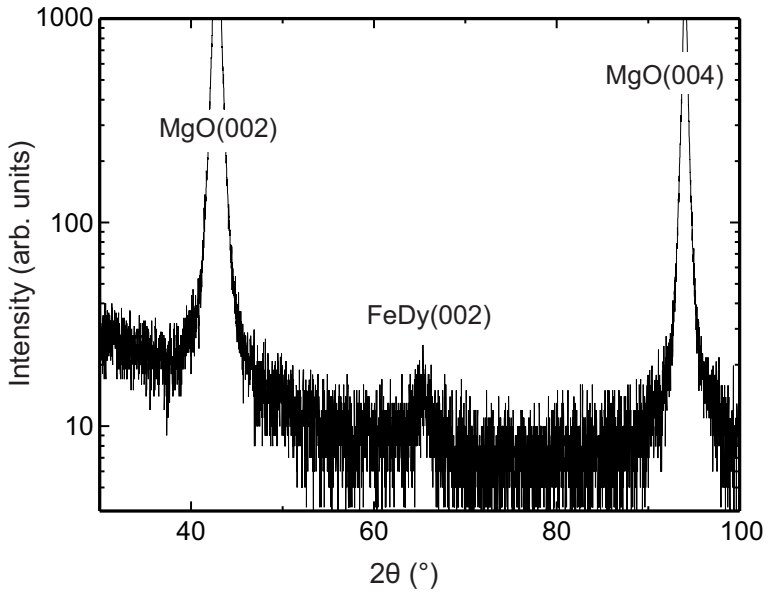


Figure 4.2: XRD spectrum for a 5-nm-thick $Fe_{0.97}Dy_{0.03}$ sample. The MgO substrate peaks and the film peak are indicated.

of a 5-nm-thick $Fe_{0.97}Dy_{0.03}$ sample.

4.3 Magnetometry and Magetocrystalline Anisotropy Parameters

Magnetometry measurements were carried out using a Quantum Design SQUID-VSM, determining saturation magnetization (M_s) and coercive field (H_c). Example measurements are shown in Fig. 4.3, displaying a reduction in saturation magnetization with Dy doping (also indicated in table 4.1), likely arising from an antiferromagnetic coupling of the Dy impurities to the host Fe lattice [88]. A slight increase in coercive field was also observed, possibly related to an increased availability of pinning sites during the domain reorientation process [93].

FMR measurements were performed for varying bias field strength and angle, with respect to the [100] axis. Figure 4.4(a) shows angular variation of resonance field at 15.5 GHz for films with varying Dy concentrations. The anisotropy constants

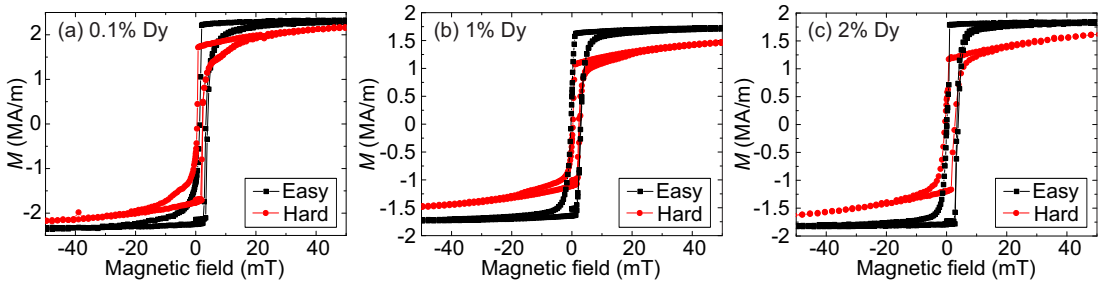


Figure 4.3: Hysteresis loops measured along the easy and hard axes of Dy-doped Fe thin films with Dy concentrations of 0.1% (a), 1% (b), and 2% (c).

Dy conc. %	$Kc_{\parallel}$ kJ/m^3	$Ku_{\parallel}$ kJ/m^3	g	M_s MA/m
0.1	58.4±0.1	0.15±0.09	1.80±0.01	2.18±0.01
0.5	58.3±0.1	0.74±0.05	1.81±0.01	2.17±0.01
1	46.1±0.1	2.1±0.1	2.02±0.01	1.70±0.01
2	47.3±0.1	2.20±0.08	1.99±0.01	1.70±0.02
5	52.6±0.1	2.7±0.2	1.88±0.01	1.84±0.04

Table 4.1: Magnetocrystalline anisotropy parameters and g-factor determined by fitting of angle- and field-dependent FMR frequency for samples with indicated Dy doping concentration, and saturation magnetization determined from SQUID-VSM measurements.

were determined using the Kittel equation (2.15). Example fits for selected Dy concentraions are shown in Fig. 4.4(b – d). Simultaneous fitting of the field and angle dependence of the resonance yielded the parameters listed in table 4.1. The reduction in saturation magnetization with Dy content is accompanied by a reduction in $K_{c\parallel}$. However, the in-plane uniaxial anisotropy (aligned along the [110] direction) is enhanced by a factor of almost 20 going from $x = 0.001$ to 0.05. As the substrate normal is perpendicular to the molecular beams during growth, this increase cannot be explained by kinematic considerations [94]. Such anisotropies have previously been observed in Fe grown on GaAs, and attributed to effects at the substrate-film interface [95]. Strain arising from substrate miscuts can also cause an enhanced uniaxial anisotropy [96], suggesting a slight modification of epitaxial strain with increasing Dy content.

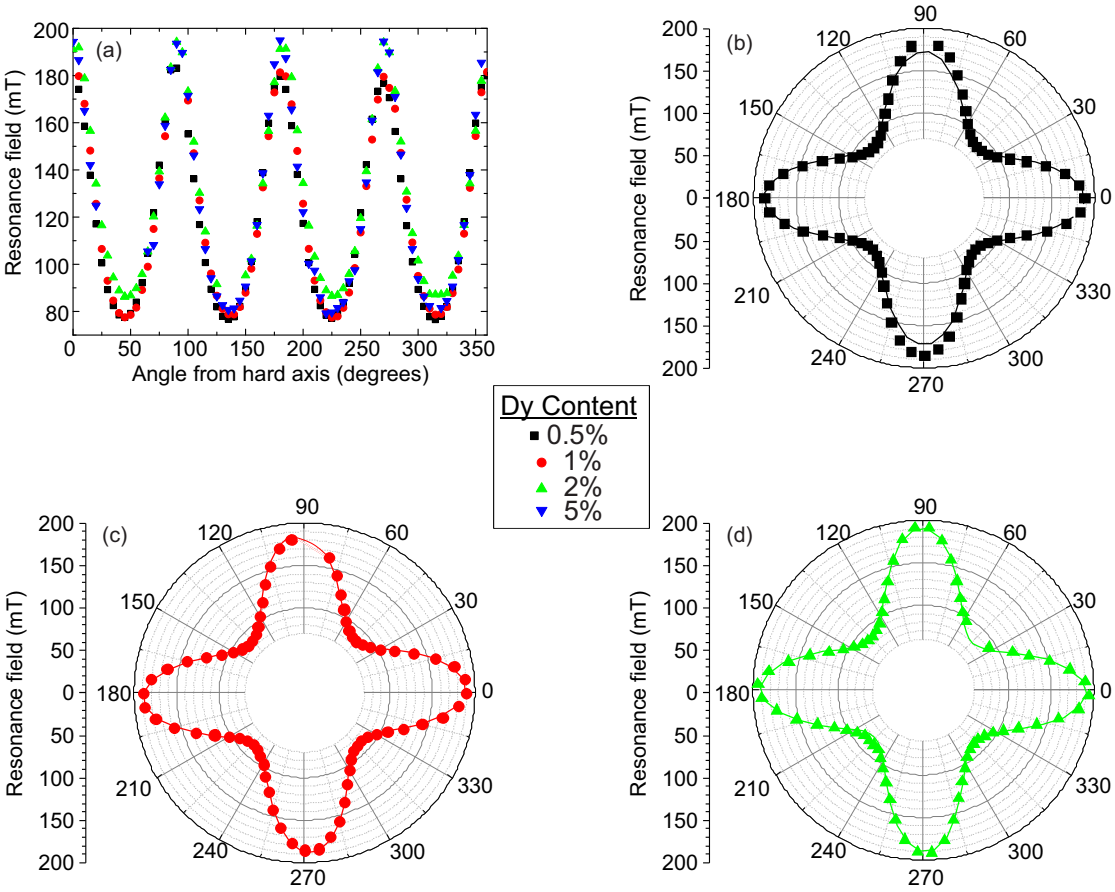


Figure 4.4: Angular variation of resonance field at 15.5 GHz for Dy-doped Fe, with panel (a) showing anisotropy for four concentrations of Dy: 0.5% (black squares), 1% (red circles), 2% (green triangles), and 5% (blue triangles). Panels (b,c,d) show angular variation of resonance field at 16 GHz for 0.5%, 1%, and 2%, along with fit lines produced by equation (2.15) and the constants listed in table 4.1.

4.4 Angle-Dependent Gilbert Damping

As discussed in section 2.3.1, the linewidth of resonance, ΔH, has both intrinsic (Gilbert) and extrinsic (two-magnon scattering and inhomogeneous broadening) contributions. Equation (2.21) relates the measured linewidth to ΔH_0, the inhomogeneous broadening, and α, the (dimensionless) Gilbert damping parameter. A slight increase in ΔH_0 with increasing Dy content was observed, indicative of increased sample inhomogeneity. This might be expected for a higher doping concentration, as the local structural quality degrades slightly with increasing Dy intercalation into the host lattice. Calculated Gilbert damping parameters for the

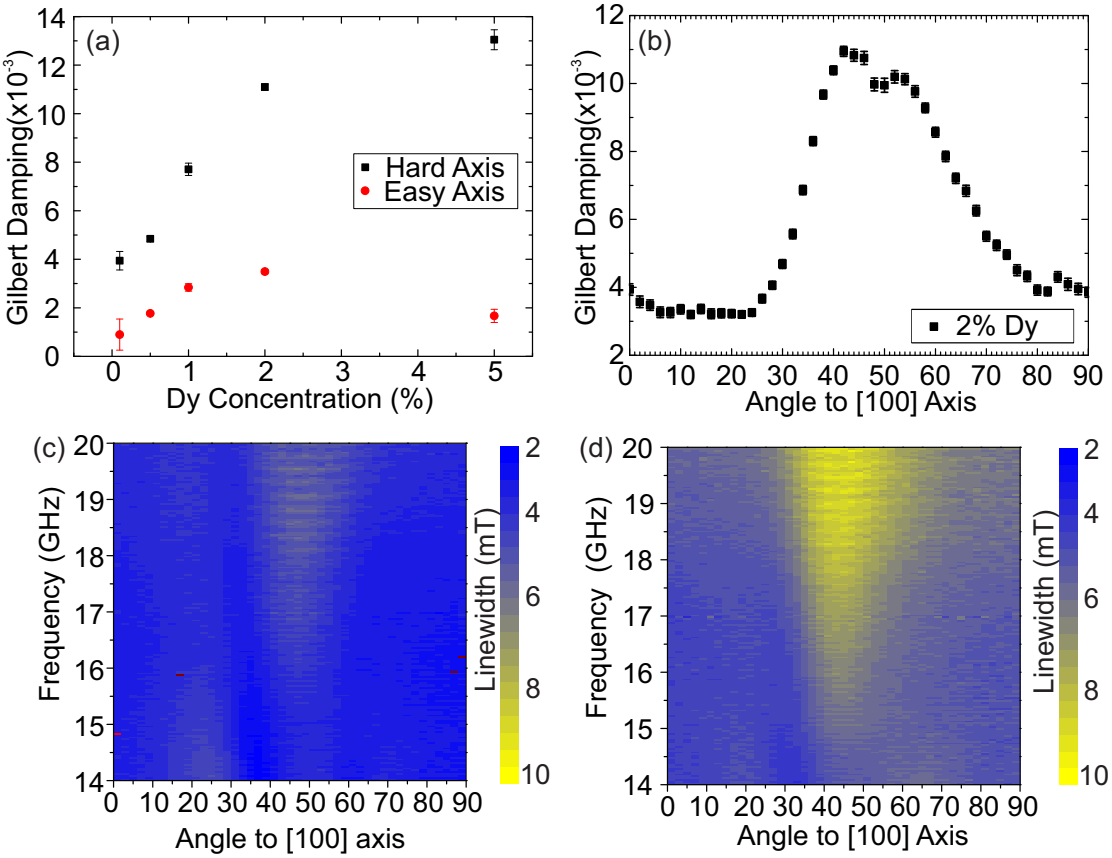


Figure 4.5: (a) Calculated Gilbert damping, α, along the easy [100] and hard [110] axes for samples with varying Dy concentration, showing both a strong anisotropic damping and an increase of this anisotropy with increasing Dy content. (b) Variation of Gilbert damping, α, for a sample with Dy content of 2%, as a function of bias field angle, showing a peak around the hard [110] axis. Lower panels explore this in more detail, showing the linewidth of the resonance as a function of bias field angle and driving frequency for (c) 0.5% Dy and (d) 2% Dy.

in-plane easy and hard axes are shown in Fig. 4.5(a), displaying the expected enhancement of damping with increasing Dy content. A total increase in damping along the easy axis of ∼200% is observed. This is significant, but much less than the several orders of magnitude increase that has been achieved in polycrystalline permalloy samples doped with, e.g., Tb [85]. However, the striking feature of the data set is the sharp increase in anisotropy of the damping brought about by dilute Dy doping, as shown in Fig. 4.5(b). For lower concentrations the damping along the hard axis is 2–3× higher than along the easy axis, but for $x = 0.05$ it is over 7× higher. Examples of the variation of linewidth with field angle and

frequency are shown in Fig. 4.5(c,d). The relatively sharp peak in the damping around the hard axis does not match the angular dependence that would be expected for other anisotropic damping processes, such as the smooth sine curve of two-magnon scattering [17].

The enhanced damping of such RE-doped films has its origin in the coupling of the Dy $4f$ electrons to the Fe $3d$ electrons mediated through the RE $5d$ orbitals. This interaction is anisotropic, however, so that the populations of the $4f$ states vary as the $3d$ moments undergo FMR, leading to a time-varying field due to the Dy relaxation time. Anisotropic damping enhancement has previously been observed in low temperature measurements of bulk YIG doped with rare earth atoms such as Tb or Y [97, 98]. The linewidth was found to reduce along orientations corresponding to near-crossings of the energy levels of the host lattice and the RE impurity [99]. This suggests that the increased anisotropy of damping originates from the same process as the damping enhancement itself, i.e., anisotropic coupling of the $4f$-$5d$ orbitals. The importance of using high quality, epitaxially grown samples is clear in this case; it allows a detailed study of angular dependence that is simply not possible with polycrystalline films. Further, it limits the role of defects (which can lead to inhomogeneous broadening) or other microstructural effects as crystal quality is preserved across the whole series. It is therefore important to study the effect this interaction has on the host Fe lattice in more detail, in order to determine whether the effects of the Dy are limited to the interatomic $5d$ states, or if the character of $3d$ moments themselves is changed.

4.5 Determination of Spin and Orbital Magnetic Moments

XMCD measurements were performed to determine the spin and orbital contributions to the total magnetic moment in Fe. This element-selective technique allows a more detailed study of the effect of Dy doping on the Fe moments [38]. Figure 4.6 shows typical XAS and XMCD results for the samples, measured in a field of 150 mT along the [100] (easy) axis. A clean metallic lineshape was observed in all cases, confirming that the samples are free of oxidation or other undesirable effects. Figure 4.6(c) shows the integrated XMCD signal for samples with $x = 0.005$, 0.02, and 0.05, illustrating the effects of increasing Dy content. The most pronounced effect is a reduction in intensity above the L_2 edge, indicative of a reduction in m_l/m_s ratio. The XMCD sum rules allow separate determination of the orbital and spin moments, using [39, 40]:

$$\begin{aligned} \frac{m_l}{n_h} &= -\frac{4}{3}\frac{q}{r} \\ \frac{m_s}{n_h} &= -2\left(\frac{3p-2q}{r}\right) \\ \frac{m_l}{m_s} &= \frac{1}{(9/2)(p/q)-3} \end{aligned} , \tag{4.1}$$

where n_h is the number of holes, p and q are the XMCD integrals over the L_3 and the combined $L_3 + L_2$ edges, respectively, and r the integral over the sum of positive and negative field spectra over the $L_3 + L_2$ edges [cf. Fig. 4.6(b,c)]. For more details, see section 2.4.1.

The extracted moments are shown in Fig. 4.7(a). The orbital moment per $3d$ hole drops with increasing Dy content, with a total reduction of almost 50% for $x = 0.05$. This demonstrates that the antiferromagnetic coupling of the Dy $4f$ to Fe

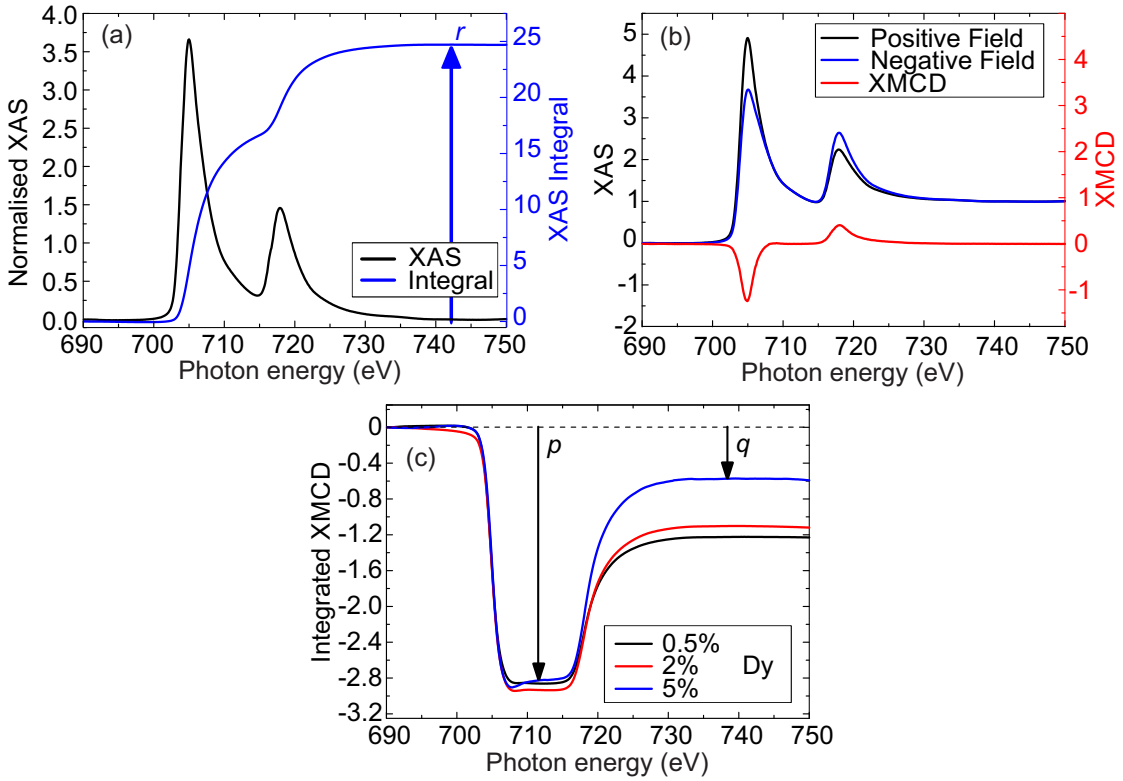


Figure 4.6: Fe $L_{2,3}$ x-ray absorption spectra. (a) XAS spectra for 2% Dy doping in a field of ± 0.15 T aligned parallel to the beam, and the difference spectrum, the XMCD. (b) Summed XAS and its integral for 2% Dy doping. A step function has been subtracted at each edge to remove the transitions to the s states, so that the integrated intensity is proportional to the d states. (c) Integrated XMCD spectra for 0.5%, 2%, and 5% Dy-doped Fe, showing a suppression of the L_2 edge, indicating a decrease in orbital moment with higher Dy content.

$3d$ through hybridized $5d$ states does not merely reduce the total moment of the sample, rather it causes a quenching of the orbital moment of the Fe itself. XMCD results were unchanged by relative in-plane orientation of the magnetization, suggesting that the anisotropy of the $4f$-$5d$ interaction is only important in dynamic measurements. The m_l/m_s ratio is shown in Fig. 4.7(b), along with the g-factor determined from fits to Kittel curves. The quenching of the Fe orbital moment leads to an overall reduction in m_l/m_s ratio of over 60%. This is in contrast to Gd or Nd, which enhance m_l/m_s [87, 88].

There appear to be two regimes as a function of Dy concentration. For >1%, the damping anisotropy becomes very large and the trend in the g-factor as determined

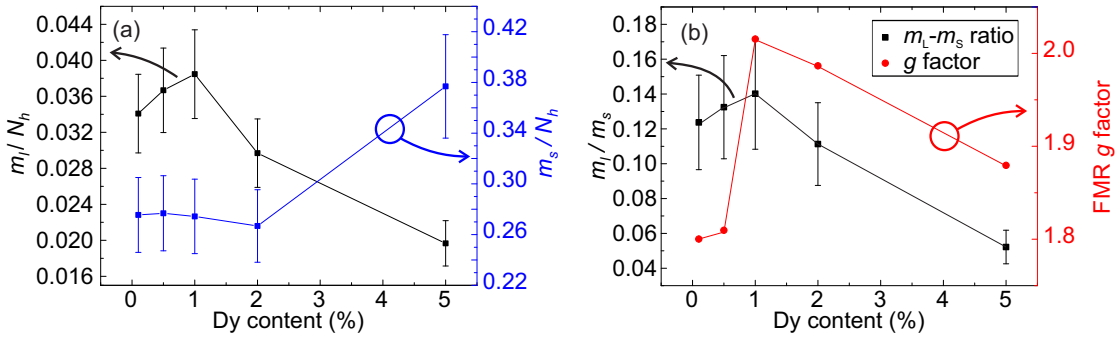


Figure 4.7: (a) Orbital and spin moments per hole as a function of Dy dopant percentage. A suppression of m_l and slight enhancement of m_s with increasing Dy is observed. (b) Comparison of m_l/m_s ratio as determined by element-selective XMCD, and the g-factor, as determined by FMR.

by FMR follows the m_l/m_s ratio. This most likely arises as the proximity of the Dy increases the spin-orbit interaction of the Fe. For <1% Dy the anisotropy is less pronounced and the m_l/m_s is significantly reduced, while the g-factor generally follows the trend, but at a much smaller rate. A possible cause is that the influence of the low concentration of Dy is insufficient to increase the Fe orbital moment, yet is still able to affect the FMR, through the effective field exerted by these slow-relaxing impurities.

4.6 Conclusion

This chapter has examined the modification of static and dynamic properties of ultrathin Fe films through dilute Dy doping. Crystal quality was preserved up to 5% Dy content, as determined by RHEED and XRD. It was found that the introduction of RE dopants reduces the saturation magnetisation of the film, most likely through antiferromagnetic coupling to the host Fe lattice, and that the cubic magnetocrystalline anisotropy parameter was similarly reduced. The uniaxial anisotropy parameter increased, however, perhaps as a result of epitaxial strain or hybridisation with the substrate. The Gilbert damping was enhanced by a factor

of three with increasing Dy content, as has been observed with many other RE-doped thin films. Using high quality MBE-grown samples allowed a detailed study of the anisotropy of the increased Gilbert damping, which has heretofore received only limited interest. A strong anisotropy of the damping develops, driven by the anisotropic interaction between the Dy $4f$ and interatomic $5d$ states, characteristic of the slow relaxing impurity model. This orientation dependence is important when considering spin-torque assisted magnetization reversal, or similar spintronic processes. Element-specific measurements showed that the Dy also modifies the properties of the Fe lattice itself, significantly reducing the orbital moment, and with it the m_l/m_s ratio. These results show that the interaction between FM films and RE dopants are more significant than previously anticipated, and demonstrate the possibility of fine-tuning magnetic properties of films for spintronic applications. More detailed calculations are required to elucidate the link between the increased Gilbert damping and modified orbital moment. A more detailed study of the temperature dependence of such effects could provide this information, as damping due to RE impurities has previously been observed to have a maximum at about 80 K, but how the anisotropy or spin and orbital moments are affected remains an open question. The techniques and results presented here show exploratory power of the combination of VNA-FMR and synchrotron radiation as tools to characterise the dynamic properties of thin films, as well as the nuanced role that growth, composition and exchange interactions can have on magnetodynamics. Later chapters will take these ideas further, studying spin transfer and coupling mechanisms that arise when two ferromagnets are in close proximity, as well as showing the profound insights that a combination of FMR and XMCD, XFMR, can offer.

Chapter 5

Micromagnetic Modelling of Coupled Magnetodynamics

5.1 Motivation

The field of computational micromagnetics is an expanding area of study that bridges the pure physics and device engineering communities, offering valuable insights into the behaviour of magnetic structures at the nanoscale, where experimental data is difficult to obtain due to the length scales involved, to understand complicated time-resolved magnetodynamics [100], or where analytical theory can not be applied. Here, it has been employed to gain a greater insight into the layer-resolved magnetodynamics of the heterostructures.

This chapter outlines the approach for conducting FMR simulations in the National Institute of Standards and Technology's (NIST) object-oriented micromagnetic framework (OOMMF) [101], discussing the case of isolated layers, finite-size effects and the insights offered by modelling of coupled layers. It then outlines in broad detail the approach for calculation of the AC susceptibility tensor, and how

this yields data comparable to XFMR measurements. The effects of static and dynamic exchange on the coupled magnetodynamics of spin valves are discussed, with particular reference to how their competition can distort phase features. With this foundation, it is then possible to move on to experimental measurements of such spin valve samples.

5.2 OOMMF

The first modelling approach employed was OOMMF: this package employs the finite difference approach to create a mesh of cuboids across a sample, then solves the LLG to compute the time evolution of magnetisation for a point at the centre of each cuboid. This makes OOMMF fast and well suited for samples of a regular geometry (such as thin films), but poor for objects with curves or sharp points. As OOMMF is a mature software package, its results are generally reliable, and it accurately incorporates effects such as magnetocrystalline anisotropy, static exchange coupling through the Ruderman-Kittel-Kasuya-Yosida (RKKY) interaction and magnetodynamics for FMR. When simulating FMR, this method yields the amplitude and phase of precession at a fixed field for a wide frequency range, with a spatial resolution governed by the exchange length and the spatial discretisation chosen by the user. It is somewhat limited, however, as it does not offer support for the spin pumping effect, which is a key consideration in many of the systems studied in this thesis. Nevertheless, OOMMF is a valuable tool when investigating ferromagnetic resonance [100, 102–105].

The most computationally expensive step in micromagentic is calculation of the demagnetising field.Analytical formulae only exist for uniformly magnetised ellipsoids, therefore OOMMF must numerically calculate the long-range demagnetisation field for every point in the mesh at every time step. This is, naturally, a

time-consuming process that places practical limits on the size of the simulated objects. Furthermore, when simulating magnetic heterostructures of out-of-plane (z) dimension ∼20 nm, the in-plane dimensions ($x - y$) must be several orders of magnitude larger, to preserve the thin-film behaviour of the demagnetisation tensor. Therefore, to achieve manageable simulation times a simplifying approximation is employed. The magnetisation is restricted to vary only with z, i.e. for a given slice within the depth-profile of the film the magnetization acts as a macrospin, and the film appears as a chain of spins in the z direction only. In this way, the number of points calculated by OOMMF is significantly reduced, and the simulation closely matches the thin-film approximation employed in the Kittel equation [equation (2.15)].

5.2.1 Simulating FMR

The simplest method to simulate FMR is to perturb the system and record the magnetisation dynamics as precession is damped away. If the perturbation is chosen correctly, the precession of magnetisation is composed of a sum of the supported normal modes. Resonance frequencies and corresponding modes can then be extracted by performing the Fourier transform on the recorded data.

When performing these simulations, the system was first prepared in a uniformly magnetised state by being allowed to relax under a static external field applied along the x direction. Next, a sinc ($\frac{\sin(t)}{t}$) pulse is applied out of the plane of the film used to excite precession of magnetisation over a given frequency range. The time evolution of the system was recorded over a period of 20 ns, over which time the magnetisation precession is described by sine curves of frequencies matching the normal (FMR) modes of the system, convoluted with a decaying exponential damping term due to energy loss. Fourier transforming the resulting data yields an FMR spectrum. Only the y-component of magnetisation is important in this

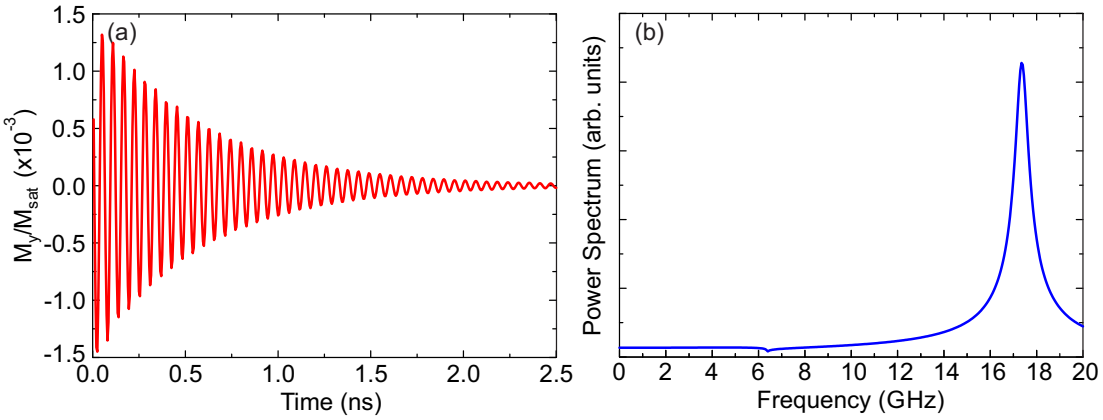


Figure 5.1: (a) Time-resolved precession of magnetisation for a thin $Co_{50}Fe_{50}$ film with a 120 mT bias field. (b) The associated FMR spectrum, showing the normal mode of uniform precession at 17.35 GHz.

process, as the external field is applied along x, and precession in z is distorted by the effects of the demagnetisation field. Figure 5.1 shows an example of such results for a thin CoFe film, with an external magnetic field of 120 mT applied along the easy axis. The precession is significantly damped over a period of 3 ns, with well-defined oscillations visible over this time. The Fourier transform yields a resonance peak at 17.35 GHz, the normal mode of precession of magnetisation, which corresponds to the FMR frequency.

5.2.2 Isolated Layers

The approach outlined above allows for straightforward simulations of isolated magnetic layers, using the thin film approximation of magnetization varying only in z to produce spectra corresponding to the macroscopic samples used in experiments. Figure 5.2(a) shows the simulated FMR spectrum for a 10 nm $Co_{50}Fe_{50}$ film, using materials parameters extracted from fits to experimental samples. As can be seen, the simulation accurately reproduces the resonance frequency from the experimental data, but somewhat over-estimates the linewidth of resonance. This demonstrates the strength of such modelling – it can quickly produce data

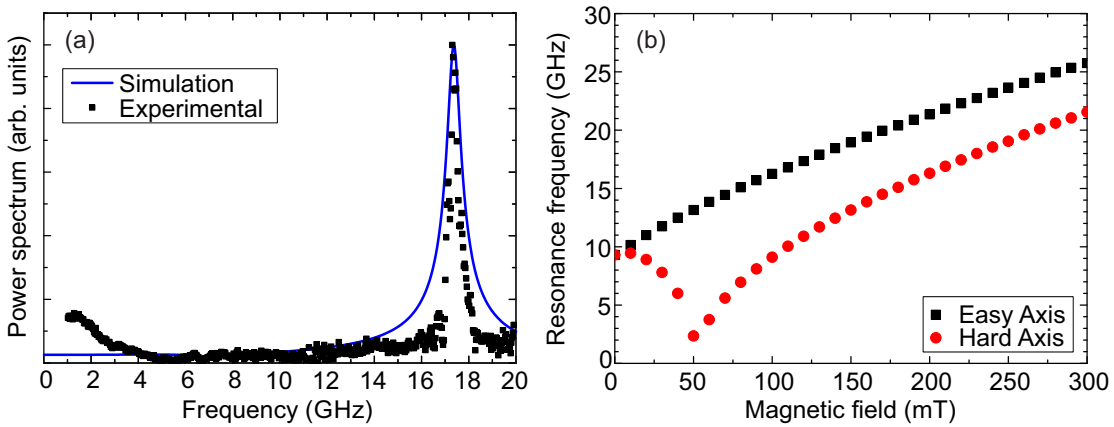


Figure 5.2: (a) Simulated (blue line) and experimentally measured (black squares) FMR spectrum of a thin CoFe film with an external bias field of 120 mT applied along the easy axis. (b) The calculated Kittel curve for bias fields of varying strengths applied along the easy (black squares) and hard (red circles) axes.

that is in good agreement with experimental results – but also the limitations, as a perfect match is not obtained.

The simulations are also capable of determining the angle-dependence of the resonance frequency, through OOMMF's implementation of uniaxial and cubic magnetocrystalline anisotropies. Rotating the defined easy axes with respect to the bias field replicates the effect of rotating the external field in the FMR experiments described in, for example, chapter 4. Example Kittel curves along the easy and hard axes of a thin $Co_{50}Fe_{50}$ film (also referred to as CoFe) are shown in Fig. 5.2(b), with the hard axes displaying the characteristic drop and recovery of resonance frequency caused by realignment of the magnetisation.

5.2.3 Coupled Layers

While simulating isolated layers can be useful as an alternate means to determine materials parameters, the primary relevance of micromagnetism for this work is the modelling of coupled multilayer structures. Since tools such as OOMMF discretise space to perform the simulation, they also offer a layer-selective probe of

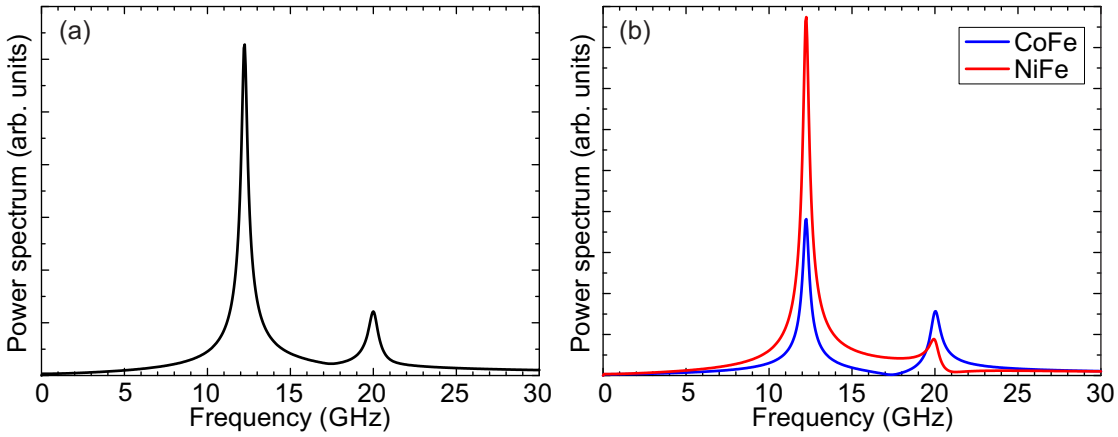


Figure 5.3: Simulated power spectra of a weakly coupled CoFe/NiFe bilayer with 100 mT magnetic field applied along the easy eaxis of the CoFe. The average magnetisation across the whole stack is shown in (a), while (b) shows the individual magnetisations of the CoFe and NiFe.

magnetodynamics and resonance frequencies. Conventional, lab-based FMR experiments have no means to directly separate the magnetic layers in a bilayer or spin valve structure, and synchrotron-based XFMR remains a time-consuming process.

Figure 5.3(a) shows the FMR spectrum for a $Co_{50}Fe_{50}$(10 nm)/$Ni_{81}Fe_{19}$(10nm) bilayer, coupled by a static exchange of 5×10^{-13} Jm^{-1} (compared to 2×10^{-11} Jm^{-1} within CoFe, or 1.3×10^{-11} Jm^{-1} within NiFe), with a magnetic field of 100 mT applied along the easy axis of the CoFe. The spectrum shows two resonance peaks, corresponding to the two magnetic layers. The lower frequency mode corresponds to the resonance of the magnetically soft NiFe layer, which has a lower saturation magnetisation, while the high frequency mode is driven by the harder CoFe, which has a higher saturation magnetisation. This is demonstrated in Fig. 5.3(b), which shows the layer-resolved power spectrum. The coupling causes there to be significant precession in the CoFe layer at the NiFe resonance condition (and vice-versa), as shown by the matching peaks in the power spectrum. It is notable that even at this comparatively weak coupling, the amplitude of CoFe is greater at the low-frequency mode than at the high-frequency mode that it primarily drives. A

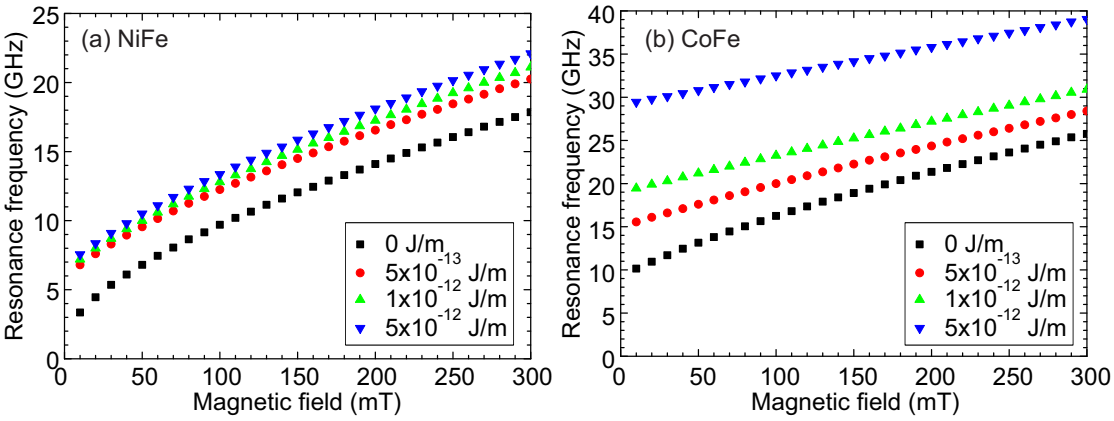


Figure 5.4: Simulated Kittel curves for a CoFe/NiFe bilayer thin film for several interlayer exchange coupling strengths.

strong interlayer exchange interaction causes the two layers to precess together.

The additional energy of the exchange coupling also increases the resonance frequencies relative to isolated layers. This is shown in more detail in Fig. 5.4, where the Kittel curves for the two resonance peaks are plotted as a function of the strength of the interlayer exchange coupling. In both cases the resonance frequency jumps sharply when weak static coupling is first introduced, but still produces a Kittel-like dispersion relation. However, as the coupling strength increases the behaviour of the two modes diverges. The low-frequency resonance, dominated by NiFe [Fig. 5.4(a)] does not significantly change as the strength of the interaction increases to $5{\times}10^{-12}$ Jm^{-1}. The frequency of the other mode, however, dominated by CoFe [Fig. 5.4(b)], continues to sharply increase, and the $\sqrt{H_{\mathrm{ext}}\left(H_{\mathrm{ext}}+M_{\mathrm{sat}}\right)}$ behaviour is replaced by a linear increase.

Plotting the power spectrum as a function of interlayer coupling strength [Fig. 5.5(a)] reveals that the amplitude of the high frequency mode decreases significantly as the exchange between the two layers increases. While the frequency increases, the energy of this mode decreases sharply, until it less than a tenth of the intensity of the lower resonance. Figure 5.5(b) shows the same information, but for the CoFe layer only. In the case of uncoupled layers, the CoFe resonance is at ∼16 GHz,

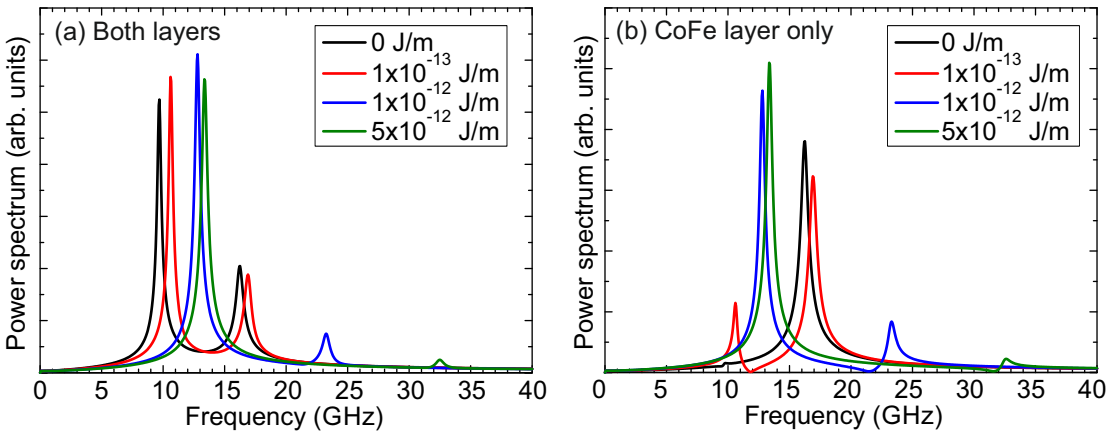


Figure 5.5: Simulated power spectra of a CoFe/NiFe bilayer with 100 mT magnetic field applied along the easy eaxis of the CoFe for varying interlayer exchange coupling strengths. The average magnetisation across the whole stack is shown in (a), while (b) shows the magnetisation of the CoFe layer only, demonstrating the change in character of the high frequency mode as the coupling strength increases.

and there is no peak at the resonance condition of the NiFe-dominated low mode. However, as the strength of the exchange coupling increases, the relative intensity of the two peaks reverses, until the CoFe spectrum is dominated by the low mode.

This change can be understood by considering the character of the two resonances changes when the strength of the interlayer exchange increases, as shown in Fig. 5.6. When the layers are fully decoupled, each of the peaks corresponds to the resonance condition of the isolated layers, and the amplitude of precession is uniform across each layer. This is shown in Fig. 5.6(a). When the coupling is sufficiently strong the low frequency mode becomes the dominant excitation of both layers. The phase of precession is uniform across both layers, and while the amplitude of precession is larger in the NiFe layer, there is a smooth transition across the interface. This is shown in Fig. 5.6(b). The high frequency mode, however, has the two layers precessing in anti-phase, and the interface functioning as a node in a standing wave that spans the extent of the bilayer. This insight demonstrates the value of micromagnetic modelling, as it directly confirms what would have only been implicit in lab-based measurements. The strength of the

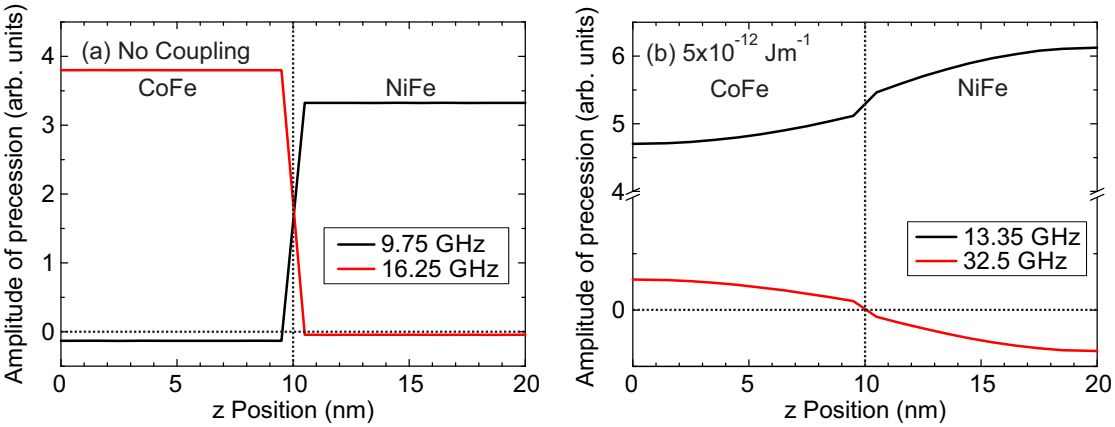


Figure 5.6: Complex exponential form of the Fourier transform of precession across the depth of the bilayer. The black and red lines correspond to low and high frequency modes respectively, with the case of no coupling shown in (a), and strong coupling of 5×10^{-12} Jm^{-1} shown in (b). Vertical dashed lines indicate the location of the interface between the two layers. Negative amplitude corresponds to out of phase precession.

coupling required to hybridise the two layers depends upon the materials used, and the relative thicknesses of the two layers.

While OOMMF can offer valuable insights in cases such as these, there is currently no way to incorporate the generation and absorption of pure spin currents. Although it could, in principle, be extended with this capability, it is in practice simpler to adopt an alternate approach which builds in spin pumping from the start. Although the fine spatial resolution offered by OOMMF is in an extremely useful tool for many investigations, the research presented here is concerned primarily with the modes of uniform precession excited in conventional FMR experiments, rather than any higher-order effects. Therefore, the higher spatial resolution is largely redundant, and an alternative technique must be used to model XFMR.

5.3 Determination of the AC Magnetic Susceptibility Tensor

The second modelling approach was chosen to address the need for a layer-resolved model of magnetisation dynamics that incorporates both static and dynamic exchange. To achieve this, the LLG was modified to include the required coupling mechanisms, then solved using a macrospin approximation and linearising in time. From this, the AC magnetic susceptibility tensor can be determined, yielding the amplitude and phase of precession at a fixed frequency for a range of fields, with a spatial resolution suitable only to separate the two layers. It is a fast calculation, but cannot offer the detailed spatial information that OOMMF does, nor does it truly reproduce the time-resolved magnetodynamics. However, it matches measured XFMR data closely, which offers the same information, at the same spatial resolution. Furthermore, calculations can be run extremely quickly, which is useful for the large parameter space afforded by systems with both static and dynamic coupling, alongside magnetocrystalline anisotropies and damping terms within the layers.

5.3.1 Dynamic Susceptibility of an Isolated Layer

The dynamic (AC) susceptibility tensor relates the response of the magnetisation of a material to a time-varying perturbation, giving the real and imaginary components of the precession of magnetisation. From this, the amplitude and phase of precession can be determined. The tensor is found using a solution of the Landau-Lifshitz Gilbert equation:

$$-\frac{\partial \boldsymbol{m}}{\partial t} = \boldsymbol{m} \times \left[\gamma \boldsymbol{H}_{\text{eff}} - \alpha \frac{\partial \boldsymbol{m}}{\partial t}\right], \tag{5.1}$$

with $\boldsymbol{m}$ the magnetisation vector, $\boldsymbol{H}_{\text{eff}}$, the effective field and α the Gilbert damping. This derivation uses the co-ordinate system outlined in Fig. 2.1, a thin film with z oriented out of the plane, an effective field $\boldsymbol{H}_{\text{eff}}$ composed of $\boldsymbol{H}_{\text{ext}}$ and $\boldsymbol{H}_{\text{anis}}$ oriented along x, an RF field $\boldsymbol{h}(t)$ oriented along y, and $\boldsymbol{H}_{\text{demag}}$ oriented along z. The magnetic field is homogeneous, and the magnetisation of the thin layer behaves as a macrospin with the equilibrium orientation aligned with $\boldsymbol{H}_{\text{eff}}$ along x. Since $\boldsymbol{h}(t) \ll \boldsymbol{H}_{\text{ext}}, \boldsymbol{H}_{\text{anis}}$, the perturbations are small and the magnetisation vector $\boldsymbol{m}$ can be approximated:

$$\boldsymbol{m} = \hat{x} + m_{\text{y}}\hat{y} + m_{\text{z}}\hat{z}, \tag{5.2}$$

The effective field is:

$$\boldsymbol{H}_{\text{eff}} = (H_{\text{ext}} + H_{\text{anis}})\hat{x} + h(t)\hat{y} - M_{\text{s}}m_{\text{z}}\hat{z}. \tag{5.3}$$

Substituting these definitions into the LLG yields:

$$\begin{aligned} 0 &= m_y\left(M_{\text{s}} - \alpha\frac{\partial m_z}{\partial t}\right) - m_z\left(h - \alpha\frac{\partial m_y}{\partial t}\right) \\ -\frac{1}{\gamma}\frac{\partial m_y}{\partial t} &= m_z(H_{\text{ext}} + H_{\text{anis}} - M_{\text{s}}) + \frac{\alpha}{\gamma}\frac{\partial m_z}{\partial t} \\ -\frac{1}{\gamma}\frac{\partial m_z}{\partial t} &= \left(h + \frac{\alpha}{\gamma}\frac{\partial m_y}{\partial t}\right) + m_y(H_{\text{ext}} + H_{\text{anis}}), \end{aligned} \tag{5.4}$$

with γ the gyromagnetic ratio, and α the Gilbert damping. These equations are then linearised by disregarding products of m, h, and using harmonic solutions of the form $m(t) = m\exp(-i\omega t)$, $h(t) = h\exp(-i\omega t)$. This yields the following pair

of equations:

$$\begin{aligned} 0 =& -\frac{i\omega}{\gamma} m_y + m_z \left(H_{\text{ext}} + H_{\text{anis}} - M_{\text{s}} - \alpha \frac{i\omega}{\gamma} \right) \\ h =& - m_y \left(H_{\text{ext}} + H_{\text{anis}} + \alpha \frac{i\omega}{\gamma} \right) + \frac{i\omega}{\gamma} m_z. \end{aligned} \tag{5.5}$$

Which can be written in matrix form as:

$$\begin{pmatrix} 0 \\ h \end{pmatrix} = \begin{pmatrix} -\frac{i\omega}{\gamma} & H_{\text{a}} \\ -H_{\text{b}} & \frac{i\omega}{\gamma} \end{pmatrix} \begin{pmatrix} m_y \\ m_z \end{pmatrix}, \tag{5.6}$$

where:

$$\begin{aligned} H_{\text{a}} &= H_{\text{ext}} + H_{\text{anis}} - M_{\text{s}} - \alpha \frac{i\omega}{\gamma} \\ H_{\text{b}} &= H_{\text{ext}} + H_{\text{anis}} + \alpha \frac{i\omega}{\gamma}. \end{aligned} \tag{5.7}$$

This can be succinctly written as $\boldsymbol{h} = \hat{A}\boldsymbol{m}$, and since $\boldsymbol{m} = \chi \boldsymbol{h}$, the susceptibility tensor, χ, is found by inverting the matrix, $\hat{A}$. As the microwave field is aligned purely in y, only χ_{yy} is required for modelling purposes. χ_{yy} is in general a complex number, with the real part giving the portion of the oscillation that is in phase with the driving frequency, and the imaginary part being the component that is out of phase by 90°. Thus the amplitude and phase of χ_{yy} correspond to the transmission of microwaves as measured by VNA-FMR, or the amplitude and phase of precession of magnetisation as measured by XFMR.

Figure 5.7 shows the results of modelling of a thin Fe film, with the magnetic field applied along the magnetocrystalline easy and hard axes. The peaks in amplitude of precession in Fig. 5.7(a) correspond to the peaks in absorption of microwave power observed in VNA-FMR. Several features are notable here. First, the hard axis has two resonance peaks at 4 GHz, due to the reorientation of the

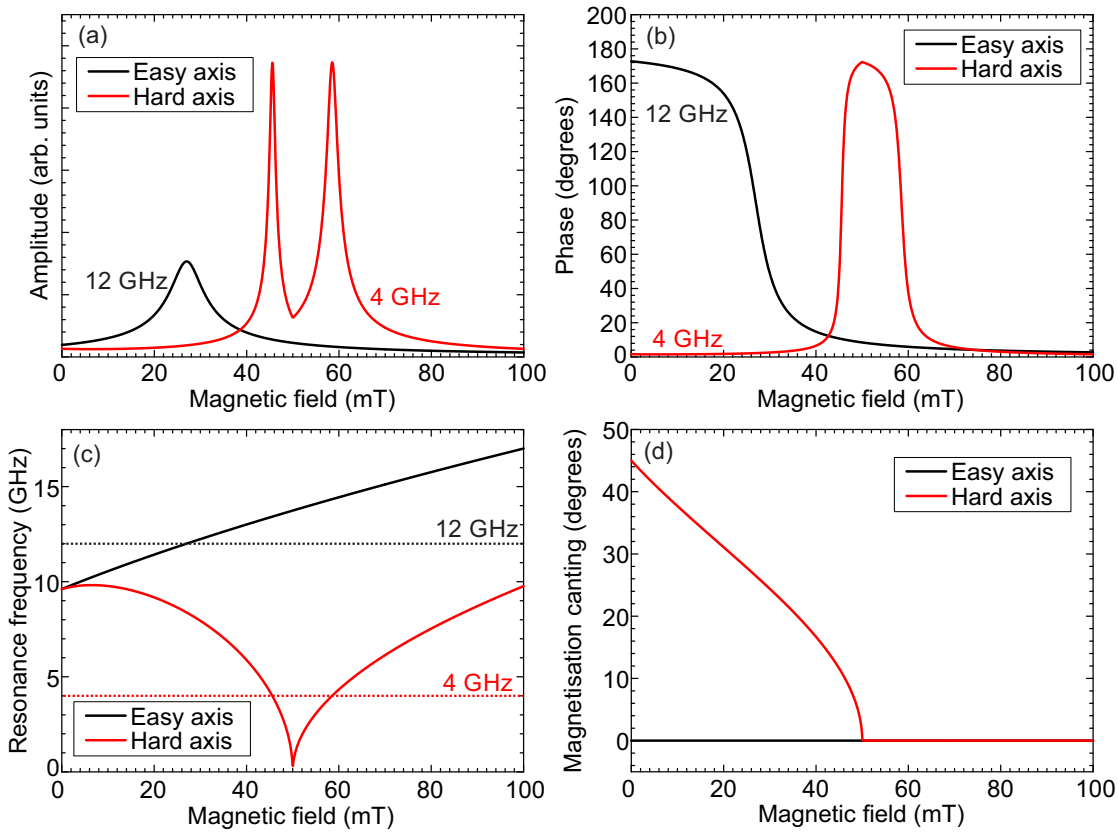


Figure 5.7: Dynamic susceptibility results for a thin Fe film with the magnetic field applied along the magetocrystalline easy (black) and hard (red) axes. Amplitude and phase of precession are shown in (a) and (b), with driving microwave frequencies of 12 GHz and 4 GHz, respectively. The calculated resonance frequency is plotted in (c), with dashed lines showing the frequencies simulated in (a,b). The magnetisation may cant away from the external field due to the effective field within the sample, the deviation of magnetisation from the external field is shown in (d).

magnetisation as the external field exceeds the anisotropy field. Secondly, the easy axis peak at 12 GHz is broader than the hard axis peaks. This is because of the linear relationship between resonance linewidth and excitation frequency, as given by equation (2.21).

The phase of precession of magnetisation is plotted in Fig. 5.7(b), with the easy axis showing the phase shift of full 180° across resonance expected from a simple harmonic oscillator model. Along the hard axis there are two phase shifts, again arising due to the reorientation of magnetisation. This "forwards-backwards"

phase feature always occurs along a hard axis, though if the peak separation is small the feature is compressed, and may not complete the full 180° shift. This can make interpretation of XFMR data rather challenging, and renders the classification of a resonance as an "optic" or "accoustic" mode complicated.

Figure 5.7(c) shows the Kittel curves for the thin Fe film calculated from the prefactor of the inverse susceptibility matrix. At zero applied magnetic field the results along both axes agree. The curves diverge as the magnetic field increases, and the external field begins to compete with the anisotropy field. Examining the kink in the hard axis data yields an anisotropy field of ∼50 mT. The equilibrium orientation of magnetisation was calculated by minimising the free energy derivative, equation (2.10), and is plotted in Fig. 5.7(d). Along the easy axis the magnetisation is always collinear with the field, however along the hard axis the rotation of magnetisation can be easily observed.

This illustrates the benefits of this modelling approach: it quickly produces results that correspond well to experimental findings, and gives a good breadth of information by returning susceptibility, resonance condition and canting angle simultaneously. Further, as it is a direct simulation of an ideal FMR experiment, one does not have to worry about shape effects, choice of initial perturbation or time discretisation. However, the very fact that it is an idealised FMR experiment means that there are some shortcomings; it assumes a perfect microwave excitation, infinitely sharply defined crystalline axes, and homogeneous magnetic field. Further, its spatial resolution is limited to a macrospin approximation of each layer, as it has no way of dealing with the magnetisation variations within a ferromagnet. In this respect it is inferior to OOMMF. However, as this is the same level of spatial resolution obtained by XFMR, this drawback is less important. Therefore, for its versatility, speed and ease of use, and close correspondence to experimental techniques, determination of the dynamic susceptibility is the

preferred modelling approach.

5.3.2 Modelling Dynamic and Static Exchange

The magnetic heterostructures studied in the following chapters are based on the spin valve or tunnel junction concept: two ferromagnets separated by a thin non-magnetic barrier, that may be conducting or insulating. For a suitable barrier thickness and material, two coupling mechanisms exist. Dynamic coupling (introduced in section 2.3.3) occurs when the magnetisation of one or both of the layers is in motion, and proceeds through the indirect interaction of spin pumping. The mathematical formulation of spin pumping is discussed in more detail in section 2.3.3. The dynamic interaction modifies the LLG with the addition of damping and anti-damping terms, which codify the additional linewidth of resonance due to loss of angular momentum, and the induced precession caused by absorption of angular momentum.

Static coupling was introduced in section 2.2.4, recall the definition [31, 35]:

$$\beta_i = \frac{A_{\text{ex}}}{M_{\text{s}}^i d^i} \cos(\phi_{\text{M}}^i - \phi_{\text{M}}^j), \tag{5.8}$$

with A_{ex} the interlayer exchange constant, d the thickness of the magnetic layer, and ϕ_{M} the equilibrium orientation of magnetisation. The sign of A_{ex} determines whether the interaction favours parallel (positive) or antiparallel (negative) alignment.

With the addition of these two coupling mechanisms, the LLG for a trilayer system

becomes [35]:

$$-\frac{\partial \boldsymbol{m}^i}{\partial t} = \boldsymbol{m}^i \times \left[\gamma^i \boldsymbol{H}^i_{\text{eff}} + \boldsymbol{\beta}^i M^j_{\text{s}} \boldsymbol{m}^j - (\alpha^i_0 + \alpha^i_{ii})\frac{\partial \boldsymbol{m}^i}{\partial t}\right] + \alpha^i_{ij} \boldsymbol{m}^j \times \frac{\partial \boldsymbol{m}^j}{\partial t}, \tag{5.9}$$

where superscripts denote magnetic layer, and $\boldsymbol{H}^i_{\text{eff}}$ is the effective field acting on layer i. The intrinsic Gilbert damping is α^i_0, while α^i_{mn} are spin source ($m = n$) and spin sink ($m \neq n$) terms. This equation is solved in the same manner as in section 5.3.1. For full details of the derivation and associated assumptions, refer to appendix A.

The presence of these coupling mechanisms alters the magnetodynamics of the on- and off-resonance layer. The static coupling shifts the resonant field of both layers, as it functions as an additional field term in the Kittel equation. Spin pumping, on the other hand, broadens the resonances by providing an additional energy loss mechanism. However, the most important change is the precession induced in the off-resonance layer, wherein the exchange interactions transfer energy between the two layers. This leads to changes in both the phase and amplitude of precession, with the phase being the more sensitive probe.

Figure 5.8 shows the off-resonance precession induced at 7 GHz in a 5 nm $Co_{50}Fe_{50}$ layer, coupled to a 5 nm $Ni_{81}Fe_{19}$ layer by the static interaction. The shifts in resonance frequency relative to the resonance of an isolated NiFe layer (dashed black line) are due to the increased energy in the system from the static interaction. A (weak) interaction of 1×10^{-6} Jm^{-2} has little effect, leading to an almost flat line across the resonance. When this is increased to 1×10^{-5} Jm^{-2} there is a weak bipolar feature in the amplitude, and a unipolar feature in the phase, along with a shift in resonance frequency of about $\sim$5 mT. If the same coupling strength is used, but the interaction is made antiferromagnetic, the resonance shifts in

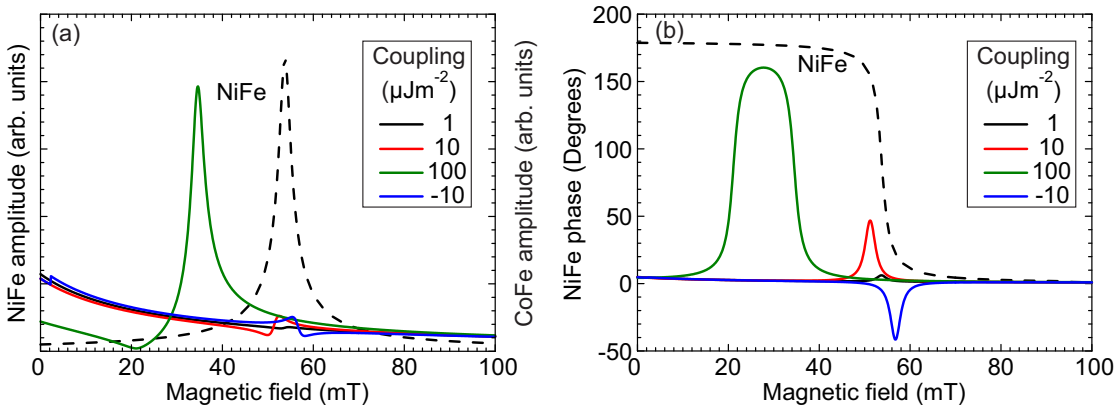


Figure 5.8: Effects of the static exchange interaction on the amplitude (a) and phase (b) of induced precession at 7 GHz for a trilayer of 5 nm $Co_{50}Fe_{50}$ and 5 nm $Ni_{81}Fe_{19}$, separated by a thin barrier of unspecified material. The dashed line is a reference for an isolated NiFe layer, while the solid lines are the CoFe layer. Precessional amplitude in the NiFe layer is approximately 10 times higher than that of the CoFe layer.

the opposite direction, and both the amplitude and phase features reverse sign. Finally, a strong interaction of 1×10^{-4} Jm^{-2} leads to a large shift in resonance frequency, and a phase feature that approaches 180°. There is also an asymmetric peak in the amplitude, rather than a pure bipolar lineshape, as the layers become more strongly hybridised.

Figure 5.9 shows the off-resonance precession induced at 7 GHz in a 5 nm $Co_{50}Fe_{50}$ layer coupled to a 5 nm $Ni_{81}Fe_{19}$ layer by the dynamic interaction. At the NiFe resonance condition, a pure spin current is emitted from the NiFe layer, crossing the barrier and being absorbed by the CoFe, where it induces precession through the spin-transfer torque. For simplicity, perfect transmission and absorption are assumed. The dynamic interaction leads to a unipolar feature in the amplitude, just visible above the tails of the resonance in the CoFe (which is at negative field at this excitation frequency). The peaks get larger with increasing spin pumping, and also significantly wider as the interaction also broadens the NiFe resonance, thereby widening the range over which the dynamic interaction takes place. A similar effect can be observed in the phase, where there is a bipolar feature. Again,

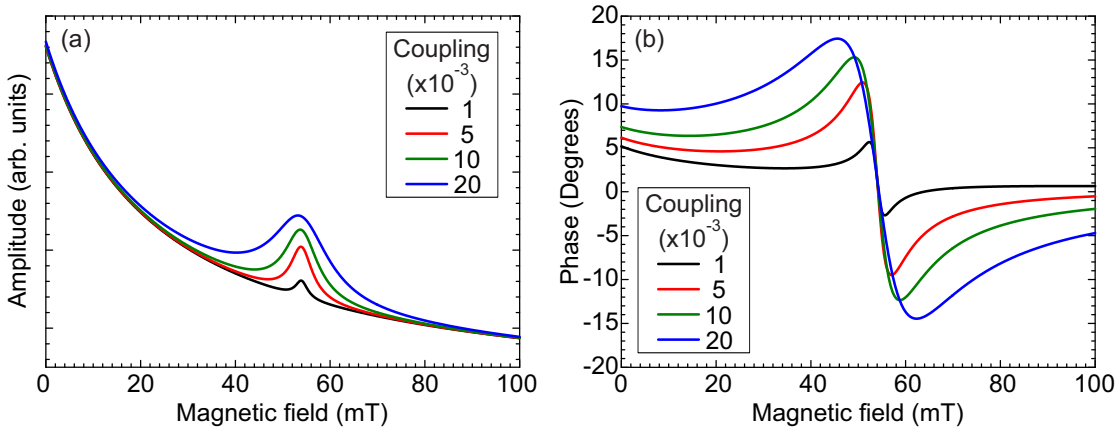


Figure 5.9: Effects of increasing spin pumping on the amplitude (a) and phase (b) of induced precession at 7 GHz for a trilayer of 5 nm $Co_{50}Fe_{50}$ and 5 nm $Ni_{81}Fe_{19}$, separated by a thin barrier of unspecified material. Coupling strength is defined here as the additional damping experienced of the NiFe, α_{22}^2, and the anti-damping term for the CoFe, α_{12}^1.

this broadens and increases in amplitude as the interaction strength is increased. Nevertheless the zero crossing is always at the same value, as the link between damping and resonance field is extremely weak.

In most real systems, however, both interactions will be present, and careful modelling is required to separate their relative contributions. In broad terms, the two interactions can be considered additively, as each of them imposes a certain change to the amplitude and phase of the induced precession, as shown in Fig. 5.10. Here, the distinct lineshapes of each coupling mechanism can be observed, before they are combined to lead to asymmetric Lorentzians in both the amplitude [Fig. 5.10(a)] and phase [Fig. 5.10(b)] of precession. However, the combination of the two exchange interactions can be more complicated. For example, if the on-resonance layer has a rather low intrinsic linewidth, such that even a small amount of spin pumping represents a significant contribution to the total linewidth. In this case the phase feature associated with static coupling is limited by the linewidth of the resonance, so the broadening due to spin pumping might lead to an effective increase in the impact of the static coupling too.

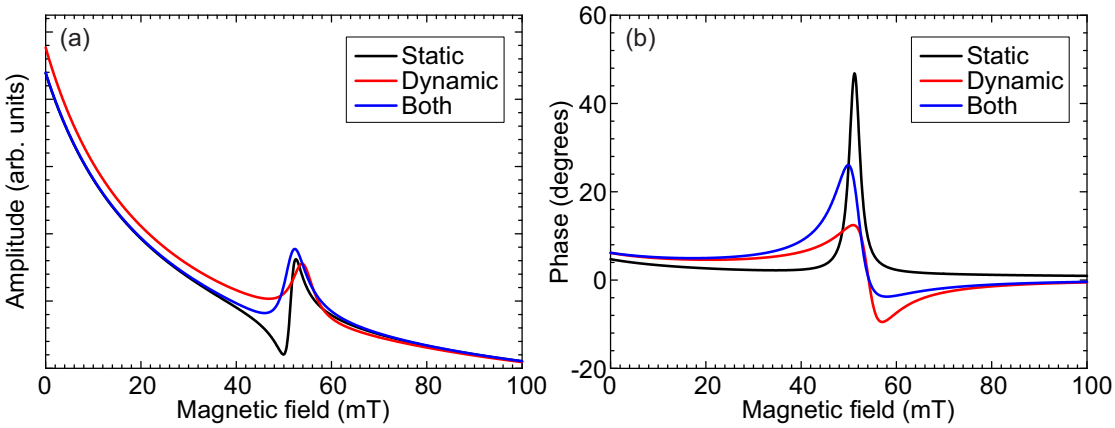


Figure 5.10: Effects of combining the static and dynamic coupling on the amplitude (a) and phase (b) of induced precession at 7 GHz for a 5 nm $Co_{50}Fe_{50}$ layer coupled to a 5 nm $Ni_{81}Fe_{19}$ layer.

Being based on the LLG formalism, modelling with the dynamic susceptibility approach is somewhat limited in that it does not include non-Gilbert damping mechanisms, such as inhomogeneous broadening or two-magnon scattering. Further, it is ill-suited to modelling particularly thick layers (>40 nm), where there is significant variation in magnetodynamics across the layers. Despite this, the ability to detect the presence and interplay of spin pumping and static exchange is extremely valuable, and leads to important insights into spin transfer in the following three chapters. As it incorporates interactions through the effective field in the LLG, it can also be readily adapted to model the particulars of a range of material systems, including, for example, exchange bias or strain effects.

5.4 Conclusion

This chapter has presented two of the modelling approaches used through the thesis research: micromagnetic simulations in OOMMF, and numerical determination of the dynamic susceptibility over resonance based upon a linearised solution of the LLG. Both methods allow study of the spatially resolved magnetodynamics

of thin film magnetic heterostructures, without requiring a synchrotron or similar complex experimental techniques. Further, through their implementations of static coupling mechanisms, they enable identification of the character of resonances in coupled systems. While OOMMF offers finer spatial discretisation, and thereby examination of the distribution of energy across the magnetic layer at the resonance condition, it currently lacks the ability to simulate spin pumping offered by calculations of the dynamic susceptibility. This modelling of magnetodynamics, and the introduction of coupling terms to the resonance condition, will prove crucial in the coming three chapters, which deal with trilayer structures. The separation of the effects of intrinsic damping, spin pumping, and static exchange is essential to develop a detailed understanding of coupled magnetodynamics.

Chapter 6

Suppression of Spin Pumping by an Insulating Barrier

6.1 Motivation

Much attention is currently devoted to the spin-transfer torque (STT), through which it is possible to realise spontaneous magnetisation precession and switching. The spin pumping effect is one of the most promising candidates for this application [106]. Spin pumping has been under intense scrutiny since it was first proposed in 2002 [20, 21, 51], studying the generation of pure spin currents by ferromagnetic resonance. Particular attention has been paid to the transmission of spins across a variety of non-magnetic (NM) materials, from conductors such as Ag [23], Au [107], and Cu [15, 43] to semiconductors such as Si [25], or insulators like MgO [33] and $SrTiO_3$ [25]. The efficacy of spin pumping is governed by the spin diffusion length of the nonmagnetic layer, and the spin mixing conductance of the FM/NM interface [22]. Since the spin transfer processes involve conduction electrons, spin pumping is heavily suppressed in insulators, leading to very short spin coherence lengths, often under a nanometre [25]. However, a coupling of the

spin and charge degrees of freedom, and associated charge pumping in tunnelling heterostructures can complicate interpretation of results [106, 108, 109]. For this reason, it is useful to investigate spin pumping through insulating layers using probes that are insensitive to charge-based effects. Such information is valuable both from the perspective of fundamental physics, aiming to understand spin transfer processes, and for comparison against more exotic systems, such as the topological insulators that are the subject of chapter 7.

This chapter presents a study of exchange coupling across a thin MgO barrier in a magnetic tunnel junction trilayer sample, investigating the interplay of static and dynamic interactions on the coupled magnetodynamics. The strength of the static exchange interaction can be reduced by increasing the thickness of the MgO barrier, as the layers are decoupled by their increasing separation, and is most easily observed by examining magnetic hysteresis loops. Spin pumping can be detected in several ways, for example by measuring the voltage induced by the inverse spin-Hall effect [33], examining resonant linewidth as a function of barrier thickness [23], or layer-resolved measurements of precession induced by the absorption of the pumped spin current [15]. Here, the latter two methods are employed as complimentary tools to quantify the dynamic interaction, without requiring charge transport studies on patterned samples.

6.2 Sample Fabrication

Magnetic multilayer samples were prepared by MBE in the LaMBE system (see section 3.1) on epi-ready MgO (001) substrates. RHEED measurements were performed throughout the growth to monitor crystal quality. The full structure is $MgO/Co_{50}Fe_{50}(10)/MgO(t_{MgO})/Ni(4)/Ag(2)$ (thicknesses in nm), with $t_{MgO} = 1$, 2, 3, 4 nm. The substrates were first annealed at 700°C to improve surface unifor-

mity, before being cooled to 500°C for the deposition of stoichiometric $Co_{50}Fe_{50}$. The samples were further cooled to room temperature for deposition of MgO onto the epitaxial $Co_{50}Fe_{50}$(hereafter referred to as CoFe, for brevity). To improve the quality of the MgO, the samples were then annealed at 300°C for 20 minutes, leading to sharpening of the streaks, indicative of good crystalline quality, before being again cooled to room temperature for the deposition of Ni and the Ag cap.

6.3 Static Exchange Coupling

Figure 6.1 shows hysteresis loops measured by SQUID-VSM for all four trilayer samples. The reduction in static interlayer coupling as a function of increasing t_{MgO} can be clearly observed. In the case of the thinnest MgO barrier [$t_{\mathrm{MgO}} = 1$ nm, Fig. 6.1(a)] the two layers are strongly bound, and there is a single switching step, with a coercive field of 2 mT. As the thickness of the barrier increases, the layers decouple and behave more independently. For $t_{\mathrm{MgO}} = 2$ and 3 nm [Figs. 6.1(b) and 6.1(c)], the coupling between the two layers appears to cause some winding, leading to a smeared out transition as opposed to sharp steps. However, it is possible to identify two distinct steps in the hysteresis loop, which can be more clearly understood through the use of element-specific XMCD-hysteresis (Fig. 6.2). With the thickest barrier, $t_{\mathrm{MgO}} = 4$ nm [Fig. 6.1(d)], the coupling between the two layers is suppressed, and there are two sharp, distinct switching steps. This appears to indicate an oscillatory coupling strength, akin to an RKKY interaction, which is rather surprising in the context of an insulating barrier. For the 4 nm barrier the two ferromagnets behave as if they are independent, isolated layers, and the hysteresis loops could be represented as a simple linear combination of the two.

The element-specific (and thus layer-specific) tool of XMCD-hysteresis was used

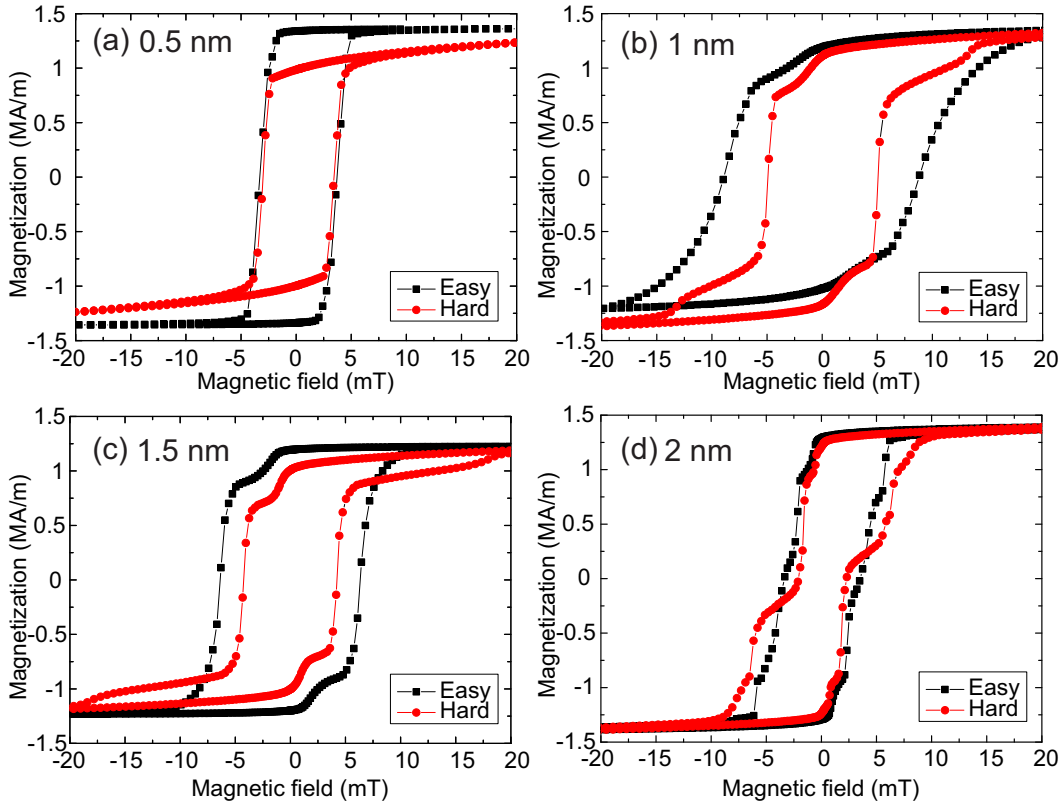


Figure 6.1: SQUID-VSM measurements of hysteresis loops for trilayers with t_{MgO} = 1 (a), 2 (b), 3 nm (c), and 4 nm (d). As the thickness of the MgO layer increases the interlayer exchange weakens, moving from simultaneous magnetic reversal to well-resolved steps as the two layers move independently.

to study magnetic reversal process in more detail, results for samples with t_{MgO} = 1 and 2 nm are shown in Fig. 6.2. The results confirm that for a thin MgO barrier the two layers are strongly coupled and switch together. This could be due to surface roughness of the MgO layer giving rise to a Néel or orange-peel type coupling [32]. Alternatively, it is possible that the layer is not continuous, with pinholes or other defects causing the two FM layers to be in contact, and interact through a direct exchange mechanism, which is possible for such thin barriers, and rather undesirable in the case of transport-based devices [110].

VNA-FMR measurements were performed to determine values for the interlayer exchange coupling and magnetocrystalline anisotropy parameters for all samples. Figure 6.3(a) shows an example field-frequency transmission map, measured for

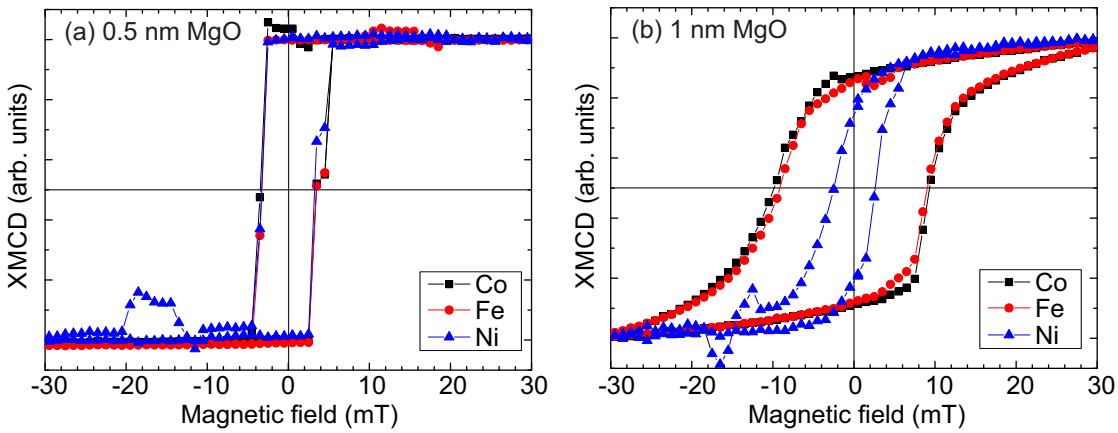


Figure 6.2: XMCD-hysteresis measurements of magnetisation reversal for trilayers with $t_{\mathrm{MgO}} = 1$ (a) and 2 nm (b) with the magnetic field applied along the easy axis of the CoFe. Discontinuities in the Ni data likely arise from beam instabilities or issues with the electromagnet.

the sample with $t_{\mathrm{MgO}} = 1$ nm. Despite the static coupling causing the two layers to switch together in measurements of hysteresis loops, there are still two distinct resonance modes, indicating that the magnetodynamics of the heterostructure are not as strongly bound.

Fits to resonance fields were performed as a function of excitation frequency and magnetisation alignment using the Kittel equation (2.15), including the field due to static exchange coupling, equation (2.20). Table 6.1 shows the resulting values for the cubic and uniaxial magnetocrystalline anisotropy parameters, $Kc_{\|}$ and $Ku_{\|}$, for each layer, and the interlayer exchange constant, A_{ex}. For the most part there is no relation between anisotropy parameters and barrier thickness, although there is a systematic decrease of in-plane uniaxial anisotropy in the CoFe layer, for unknown reasons. However, the variation of in-plane cubic anisotropy in the CoFe indicates that there is some variation in sample quality across the series.

The strength of the interlayer exchange coupling is plotted as a function of MgO thickness in Fig. 6.3(b), showing a decrease of interaction strength as the separation of the two FM layers increases. The complete suppression of the interaction at $t_{\mathrm{MgO}} = 1$ nm is somewhat surprising, as it suggests an oscillatory coupling

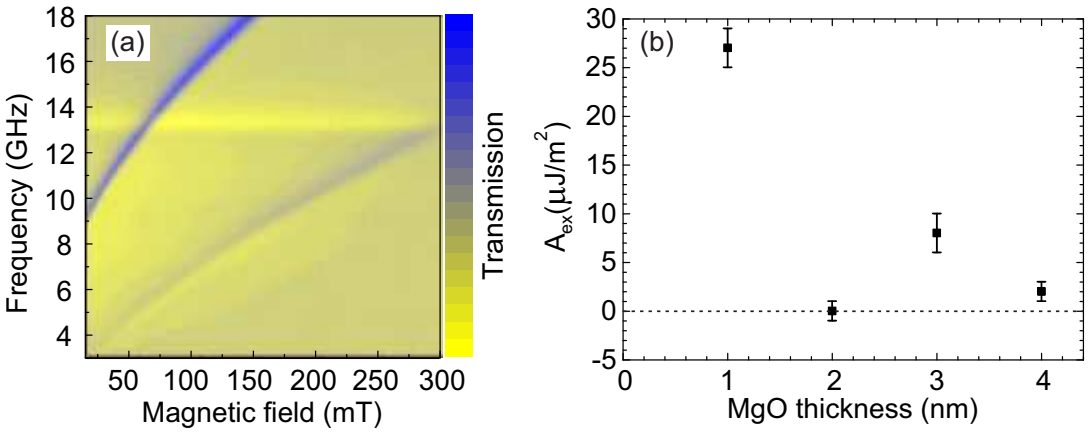


Figure 6.3: (a) VNA-FMR field-frequency transmission map for the sample with $t_{\mathrm{MgO}} = 1$ nm, and the magnetic field applied along the easy axis. (b) Interlayer exchange coupling, A_{ex}, as a function of MgO barrier thickness, determined from fits to Kittel curves. Error bars are uncertainty on fitting parameters.

strength, a phenomenon more usually associated with coupling across conductive layers (see e.g. Ref. [30] or chapter 8). This finding is in contrast to previous work on MgO, for example Ref. [48], where a similar study found no evidence of such variation. If the coupling has a component associated with surface roughness then variation within the sample series is possible, as different samples could have different layer qualities, although every effort was made to ensure reproducibility of growth. The trend in strength of the coupling suggests that the layers should be completely decoupled for $t_{\mathrm{MgO}} = 5$ nm, as the thick insulating barrier blocks all static interactions.

6.4 Structural Characterisation of the MgO Barriers

As can be seen from the discussion above, the continuity and quality of the MgO barrier layer is of key importance when interpreting the results. As the effects of pinholes, surface roughness and other defects can significantly affect the magnetic

Layer	t_{MgO} nm	$Kc_{\parallel}$ kJ/m^3	$Ku_{\parallel}$ kJ/m^3	A_{ex} μJ/m^2
$Co_{50}Fe_{50}$	1	48.4 ± 0.3	4.0 ± 0.3	27 ± 2
	2	41.6 ± 0.2	3.2 ± 0.2	0 ± 1
	3	47.5 ± 0.3	1.9 ± 0.3	8 ± 2
	4	43.4 ± 0.2	0.8 ± 0.3	2 ± 1
Ni	1	0.3 ± 0.1	1.4 ± 0.3	27 ± 2
	2	0.04 ± 0.09	1 ± 2	0 ± 1
	3	0.6 ± 0.2	1.9 ± 0.3	8 ± 2
	4	0.1 ± 0.1	1.6 ± 0.3	2 ± 1

Table 6.1: Magnetocrystalline anisotropy parameters and exchange coupling for the CoFe and Ni layers of the heterostructures, determined by fitting the angle- and frequency-dependent FMR field for heterostructures with indicated MgO thicknesses. A_{ex} is a common parameter shared by both layers.

properties of the system, it is important to properly characterise the barrier. To this end, transmission electron microscope (TEM) measurements were performed by Dr. Vlado Lazarov and Daniel Pingstone, at the University of York.

Structural properties of the grown MTJs were studied using a JEOL 2200FS double aberration corrected (scanning) transmission electron microscope (S)TEM. Cross-sectional TEM specimens were prepared using conventional methods that include mechanical thinning and polishing followed by Ar ion milling in order to achieve electron transparency [111]. Figure 6.4(b-d) shows cross-sectional TEM images of the MTJs. These images demonstrate epitaxial growth of the films, and confirm that the MgO barrier is continuous down to the thinnest barrier thickness of 1 nm. It is therefore possible to rule out the presence of direct coupling between the two layers. The smooth interfaces indicate that the Neél coupling should be minimal also, meaning that the static interaction must be mediated by a tunnelling-like interaction through the insulating barrier. This is a rather surprising finding, as an oscillatory coupling has not previously been observed in such systems, and an insulating barrier does not permit an RKKY-type interaction. It is possible that a mechanism such as superexchange couples the two ferromagnetic layers, mediated by the oxygen in the MgO, but further study is required to make

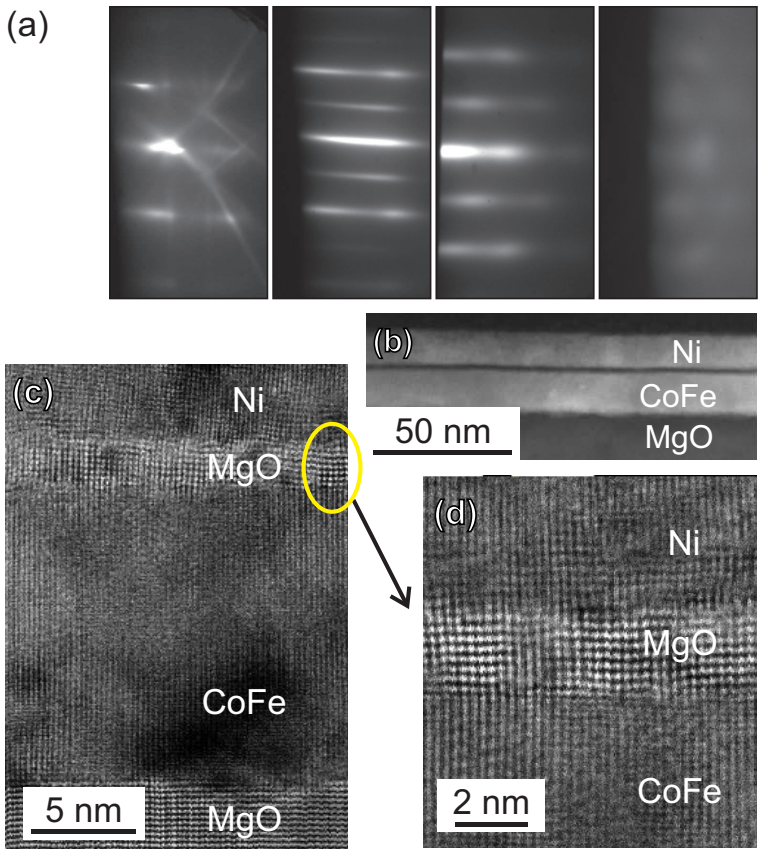


Figure 6.4: (a) RHEED images of the MgO substrate (at 700°C), CoFe layer, 3-nm-thick MgO barrier (after annealing at 300°C), and finally Ag-capped Ni layer (from left to right). (b-d) Cross-sectional TEM view of the MTJ with a 2-nm-thick MgO barrier. (b) Low-magnification high angle annular dark field image of the MTJ showing uniform thickness of electrodes and MgO tunnel barrier. (c) High-resolution bright-field scanning TEM showing the atomic structure of the substrate, electrodes and barrier viewed along [010]. (d) Interface region of electrode(s)/MgO barrier showing the atomically abrupt interfaces and the well-structured MgO barrier textured along the [010] direction.

a more concrete statement.

6.5 VNA-FMR Measurements of Gilbert Damping

The presence of spin pumping can be inferred by plotting the thickness dependence of the Gilbert damping parameter of both layers of the trilayer, as the spin

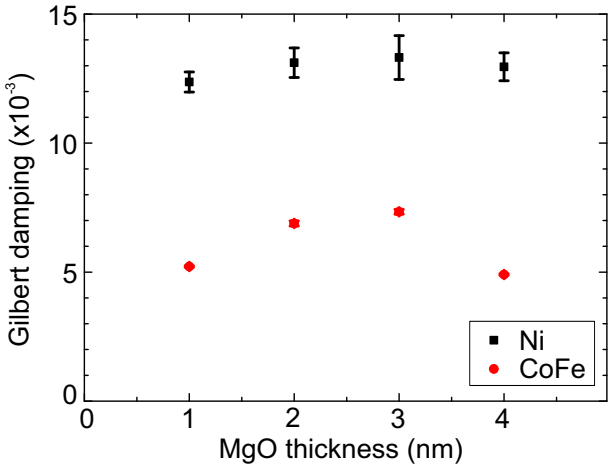


Figure 6.5: Gilbert damping determined from VNA-FMR measurements as a function of t_{MgO}. Error bars arise from uncertainty on linear fits to linewidth as a function of frequency, and in the case of the CoFe data are comparable to point size.

pumping component of damping depends upon the ability of pumped spins to reach the efficient spin sink of the second FM layer. However, in the case of an insulating barrier the spin diffusion length should be practically zero, due to the extremely short scattering lifetimes. Investigations using inverse spin Hall effect measurements have supported this suggestion, for example across $SrTiO_3$ [25] or MgO [33]. However other studies have proposed the possibility of enhancement of the induced voltage through the presence of an insulating barrier [106], as absorption of the spin current leads to sizeable charge pumping.

Gilbert damping was determined by plotting the linewidth of resonance as a function of excitation frequency, and applying equation (2.11), results for both FM layers are plotted as a function of MgO barrier thickness in Fig. 6.5. Within the error bars, there is no change in the Gilbert damping of the Ni layer, which supports the assertion that an insulating layer such as MgO does not permit a spin current to flow. However, the data for the CoFe layer is more complicated, showing at first a slight increase, then a drop in damping. The jump from t_{MgO} = 1 nm to t_{MgO} = 2 nm could be accounted for by the difficulty of achieving a continuous film at such low thicknesses. Initially, the MgO could be too thin to

form a continuous layer, resulting in pinholes or islands that cause direct contact. In this case, the magnetodynamics of the layers are more complicated, as hybridisation of the interface region can lead to modification of the relaxation rate. With a continuous layer, separate behaviour of the layers is restored. However, TEM measurements (Fig. 6.4) showed that the barrier is smooth and continuous even for $t_{\mathrm{MgO}} = 1$ nm, so any such interaction must occur across the insulating layer, rather than bypassing it due to imperfections.

In the case of the lower damping for the thickest layer, it is challenging to provide a conclusive explanation. A drop in damping with increasing interlayer thickness is usually indicative of spin pumping, but it is unclear why the damping increases before this point. It is unlikely to be related to a structural change in the CoFe, as this is the bottom layer of the heterostructure. RHEED measurements during growth, and TEM performed afterwards, gave no indication of a variation in crystal quality that could explain this change either, and despite some variation in magnetic parameters across the series there is nothing to explain the change in damping.

Several points should be noted when considering these results. Firstly, measurements on comparable bare CoFe layers yielded a Gilbert damping of $\sim 3\times10^{-3}$. This suggests that whether or not it is able to transmit a spin current, the MgO does at least absorb some of the spins pumped by the precessing magnetisation of the CoFe. Secondly, the increase of damping up to $t_{\mathrm{MgO}} = 3$ nm is not large, especially when compared to the spin pumping damping in Cr spin valves (chapter 8) or the changes induced by doping with rare earths (chapter 4).

Unfortunately, these indirect measurements of spin transfer using VNA-FMR are unable to provide a conclusive determination of the presence of spin pumping within the heterostructures. Therefore, XFMR was performed to investigate the system further, using the layer-resolved technique to establish a clearer picture of

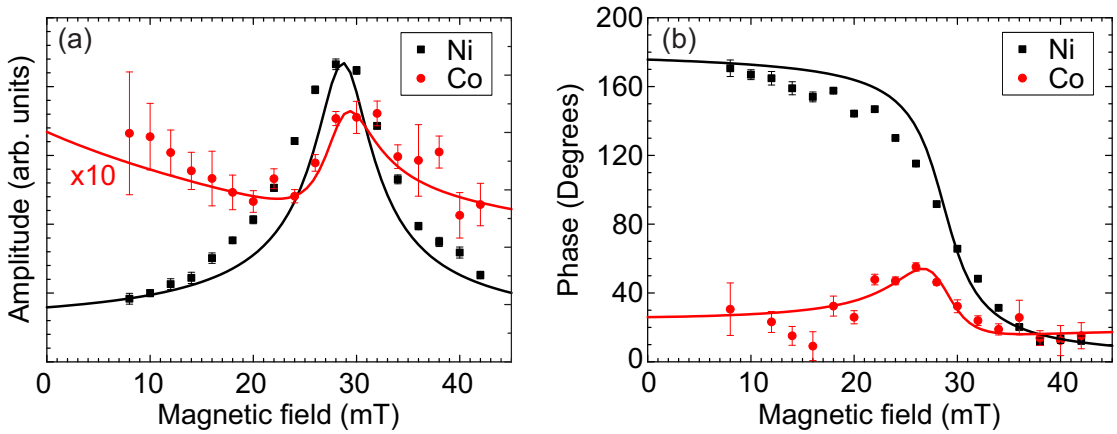


Figure 6.6: Layer-resolved magnetisation dynamics at 4 GHz for the sample with $t_{\mathrm{MgO}} = 1$ nm, showing amplitude (a) and phase (b) of precession of magnetism for Ni (black) and Co (red). The magnetic field is applied along the easy axis of the CoFe. The amplitude of induced precession in Co is approximately ten times less than that of the Ni, the data has been scaled accordingly. Solid lines are fits to the data using the dynamic susceptibility modelling introduced in section 5.3.

the coupling mechanisms that exist across the MgO barrier, aiming to unambiguously ascertain whether a pure spin current is able to cross the barrier.

6.6 Layer Resolved Magnetodynamics

X-ray detected ferromagnetic resonance measurements were performed to study the layer-resolved magnetodynamics of two samples with an MgO spacer layer, paying particular attention to the distinctive off-resonance precession induced by interlayer exchange coupling and spin pumping. By tuning the energy of the incident x-rays to the absorption edge of either Co or Ni, the element specific absorption reveals information about the magnetic state of a particular layer. This removes some of the uncertainty about variations within the sample series when determining the presence of the dynamic interaction, as rather than inferring the spin pumping component of damping, the technique directly detects the effects of the torque exerted by the pumped spins.

Figure 6.6 shows the amplitude and phase of precession at 4 GHz for each layer in the sample with $t_{\mathrm{MgO}} = 1$ nm, with the magnetic field applied along the easy axis of the CoFe. The resonance in the Ni layer can be clearly seen, with a peak in amplitude at 28 mT. Precession is also induced in the off-resonance CoFe layer; the resulting dynamic XMCD signal is approximately ten times smaller than that of the Ni. The phase feature in the Co has a magnitude of about 40°, and is predominantly unipolar in character. Taken together with the bipolar shape of the Co amplitude variation, this indicates that the static interaction is primarily responsible for induced precession in the Co, as would be expected following the VNA-FMR measurements.

Solid lines in Fig. 6.6 are fits to the data using the dynamic susceptibility modelling outlined in section 5.3 and appendix A. The values of static exchange coupling and magnetocrystalline anisotropy determined in section 6.3 were used to calculate the expected amplitude and phase of precession for each layer. In order to reproduce the slightly distorted features in the Co, a dynamic interaction had to be introduced, accounting for 50% of the total Gilbert damping in the Ni layer, and assuming perfect transmission of spins. This modifies the shape of the Co features, mixing a small amount of unipolar feature into the bipolar lineshape of the amplitude, and vice-versa in the phase. With this included the model reproduces the experimental data, although it underestimates the linewidth of the Ni mode. This is because it does not include inhomogeneous (non-Gilbert) broadening, which can be a major contribution to the linewidth at low frequencies. The measurement of a small component of dynamic interaction shows that a suitably thin MgO barrier will permit a spin current to flow.

Figure 6.7 shows the amplitude and phase of precession at 4 GHz for each layer in the sample with $t_{\mathrm{MgO}} = 2$ nm, with the magnetic field applied along the easy axis of the CoFe. As with the $t_{\mathrm{MgO}} = 1$ nm case outlined above there is a well-

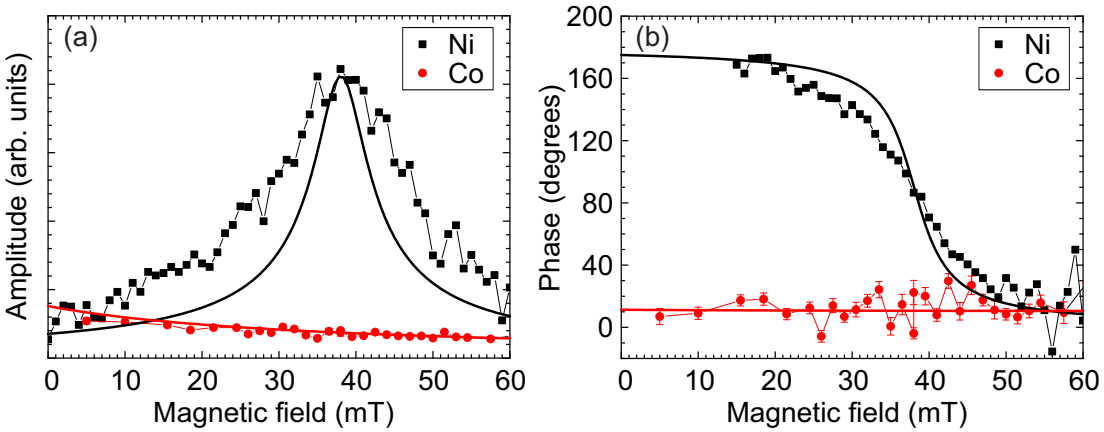


Figure 6.7: Layer-resolved magnetisation dynamics at 4 GHz for the sample with $t_{\mathrm{MgO}} = 2$ nm, showing amplitude (a) and phase (b) of precession of magnetism for Ni (black) and Co (red). The magnetic field is applied along the easy axis of the CoFe. Solid lines are fits to the data using the dynamic susceptibility modelling introduced in section 5.3.

defined resonance in the Ni data, although with $A_{\mathrm{ex}} = 0 \pm 1$ μJ/m^2 the resonance field is increased to 35 mT. A more striking effect of this reduction in exchange coupling, however, is the complete absence of induced precession in the CoFe layer. The flat line in both amplitude and phase confirms the previous finding that a 2 nm MgO barrier completely suppresses the static interaction, nor does it permit a spin current to flow, in agreement with previous studies of spin pumping in insulators [25, 33]. Solid line fits from a model without spin pumping or static exchange coupling are shown in Fig. 6.7, showing that there is no interaction. The slight curvature of the Co amplitude data is due to the presence of the CoFe layer resonance at negative field, the slope is the tail of the Lorentzian. As before, the lack of inhomogeneous broadening causes the model to underestimate the linewidth of resonance.

The XFMR results provide further information regarding the open question left by indirect measurements of spin pumping in section 6.5. The increase in damping from the thinnest layer to the 2 nm case appears to arise from the move to complete attenuation of the pumped spin current within the MgO, and a significant

reduction in the static interaction between the two layers. With the insulating barrier blocking the transmission of spins, there is no dynamic interaction. This is in line with previous studies of similar samples [25, 33]; but here the separation of different coupling effects permitted by XFMR provides a deeper understanding of the magnetodynamics of such systems.

6.7 Conclusion

This chapter has presented the first in a series of studies of coupled magnetisation dynamics in trilayer structures, investigating the interplay of static and dynamic coupling mechanisms. Here, an insulating MgO barrier was used to suppress both interactions, in a sample structure based on the magnetic tunnel junction architecture. Layer-resolved measurements of magnetodynamics show that for a thin spacer layer both static exchange and spin pumping are present, leading to coupled precession of the two magnetic layers, and simultaneous switching at a low coercive field of 2 mT. As the barrier thickness increases the interaction between the magnetic layers is weakened. In particular, the pure spin current driven by ferromagnetic resonance is attenuated by as little as 1 nm of MgO, as the low scattering lifetimes and lack of conduction electrons leads to an extremely short spin diffusion length [25, 33]. This was indicated by the lack of systematic variation of Gilbert damping as a function of t_{MgO}, and confirmed by XFMR measurements. Analysis of the Kittel curves of resonance shows that static exchange is also suppressed at 2 nm, but this appears to be a result of an oscillatory coupling strength, rather than complete decoupling of the two layers, as a weak interaction is also observed up to 4 nm. Aside from the $t_{\mathrm{MgO}} = 2$ nm case, A_{ex} generally decreases as a function of t_{MgO}, suggesting that 5 nm of MgO would completely separate the two magnetic layers. The mechanism behind this coupling is currently unknown,

however, as the RKKY interaction that typically drives an oscillatory strength should not exist in an insulating layer such as MgO. Moreover, the effect cannot be explained away as arising from structural changes or imperfections in the MgO barrier, as TEM shows that this layer is smooth and continuous across the whole series. It is clear that this surprising result merits further investigation, seeking to understand the origin of the varying interaction strength.

These results demonstrate how the coupling between magnetic layers can be manipulated through choice of barrier material and thickness, and illustrate the differing regimes of static and dynamic coupling that can be thus attained. The ability of MgO to quickly suppress a spin current was confirmed, and in more general terms it was shown that a trivial insulator can very effectively decouple ferromagnetic layers. Furthermore, the co-operative effects of static and dynamic were studied, showing how they can co-operatively transfer energy between layers during ferromagnetic resonance. The following chapters build on these themes, aiming in particular to study spin pumping in more detail and develop a deeper understanding of static and dynamic coupling.

Chapter 7

Spin Pumping in Topological Insulators

7.1 Motivation

The exciting physics of topological insulators (TIs) has been under intense study since their theoretical prediction [114] and experimental verification [115–117]. Recently, they were shown to display the quantum anomalous Hall effect after doping with magnetic impurities [118], and are proposed to host image magnetic monopoles and the giant magneto-optical effect [119–122]. In the prototypical three-dimensional TI Bi_2Se_3 a large spin-orbit interaction leads to a band inversion in the bulk and the formation of topologically protected surface states (TSS), with fully spin-polarised counter-propagating conduction channels that are robust against scattering from non-magnetic impurities [123]. Spin-momentum locking suggests the possibility of very long spin-flip scattering lifetimes and the ability to generate ultra-high spin-orbit torques [124–126]. It has been predicted that the TSS can exert a torque on spins in a neighbouring ferromagnet (FM) through exchange coupling [127]. However, in order to realise these prospects the magneto-

dynamics of the TSS must be studied and such TI-FM heterostructures fabricated. While angle-resolved photo-emission spectroscopy (ARPES) has been extremely successful at identifying TIs [116, 117], transport measurements are hampered by to large bulk conductivities that make unambiguously identifying the surface state challenging [128,129]. It is therefore beneficial to apply a wider range of techniques to the study of TIs, aiming to focus more closely on the spin degrees of freedom present in the TSS.

FMR offers an attractive means to investigate the coupling of ferromagnets to TIs, using the pure spin current emitted at the resonance condition to probe the bulk and surface state. In VNA-FMR the enhanced damping due to this loss of angular momentum can be studied, while XFMR allows detection of coupling across a TI spacer layer in a spin-valve-like structure. The application of this technique to TIs is quite naturally suggested by the similarity between the spin-locked surface state of a TI and the separation of angular momentum and charge flow that takes place in a pure spin current. Recently, studies of such effects have begun to emerge through electrical transport and inverse spin-Hall effect measurements [126, 130, 131], demonstrating the great potential of TIs for incorporation into spintronic devices such as spin valves.

This chapter describes a series of experiments designed to assess the spintronic potential of TIs, using $Co_{50}Fe_{50}$(30 nm)/Bi_2Se_3(x nm)/$Ni_{81}Fe_{19}$(30 nm) heterostructures with $x = 4...20$ nm (materials are also referred to as CoFe, BiSe, and NiFe, for brevity). Studies of the thickness dependence of interactions between the two FM layers were used to separate the contributions of bulk and surface conduction through the TI. Measurements of anti-damping terms that arise for overlapping resonances were performed to isolate the presence of spin pumping in the heterostructures, as opposed to other coupling mechanisms. Finally, the temperature dependence of the Gilbert damping was measured, as transport measurements

have shown that conduction through the bulk of a TI can be frozen out at low temperatures.

7.1.1 What is a Topological Insulator?

Topological insulators are materials in which a bulk band inversion leads to the formation of a surface state protected by time reversal symmetry, wherein electrons are spin-locked and back-scattering events are forbidden. It is important to note that this novel state is not a surface property, rather its existence is a direct consequence of the bulk band structure. Only a brief overview of TIs and their study is presented here, the interested reader is referred to, for example, Refs. [36, 79].

The band inversion that drives the fundamental properties of TIs has its origin in the strong spin-orbit interaction of such materials. Considering a simple picture, imagine a material with a separated conduction (CB) and valence (VB) band, in the case of a direct band gap at the centre of the Brillouin zone. In a conventional material the CB has positive parity, while the VB has negative character. The spin-orbit interaction lifts the degeneracy of the p level of the VB, giving rise to $j = 3/2, j = 1/2$ states. With sufficiently strong splitting, the $j = 3/2$ state moves above the s state of the CB, leading to a parity inversion and the creation of a TI. An image of the bandstructure of a TI is shown in Fig. 7.1(a). The "normal" ordering of bands must be restored at the junction of a TI with a conventional material. This means that the bands must cross the Fermi energy at the interface, leading to the formation of two metallic states that are topologically protected. In the surface state the direction of an electron's travel is determined by its spin, and they travel without resistance as any scattering event would require reversal of the spin. This is not possible without the presence of spin scattering defects, such as magnetic impurities. A diagram of these protected states is shown in Fig. 7.1(b).

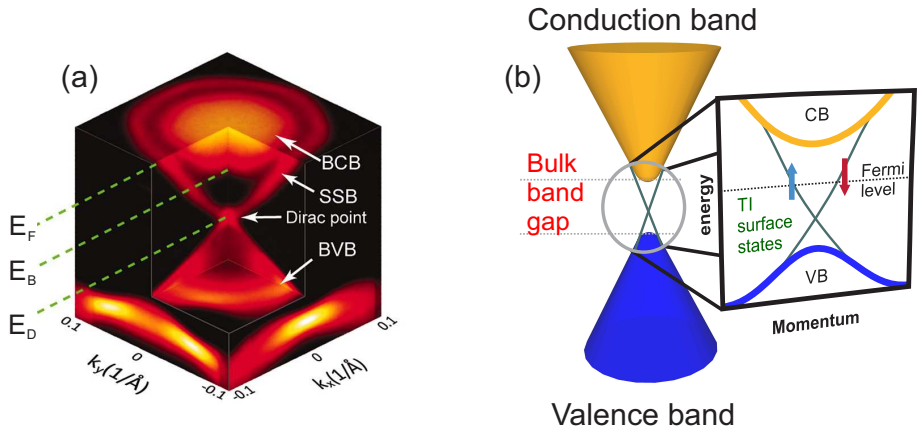


Figure 7.1: (a) Measurement of the bandstructure of the topological insulator Bi_2Te_3, showing the bulk conduction band (BCB), the surface state band (SSB) and bulk valence band (BVB). The crossing of bands occurs at the Dirac point. Figure taken from Ref. [117]. (b) Schematic of the band structure of the TI, showing the spin-polarised surface states that form the Dirac cone between the conduction and valence bands. Figure taken from Ref. [60].

A rather neat analogy for this is the case of road-traffic. In some countries cars drive on the left, in others on the right. This is a "bulk" property of the country, and is enforced across its surface. Complications arise, however, at the interface of two countries where cars drive on different sides, as traffic must be inverted without breaking its flow. One proposed solution is a bridge the separates the two lanes of traffic, passes one under the other, and merges them again, with their sense reversed [36]. This inverts the traffic without necessitating it to slow or stop: the bulk properties of the two countries has been preserved by a crossing at the interface.

The prototypical 3D TIs that host a 2D surface state are the chalcogenide systems Bi_2Se_3 and Bi_2Te_3. These have the $R\bar{3}m$ crystal structure, with a quintuple layer sequence (Se-Bi-Se-Bi-Se) and van der Waals bonding between the Se layers. They are typically grown on c-plane sapphire, to achieve high crystal quality [132], but can form high quality structures on a wide variety of materials due to the adaptive nature of van der Waals bonding [133]. One should note, however, that despite their name, most topological insulators are in fact very poor insulators, and are

rather closer to narrow bandgap semiconductors, with a typical gap on the order of 300 meV.

7.2 Sample Fabrication

Samples were prepared using MBE, sources were calibrated using a quartz crystal microbalance and beam-flux monitor. First, the MgO substrate was annealed at 700°C to clean the surface and reduce the surface roughness. Next, 30 nm of $Co_{50}Fe_{50}$ was co-evaporated from Fe and Co electron-beam evaporators. The substrate temperature was held at 300°C during this stage. Strong streaks and kikuchi lines were observed by RHEED, indicative of high crystalline quality. Samples were then transferred into a chalcogenide MBE for growth of the Bi_2Se_3 layers. Growth of the TI layers was performed by Liam Collins-McIntyre, according to growth protocols developed during his study of thin film topological insulators, see e.g. Refs. [79, 132, 133]. The $Co_{50}Fe_{50}$ surface was again annealed at 300°C to ensure the surface was high quality; this was checked by RHEED before growth. The Bi and Se were then evaporated from Knudsen cells for stoichiometric growth of Bi_2Se_3. Substrate temperature was 200°C. RHEED patterns reveal the formation of a crystalline mosaic domain pattern. Bi_2Se_3 thickness was varied between 4 - 20 nm. The samples were then transferred back to the LaMBE chamber, and a top FM layer of $Ni_{81}Fe_{19}$ (30 nm) deposited at room temperature ($\sim$300 K), to avoid damaging the Bi_2Se_3 layer structure. This leads to polycrystalline $Ni_{81}Fe_{19}$, which is desirable as it ensures fully isotropic magnetic behaviour. Samples were then capped with 5 nm Cu, to prevent oxidation. Samples were grown with an interlayer thickness of $t_{\mathrm{TI}} = 4$, 6, 8, 16, 20 nm.

The static magnetic properties of the films were characterised using VNA-FMR; example field-frequency transmission maps along the easy and hard axes are shown

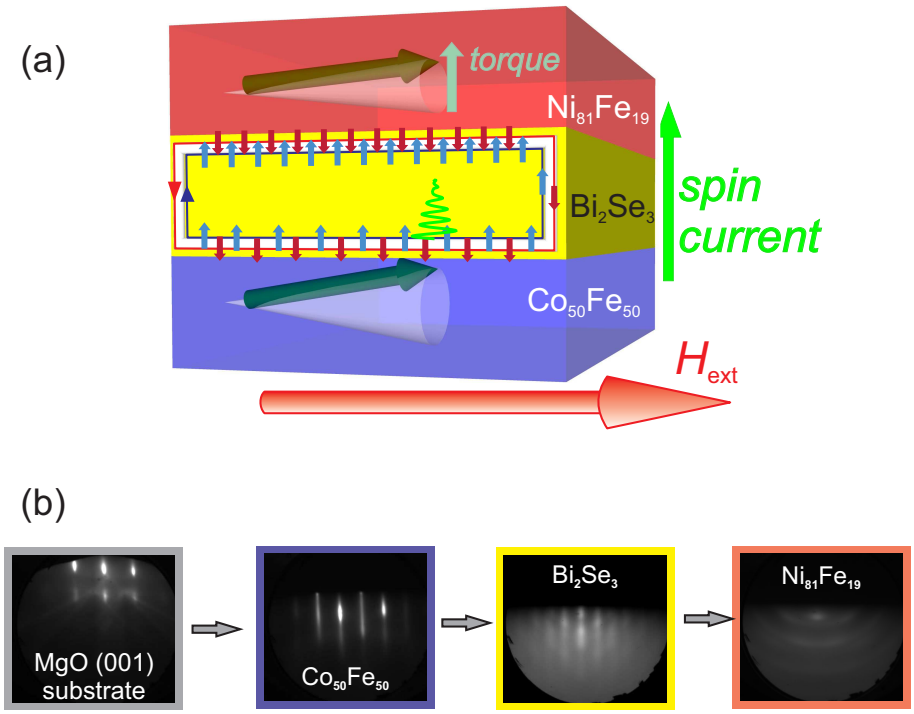


Figure 7.2: (a) Schematic of the device structure, showing the TI Bi_2Se_3 placed between two FM layers. The surface state is indicated by up- and down-arrows, representing counter-propagating spin-momentum locked conduction. The precession of magnetisation excited around the static bias field drives a pure spin current from the $Co_{50}Fe_{50}$ through the Bi_2Se_3 into the $Ni_{81}Fe_{19}$, exerting a spin transfer torque. (b) RHEED images of the growth of each layer. Figure from Ref. [60]
.

in Figs. 7.3(a) and 7.3(b). Strong resonances are observed from both layers, with the CoFe displaying the desired strong four-fold cubic anisotropy, and the NiFe having a much weaker two-fold uniaxial anisotropy. Fits to the angle- and frequency-dependence of resonance were performed to determine the magnetocrystalline anisotropy parameters and the Landé g-factor. No evidence of static exchange coupling was observed. An example of the angular variation of resonant field at 15 GHz is plotted in Fig. 7.3(c), materials parameters determined in this way are given in table 7.1. The slight dip in anisotropy constants observed for the 6 nm TI barrier likely arises from slight variations in the growth stage, as this sample was produced in a separate growth run to the others.

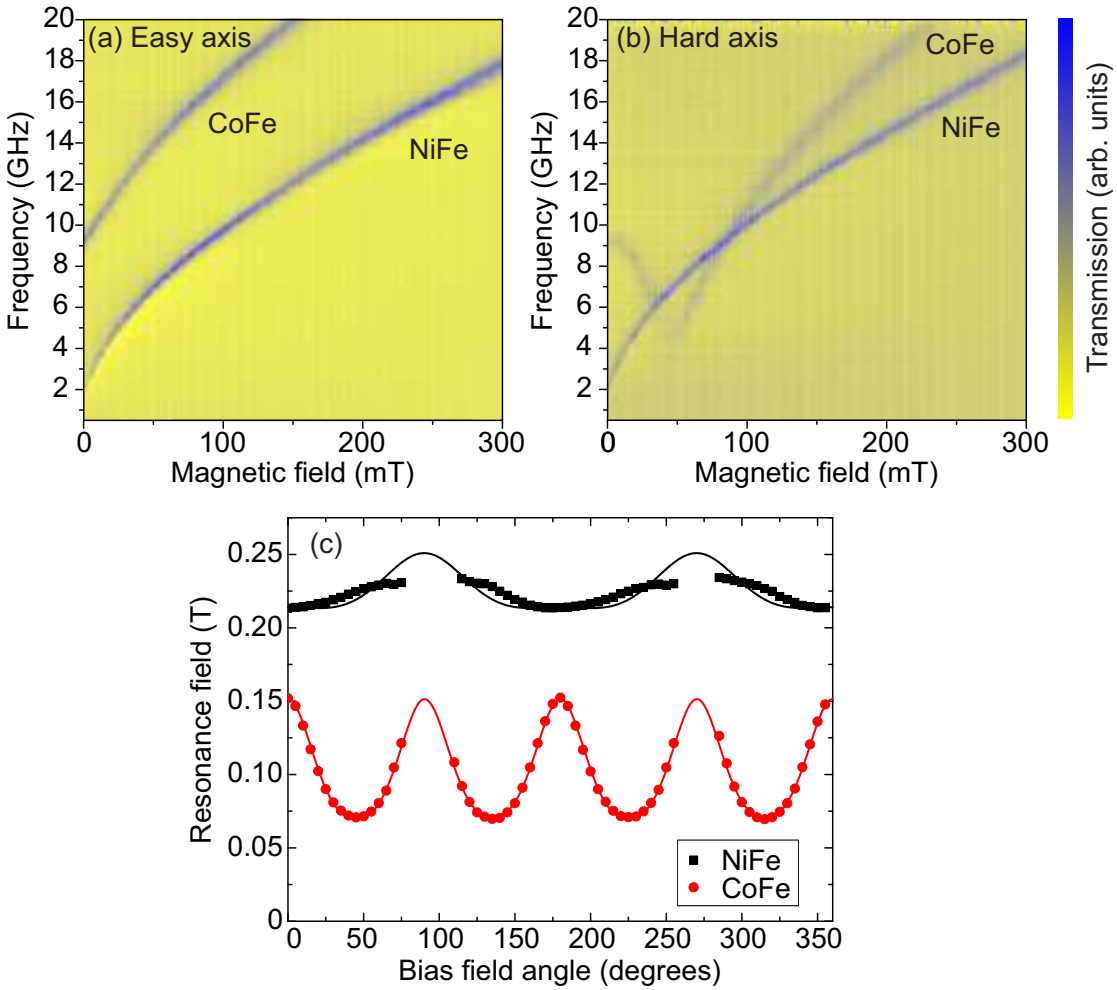


Figure 7.3: Field-frequency transmission maps for bias field applied along the easy (a) and hard (b) axes of the CoFe layer of a sample with $t_{\mathrm{TI}} = 8$ nm. Two strong resonance modes are observed, which can be attributed to the CoFe and NiFe layers by examining their angular dependence: the anisotropic mode comes from the crystalline $Co_{50}Fe_{50}$. This is shown in more detail in (c), plotting resonant field at a constant microwave frequency of 15 GHz, along with solid line fits to the data. The bias field is along the hard axis at zero degrees. Missing data points correspond to regions where the relative alignment of microwave and bias fields leads to limited precession and correspondingly weak signal.

Layer	t_{TI}	$Kc_{\parallel}$	$Ku_{\parallel}$	g
	nm	kJ/m^3	kJ/m^3	
$Co_{50}Fe_{50}$	4	41.9 ± 0.2	3.5 ± 0.1	2.10
	6	43.0 ± 0.1	0.94 ± 0.08	2.09
	8	41.1 ± 0.2	3.6 ± 0.1	2.11
	20	27.5 ± 0.7	2.78 ± 0.06	2.11
$Ni_{81}Fe_{19}$	4	2.19 ± 0.04	2.19 ± 0.04	1.91
	6	0.16 ± 0.06	0.87 ± 0.05	1.90
	8	0.96 ± 0.01	2.9 ± 0.06	1.90
	20	0.82 ± 0.04	1.21 ± 0.05	1.92

Table 7.1: Magnetocrystalline anisotropy parameters and g-factor for the $Co_{50}Fe_{50}$ and $Ni_{81}Fe_{19}$ modes of the heterostructures, determined by fitting the angle- and field-dependent FMR frequency for multilayer samples with indicated TI thicknesses.

7.3 Coupling Across a Topological Insulator

Two types of measurements were performed to investigate the presence of a dynamic coupling across the TI spacer layer. First, the Gilbert damping of the two magnetic layers was determined using frequency-dependent VNA-FMR, fitting the gradient of linewidth to extract α. As the magnetic layers should not change as a function of TI thickness, any changes in damping can be attributed to the presence of spin pumping, or another type of coupling to the TI. Secondly, XFMR measurements were performed on samples with t_{TI} = 4, 8, 20 nm. As XFMR selectively probes both spin source and spin sink layers it should provide an indication of the presence of a long-range dynamic coupling, distinguishing between spins pumped *into* and *through* the TI.

7.3.1 Gilbert Damping as a Function of TI Thickness

Figure 7.4 shows the measured damping parameter, α, for the NiFe and CoFe layers as a function of the thickness of the TI interlayer. A linear increase is observed up to 20 nm, wherein the spin pumping component represents a significant fraction

of the total damping, indicating a large transfer of angular momentum to the TI. It is important to compare this result with other materials. As discussed before, damping in trilayers normally drops exponentially with spacer thickness [23], as scattering within the non-magnetic (NM) layer is a much less efficient sink for angular momentum than absorption by a second ferromagnet. This trend is seen, for example, in the Cr spin valves studied in chapter 8. Here, however, damping increases with TI thickness, suggesting not only that the TI is a very efficient spin-sink, but that the pure spin current can penetrate several nanometres into the TI. If the spacer layer does not transmit spins the damping saturates as soon as a continuous layer is formed, as shown in chapter. Here, the consistently increasing damping suggests that the spin current can penetrate some distance into the TI, which is a more efficient spin sink than the second FM layer. One interpretation is that while it is possible to drive a spin current into the TI, recovering that pumped angular momentum at the second interface is more difficult. As a spin current is driven into the TSS a spin imbalance develops, which is converted to a charge current [126]. The scattering of such conduction electrons within the bulk of the TI could then provide a mechanism for efficient absorption of pumped angular momentum. Therefore, a thicker TI leads to a higher Gilbert damping, as a thinner layer still allows some spin backflow into the on-resonance FM layer.

Another interpretation can arise when considering the form of equation (2.27), which yields the spin pumping damping in a trilayer structure. The spin diffusion length in a nonmagnetic material is determined by its Fermi velocity, and the spin-flip and momentum scattering lifetimes. In most materials the spin-flip scattering lifetime (τ_{sf}) is longer than the momentum scattering lifetime (τ_m), yielding an exponential decay of damping with increasing spacer layer thickness. If the $\tau_m > \tau_{sf}$, however, the sense of the resulting exponential reverses and the damping increases with increasing spacer layer thickness, as observed here. This effect

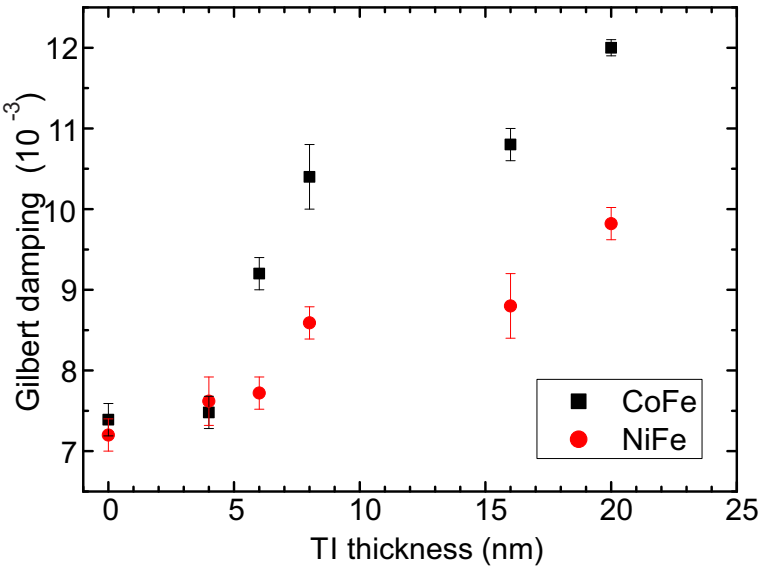


Figure 7.4: Calculated damping factor as a function of thickness of the TI interlayer for CoFe (black) and NiFe (red) layers. Error bars represent the uncertainty on linear fits to linewidth as a function of frequency. Figure from Ref. [60].

could arise in the bulk of the topological insulator, where the strong spin orbit coupling drives a band inversion. This suggestion must be treated with care, however, and is presented here as an mathematical curiosity rather than a serious interpretation of the results.

It is instructive to analyse the spin pumping results in the analytical framework of the STT in normal metals. Equation (2.28) can be rearranged to yield the spin mixing conductance, $\tilde{g}_{\uparrow\downarrow}$. Considering, for example, the case of the NiFe ($M_s = 0.906 \times 10^6$ A/m) layer in the $t_{\mathrm{TI}} = 20$ nm sample, the spin pumping damping can be extracted by comparison with a bare NiFe layer, yielding $\alpha_{\mathrm{sp}} = (2.6 \pm 0.3) \times 10^{-3}$. The spin mixing conductance is then $\tilde{g}_{\uparrow\downarrow} = (4.2 \pm 0.5) \times 10^{15}$ cm^{-2}. Performing the same calculation for the CoFe layer in this sample ($M_s = 1.76 \times 10^6$ A/m) gives $\tilde{g}_{\uparrow\downarrow} = (2.49 \pm 0.1) \times 10^{15}$ cm^{-2}. The discrepancy between the results for the two layers points towards dissimilar interfaces. This most likely arises due to the requirement for low temperature deposition of the NiFe layer, in order to preserve crystal quality within the Bi_2Se_3 layer, which could

also limit intermixing or reduce the mobility of the Se into the adjacent FM layers. Transmission electron microscope measurements were performed in an attempt to investigate this, but the preparation was not successful, and no useful data could be obtained.

Since the damping does not completely saturate these values should be regarded only as a lower limit on the effective spin mixing conductance available in FM/TI heterostructures. These values are comparable to the spin mixing conductances calculated by Jamali *et al.* from their inverse spin Hall effect measurements [26]. They are greater than previous reports for even a good spin conductor such as Ag, where $\tilde{g}_{\uparrow\downarrow} = 1.1 \times 10^{15}$ cm^{-2} [23]. Note that the calculation does not separate pumping into the bulk and surface state, which display very different spin dynamics. The value should therefore be considered only as a rough estimate of the effective spin mixing conductance that is present in TI heterostructures.

7.3.2 Layer-Resolved Magnetodynamics

VNA-FMR measurements showed that the TI spacer layer functions as an efficient spin sink, with a large interfacial spin mixing conductance. It is, however, unclear whether the pure spin current is transmitted across the TI, or simply absorbed. XFMR is able to elucidate this issue, as the layer-specific measurements remove much ambiguity from the results. In this way, pumping into the TI (visible as an increased linewidth of resonance due to additional damping terms) and pumping through the TI (visible as alterations to the phase of precession of the off-resonance layer) can be separated.

XFMR measurements were performed on beamline I10 at Diamond Light Source and beamline 4.0.2 at the Advanced Light Source, measuring amplitude and phase of precession of magnetisation across resonance at 4 GHz. The precession of the

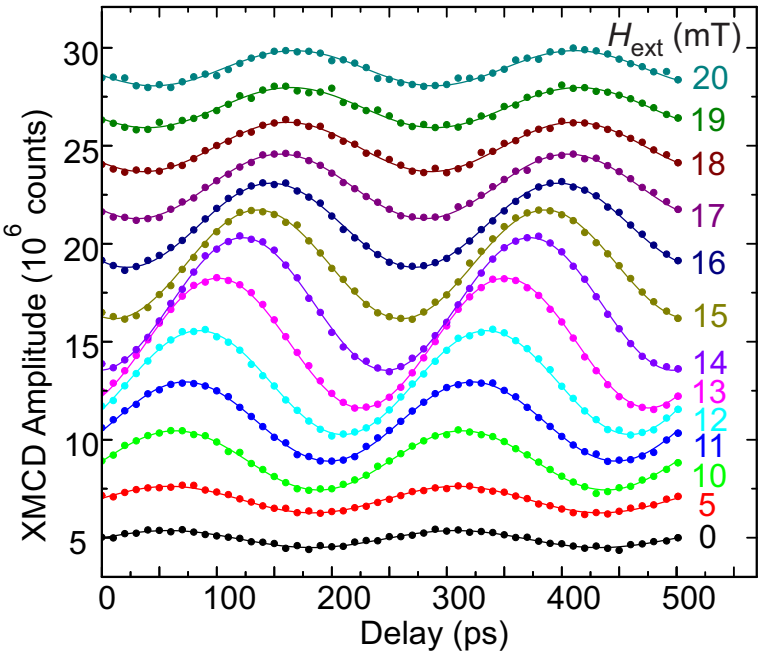


Figure 7.5: XFMR delay scans for NiFe continuously driven at 4 GHz for the t_{TI} = 8 nm sample. Varying static bias field indicated by colour of lines, offset for clarity, showing increase in amplitude and phase shift across resonance at 14 mT. Solid lines are sine curve fits to the data. Figure from Ref. [60].

magnetisation of the Ni moments in the NiFe layer is shown in Fig. 7.5 for t_{TI} = 8 nm, showing the sinusoidal variation of magnetisation alignment. The increase in amplitude of precession and phase shift is clearly visible, showing the resonant field at 14 mT. Sine curves were fitted to the delay scan data to extract values of phase and amplitude of precession as a function of external bias field. Away from resonance the cone angle of precession decreases, leading to a corresponding decrease in data quality and larger uncertainty on fitted values.

Figure 7.6 shows the phase of precession determined in this way for t_{TI} = 4 nm and 8 nm. Evidence of coupling across the spacer layer manifests as off-resonance precession and phase shifts in the spin-sink layer. Indications of coupling can be observed in the CoFe layer for t_{TI} = 4 nm [Fig. 7.6(a)] and the NiFe layer for t_{TI} = 8 nm [Fig. 7.6(b)]. The modulation of the phase in the CoFe layer displays a shape akin to the bipolar variation arising from spin pumping [15],

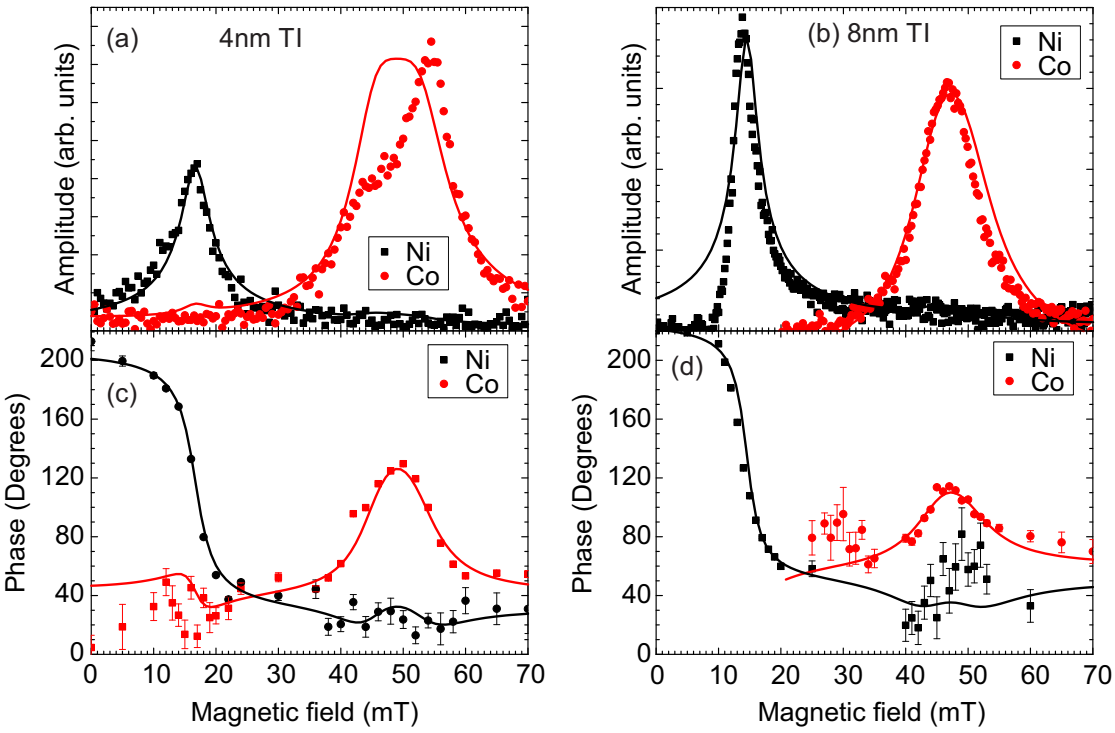


Figure 7.6: Amplitude (top row) and phase (bottom row) of precession of magnetisation for $Ni_{81}Fe_{19}$(black) and $Co_{50}Fe_{50}$(red) layers at 4 GHz driving frequency for t_{TI} = 4 nm and 8 nm [(a,c) and (b,d), respectively]. The drop and recovery in phase across the Co mode is caused by the superposition of the two modes, corresponding to canted and collinear magnetisation, as can be seen in Fig. 7.3. Error bars arise from uncertainty on fits to the time-resolved precession, see Fig. 7.5. Solid lines are fits to the data using the model presented in section 5.3 and parameters from VNA-FMR measurements. The model does not account for reduced XFMR signal due to magnetisation canting, and thus over-estimates the lower branch fo the CoFe resonance.

but is rather weak, perhaps due to scattering in the TI layer suppressing spin pumping. There is no corresponding variation of amplitude, due to the thick FM layers employed (30 nm) being much larger than the typical penetration depth of a pure spin current into an FM (∼2 nm). The phase of precession is, however, a much more sensitive probe and can be used to detect the presence of a weak coupling. Result from the modelling approach outlined in section 5.3 and values for magnetocrystalline anisotropy and spin pumping determined by VNA-FMR measurements provide only an approximate fit to the off-resonance precession. While there are indeed phase variations akin to those predicted, the model under-

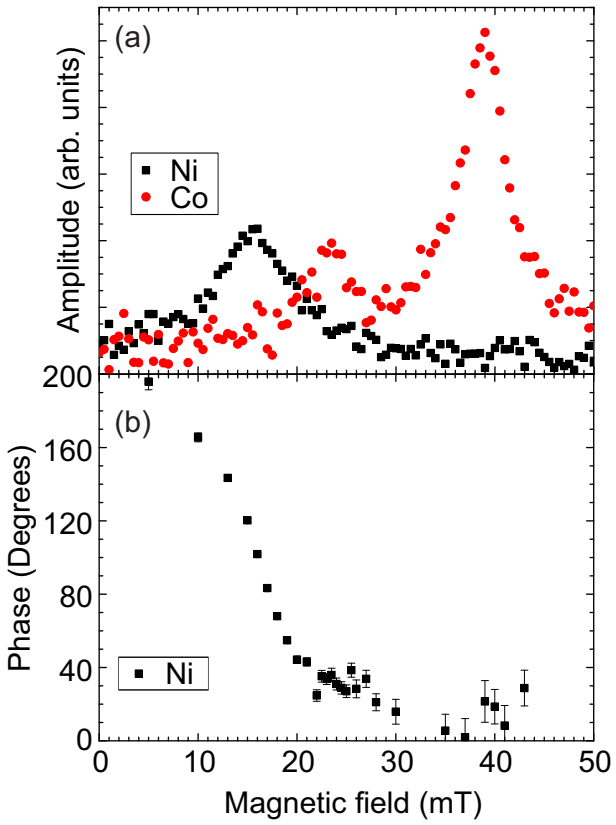


Figure 7.7: Amplitude (a) and phase (b) of precession of magnetisation for NiFe (black) and CoFe (red) layers at 4 GHz driving frequency for $t_{\mathrm{TI}} = 20$ nm. Data for the Co magnetisation was gathered using the field scan method, therefore only amplitude data is available. The lower magnetocrystalline anisotropy of the CoFe layer in this sample causes the Co resonance to occur at a lower frequency. Error bars arise from uncertainty on fits to the time-resolved precession, see Fig. 7.5.

estimates their amplitude for $t_{\mathrm{TI}} = 8$ nm. Further, it does not account for the trend for linear decrease in phase away from resonance – this would require a significantly larger spin pumping than implied using VNA-FMR. This failing of a conventional model suggests that the spin transfer properties of TIs are more complicated than in most normal metals, as expected from a non-trivial quantum system.

XFMR measurements were also performed on the sample with 20 nm Bi_2Se_3 (shown in Fig. 7.7). The flat phase data shows no evidence of coupling between the two magnetic layers, suggesting that the TI suppresses the previously observed weak interaction between the FM layers. This finding shows that the TI

permits an indirect interaction over a length scale on the order of 10 nm, slightly larger to the spin diffusion length of 6.2 nm in Bi_2Se_3 calculated in Ref. [134].

Taking the two techniques together, a more complete picture of spin transfer in these heterostructures can be obtained. First, the distinction between what they measured must be considered. VNA-FMR measures increased damping due to spin pumping out of a FM, while XFMR allows detection of modified precessional dynamics induced by spin pumping into a FM. The results in Fig. 7.4 indicate increased spin pumping with increasing TI thickness, suggesting that the TI functions as an excellent spin sink. However, transfer of the spin current is less efficient as damping of the spin current within the TI seems a preferable scattering channel to absorption by the second ferromagnet. XFMR, by contrast, shows a weak coupling between the two FM layers that persists for at least 8 nm, and could be attributed to the transmission of a pure spin current, most likely through the bulk of the TI. Measurements of the inverse spin Hall effect in a Bi_2Se_3/NiFe bilayer structure found the spin diffusion length to be (6.2 $\pm$ 0.15) nm at room temperature [134], which is consistent with these findings, allowing for small variations between samples and interfaces. The continued increase of Gilbert damping with TI thickness confirms that the spin current can persist within the TI, the fact that only limited coupling is observed suggests that transmission across the FM/TI interface and the topological surface state is more limited. Calculations of the spin mixing conductances, $\tilde{g}_{\uparrow\downarrow}$, of the two FM/TI interfaces showed that they are dissimilar, most likely due to differences in the growth protocols. If the quality of the interfaces can be improved, this suggests that even higher values of $\tilde{g}_{\uparrow\downarrow}$ could be obtained.

The novel properties of TIs could open a second mechanism for interaction between the two separated ferromagnets. In the case of a sufficiently thin film, the top and bottom surface states can experience a tunnelling effect that suppresses the

formation of the true topological surface state [135, 136]. In the case of Bi_2Se_3 this thickness is 6 nm. When this is the case, direct communication between the top and bottom interfaces should be possible, negating the presence of the bulk entirely. Since surface roughness or other imperfections can cause the surface state to retreat [137], it is possible that this direct interaction is responsible for the coupling observed for $t_{\mathrm{TI}} = 4$ nm and 8 nm, while the distinct states at $t_{\mathrm{TI}} = 20$ nm do not allow this. In this interpretation, the increased Gilbert damping stems from spin pumping into the bulk, while the interaction observed in XFMR stems from direct coupling across the TI.

7.4 Anti-Damping Torques from Simultaneous Resonance

While the VNA-FMR and XFMR measurements performed in the previous section showed that the TI layer can absorb a spin current, they did not provide a conclusive answer as to the nature of the coupling between the two ferromagnetic layers. While a dynamic interaction through spin pumping is a likely candidate, another interaction mediated by the topological surface state is also a possibility. Another experimental approach is therefore required to provide more information as to the origin of the interaction shown in Fig. 7.6.

The additional damping caused by spin pumping arises due to the loss of energy when spins are pumped out of the on-resonance layer. In the same way, this outflow of energy can induce precession in the off-resonance layer, through the spin transfer torque, when it is absorbed. These effects enter the LLG (equation (2.26)) as the damping and anti-damping constants α_{ii}^{sp} and α_{ij}^{sp}, respectively. However, if both layers are simultaneously on-resonance then the anti-damping from the incoming spin current can partially compensate the additional damping

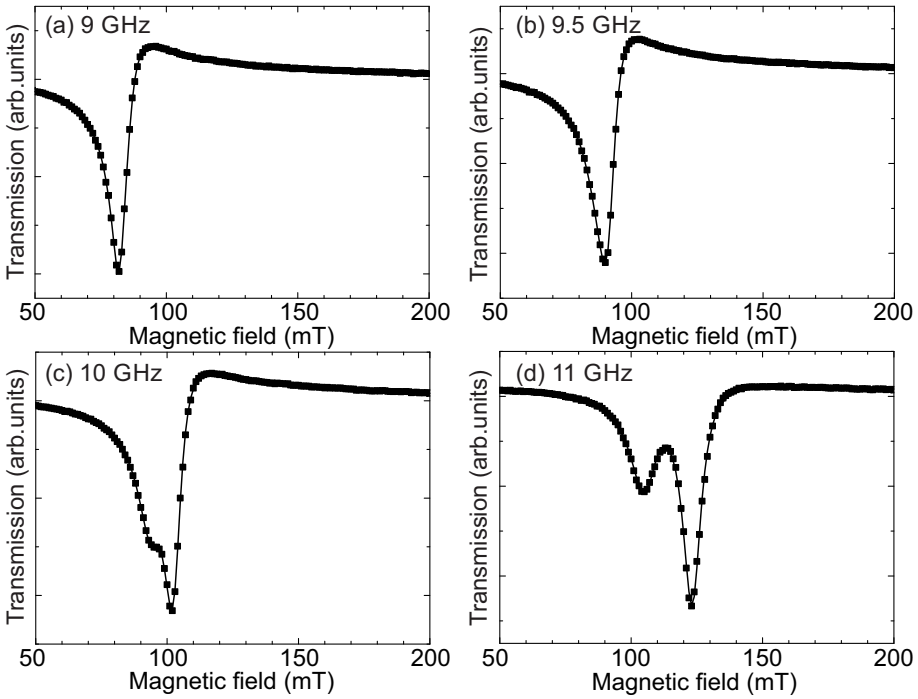


Figure 7.8: VNA-FMR data for a sample with $t_{\mathrm{TI}} = 8$ nm, showing the change in resonance field as a function of excitation frequency. The modes completely overlap at 9 GHz (a), making it difficult to separate individual contributions to linewidth and amplitude. They move apart as frequency increases (b,c), and are fully resolved at 11 GHz (d). Black squares are data points, solid lines are fits to the data using two asymmetric Lorentzians.

from the outgoing spin current. Experimentally, this is observed as a decrease in resonance linewidth as the separation of the resonances of the two layers approach one another. In heterostructures with a strong magnetocrystalline anisotropy it is possible to use the angular dependence of the resonance condition to alter the separation of the two resonances, and identify signs of spin pumping. This technique is made somewhat more complicated by the difficulty of obtaining accurate fits to the overlapping Lorentzians of two resonances in close proximity. This is illustrated in Fig. 7.8. Furthermore, spin pumping is not the only source of angular variation of resonant linewidth: mosaic broadening and two magnon scattering can also play a role. Nevertheless, this technique can offer valuable insights into the relaxation processes of spin valves.

7.4.1 Vector Network Analyser Measurements

The steps to evaluate the presence of anti-damping torques are shown in Fig. 7.9 for a sample with $t_{\mathrm{TI}} = 8$ nm, demonstrating the difficulty of obtaining unambiguous data. In particular, significant additional linewidth broadening occurs when the magnetisation is canted away from the static bias field, as happens at low fields in the vicinity of a magnetocrystalline hard axis. An example of this can be seen in Fig. 7.9 (e) below 8 GHz. This effect can cause the apparent resonant linewidth to increase by a factor of ten or more, but does not have a physical relation to the spin pumping process. For this reason, such regions of data cannot be used and must be avoided.

The correlation between mode separation and linewidth at 10 GHz is shown in Fig. 7.9(f). The linewidth of the CoFe resonance decreases as the separation decreases, which suggests the presence of a spin-pumping mediated dynamic interaction. Linewidth decreases when the spin torques exerted by the pure spin current partially cancel. However, a slight increase in damping is observed in the $Ni_{81}Fe_{19}$, which in theory should show the same trend as in the $Co_{50}Fe_{50}$. The discrepancy could be related to an intrinsic damping anisotropy, exacerbated by dissimilar spin pumping efficiencies from the two layers, as evidenced by a lower spin mixing conductance observed for the $Co_{50}Fe_{50}$/TI interface, indicating that spins are less readily pumped from the $Co_{50}Fe_{50}$.

The effects of mode proximity on the linewidth at 8.9 GHz is shown in Fig. 7.10 for t_{TI}= 4, 6, and 8 nm. In all cases the linewidth of the CoFe decreases as the modes move towards one another, dropping to a minimum of about 3.5 mT, suggesting that this is the intrinsic linewidth for the bare film when the spin pumping damping cancels. However, the linewidth of the NiFe is largely unchanged across the same range, and even shows a slight increase as the modes approach crossover, which

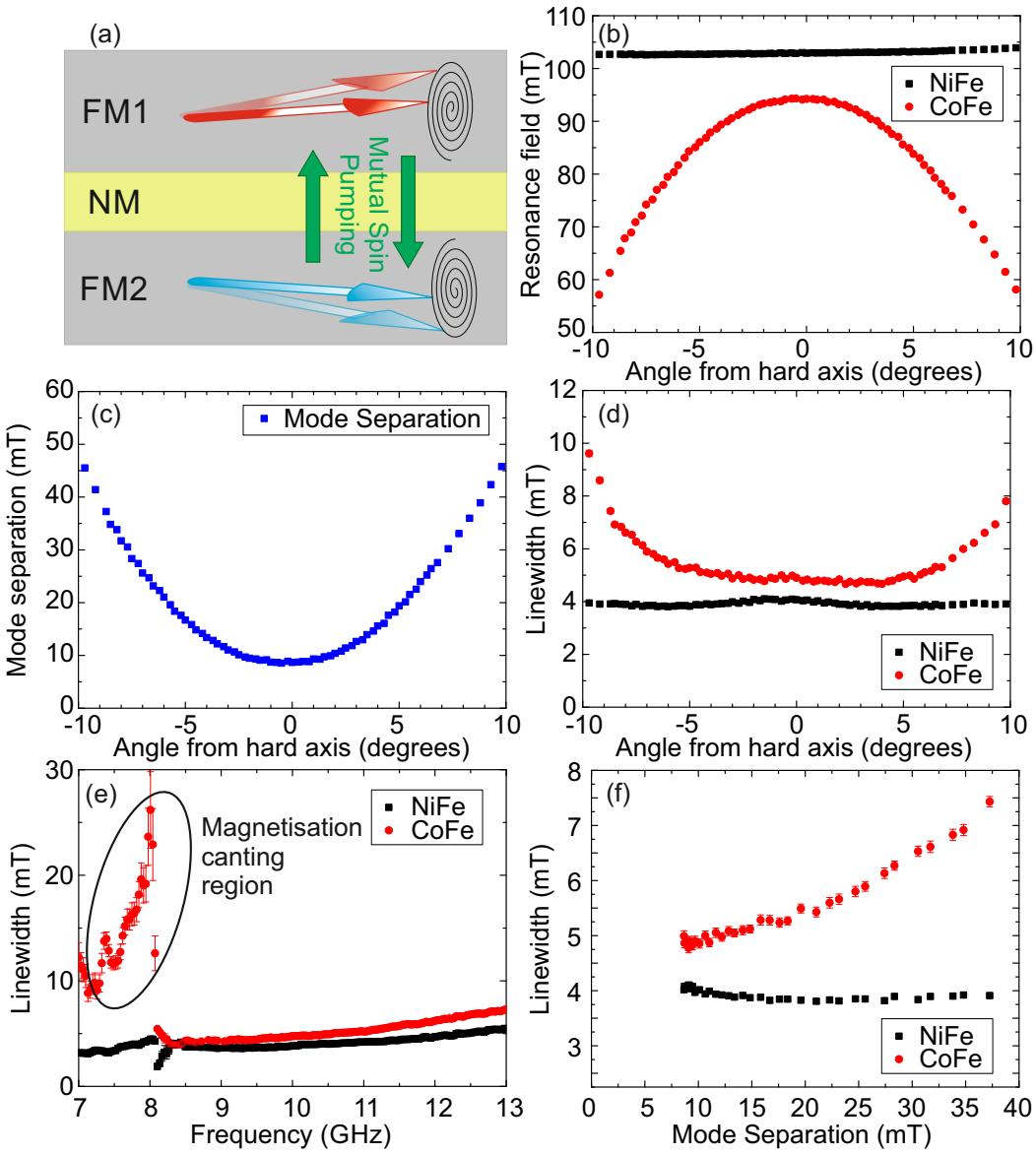


Figure 7.9: Analysing anti-damping torques in FMR. The concept of mutual spin pumping is outlined in (a). Panel (b) shows the angular variation of linewidth at 10 GHz around the magnetocrystalline hard axis of the CoFe layer, with the mode separation plotted in (c). Variation of linewidth with respect to bias field angle is shown in (d), which indicates the difficulty of separating variation due to mutual spin pumping and other relaxation mechanisms. Panel (e) shows frequency dependent linewidth performed 5° away from the hard axis. Two regions of unusable data are shown. First, where overlapping resonances lead to spurious linewidths, in the region 8 GHz to 8.5 GHz. Secondly, the canting of magnetisation at low bias fields leads to the drastic increase in CoFe resonant linewidth in CoFe below 8 GHz. Taking into account these limitations, the variation of linewidth as a function of mode separation at 10 GHz is plotted in (f). All error bars arise from uncertainty on fits to the resonances.

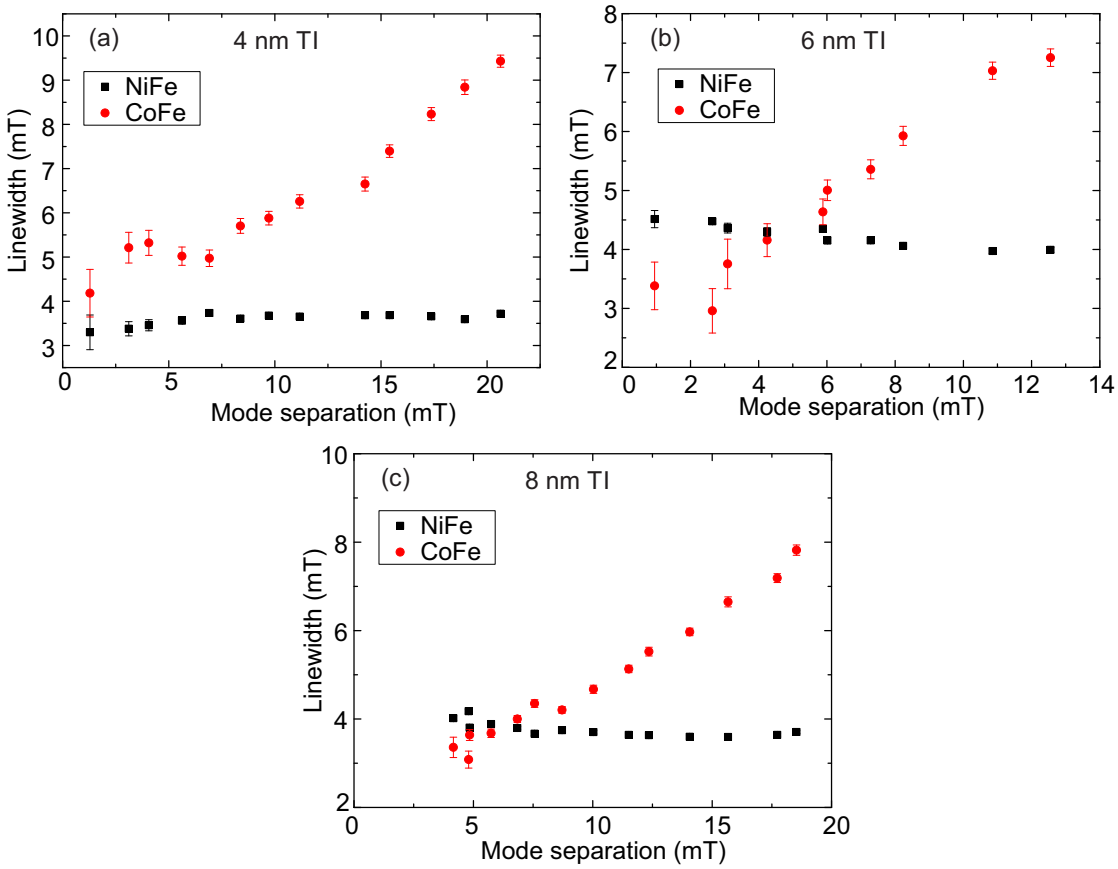


Figure 7.10: Variation of linewidth at 8.9 GHz as a function of separation of the modes for t_{TI}= 4, 6, 8 nm [(a), (b), (c), respectively]. A systematic variation is only evident in the CoFe layer.

contradicts the previous interpretation of anti-damping torques. The change in linewidth of the CoFe could then instead come from misfitting caused by overlap, or else artificial broadening due to the canting of magnetisation away from the bias field. The data indicates the presences of anti-damping torques, in turn suggesting that the interaction across the TI is mediated by spin pumping, but cannot be conclusive due to the aforementioned difficulty interpreting the data.

No equivalent data could be obtained for t_{TI}= 20 nm due to differing anisotropy parameters (see table 7.1) meaning that the closest approach of the modes is 10 mT. Further, due to increased inhomogeneous broadening the modes are rather wide, making fitting difficult in the overlap regions. The NiFe layer in the sample with t_{TI}= 20 nm appears to be of lower quality than in other samples, possibly

due to interdiffusion with the Bi_2Se_3 layer, or else problems with stoichiometry during growth. It is also possible that the surface roughness of the Bi_2Se_3 increases significantly for thicker films, leading to a poor quality NiFe film. The problem of fitting in overlap regions is partially addressed by measuring with XFMR.

7.4.2 Layer-Resolved Measurements

XFMR offers a solution to some of the problems inherent in measuring overlapping resonances, as its element-selectivity ensures that only one layer is measured at a time. Further, it is less sensitive to magnetisation canted away from the bias field, due to reduced projection along the x-ray beam in turn reducing the dynamic XMCD signal. The first results gathered in this way are shown in Fig. 7.11, where the amplitude of precession of magnetisation is shown around resonance for $t_{\mathrm{TI}} =$ 4 nm. The anisotropy of the CoFe layer is used to tune the relative position of the two layers. The move from overlapping resonances to a separation of $\sim$10 mT causes the linewidth to increase by approximately 15%, although the lower data quality of the CoFe leads to large uncertainty on the fit. Nevertheless, a reduction in linewidth is observed in the NiFe layer, indicative of anti-damping arising form mutual cancellation of spin pumping.

Further results of separation-dependent linewidth at 8 GHz for samples with t_{TI} = 8 nm and $t_{\mathrm{TI}} = 20$ nm, are plotted in Fig. 7.12. The data show a narrowing of resonant linewidth with decreasing mode separation for $t_{\mathrm{TI}} = 8$ nm, though as with the VNA-FMR measurements, only in the CoFe layer. This suggests that the linewidth narrowing previously observed is a genuine effect, perhaps stemming from simultaneous spin pumping.

XFMR overcomes the difficulties previously presented by the increased linewidth of the NiFe mode in the $t_{\mathrm{TI}} = 20$ nm sample, allowing measurements of the two

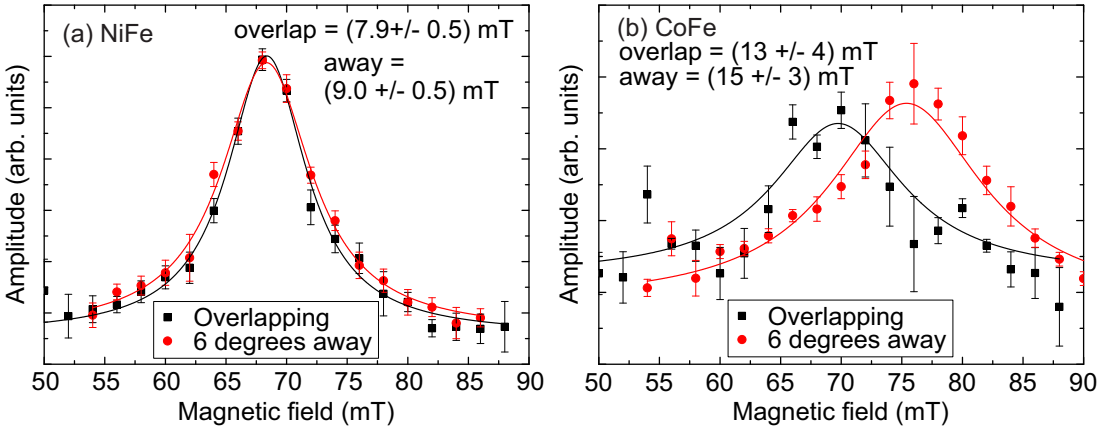


Figure 7.11: Amplitude of precession of magnetisation at 6 GHz as measured by XFMR for a sample with $t_{\mathrm{TI}} = 4$ nm for the NiFe (a) and CoFe (b) layers. A small reduction in linewidth is observed for the NiFe layer, while the large error bars on the weaker CoFe signal preclude drawing a conclusion. Error bars on points arise from uncertainty on sine fits to the XFMR delay scans.

resonances as they enter the crossover region. The linewidth of the NiFe has increased threefold, in line with the significantly increased damping measured by VNA-FMR. Further, due to reduced magnetocrystalline anisotropy in the CoFe layer the closest possible approach is 10 mT. Figure 7.12(b) shows the linewidth of both layers as a function of mode separation, where the variation in linewidth is within the error on the measurements. There is thus no evidence of anti-damping torques acting to reduce linewidth in the case of mutual spin pumping. This indicates that the thicker TI interlayer effectively suppresses all interactions between the two FM layers, in agreement with measurements of phase and amplitude of precession.

However, it remains unclear why little to no variation is observed in the NiFe layer. It is possible that the problem relates to dissimilar efficiencies of spin pumping across the FM/TI interfaces. This discrepancy is also present in measurements of phase and amplitude of precession across resonance, where variations in phase take place in only one layer, as discussed above. Again, these results highlight the critical importance of high quality interfaces for spin pumping experiments, and

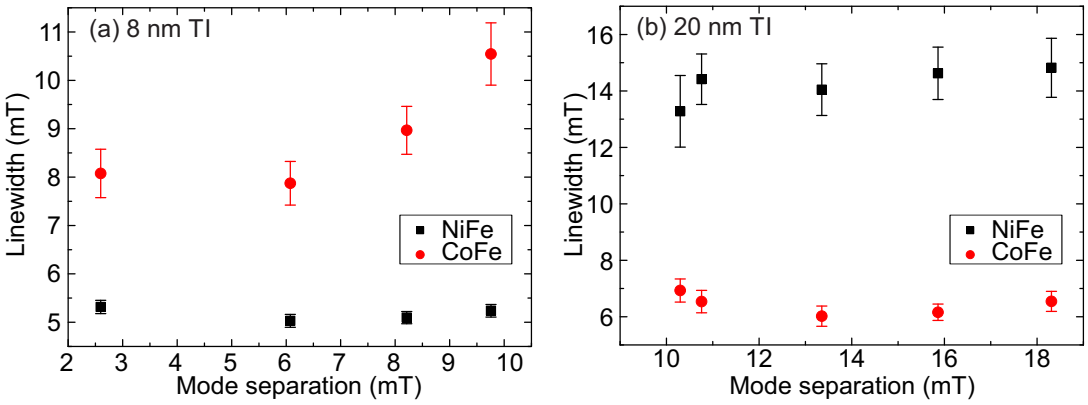


Figure 7.12: Linewidth of resonance measured by XFMR as a function of mode separation for both layers in structures with $t_{\mathrm{TI}} = 8$ nm, (a) and $t_{\mathrm{TI}} = 20$ nm (b). A decrease in linewidth is observed for the CoFe layer for $t_{\mathrm{TI}} = 8$ nm, while in all other cases any variations are within error. Note that the NiFe resonance is significantly broader in the case of the $t_{\mathrm{TI}} = 20$ nm sample. Error bars on points arise from uncertainty on fits to the real and imaginary components of resonance.

show that there is significant space for further study of spin transfer in FM-TI heterostructures.

7.5 Temperature Dependence of Spin Pumping

To perform low temperature measurements in POMS a Janis cryo-insert is used. The CPW and associated RF cabling are mounted on the cryostat, which incorporates an oxygen-free high purity copper sample stage, heater and two thermocouples, one mounted close to the sample and one mounted at the end of the cryostat itself. The insert can be cooled by liquid nitrogen or liquid helium, with a base temperature of approximately 7 K, and good thermal stability in the range 10 K to 300 K.

A key challenge when measuring transport phenomena in topological insulators is the separation of bulk and surface conduction channels. Despite their name, TIs in fact typically have a sheet resistance on the order of 100 Ω, due to conduction through the bulk of the material. This conduction can be reduced by cooling the

sample to low temperatures, freezing out conduction channels aside from those in the topologically protected surface state. Indeed, the first measurements of the quantum anomalous Hall effect in a ferromagnetically doped TI were performed at 30 mK [118]. It is thus important to study how the measurements of spin pumping in the FM-TI heterostructures are affected by temperature. The spin pumping process is dependent upon the spin flip and momentum scattering lifetimes, so should be sensitive to bulk transport. Spin pumping into the surface state, however, should not be affected by a change in temperature.

The temperature dependence of damping in ferromagnets must also be considered, as the various processes that contribute to energy dissipation can each be affected differently. For example, the additional damping due to the presence of slow relaxing impurities (see chapter 4) increases as the temperature decreases, as the population of the $4f$ levels of the rare earth impurity ions depends strongly upon temperatures [58]. Similarly, the scattering of itinerant electrons in the ferromagnet is enhanced at lower temperatures, leading to an increased damping [14, 138].

Temperature dependent measurements were performed on two samples ($t_{\mathrm{TI}} =$ 4 nm and $t_{\mathrm{TI}} = 8$ nm), which were mounted for VNA-FMR in the standard flip-chip geometry. Field-frequency transmission maps were recorded with the bias field aligned along the easy axis, in the temperature range 10 K to 300 K. The Gilbert damping was then determined from the frequency dependence of resonant linewidth, according to equation (2.21). The results are shown in Fig. 7.13.

While there are weak indications of a variation of Gilbert damping with temperature, no pattern of increasing or decreasing damping emerges. The NiFe layers in the two samples appear to show opposite trends, with a slight decrease in damping at low temperatures for $t_{\mathrm{TI}} = 4$ nm, and a slight increase for $t_{\mathrm{TI}} = 8$ nm, but in both cases the variation is extremely slight, even comparable to the uncertainty on the data points. The data for the CoFe layers has larger measurement uncertainty,

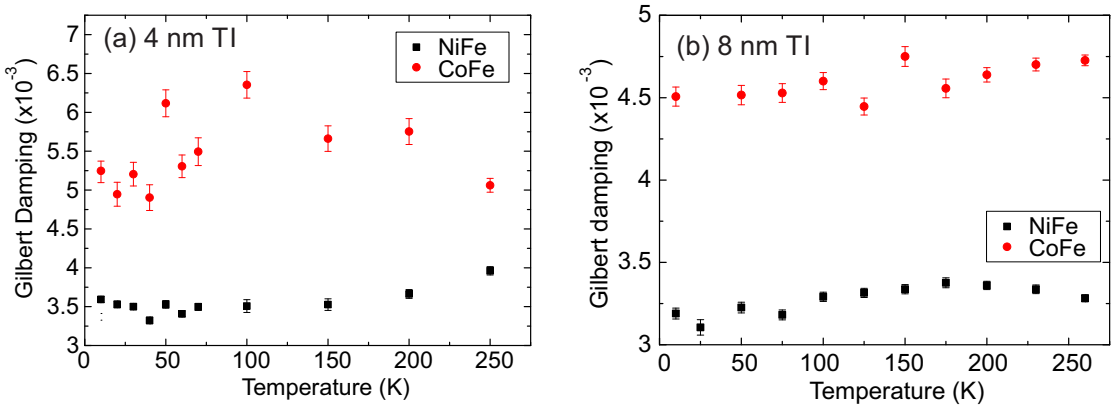


Figure 7.13: Gilbert Damping for each layer as a function of temperature for samples with $t_{\mathrm{TI}} = 4$ nm (a) and $t_{\mathrm{TI}} = 8$ nm (b). In both cases there is little evidence of systematic variation in temperature. Error bars arise from uncertainty on fits to frequency dependent linewidth, and in the case of the NiFe layer are comparable to point size.

but no systematic variation at low temperatures.

These results indicate that there is no variation of spin pumping with temperature, suggesting that the suppression of bulk conduction channels does not have a significant impact on the efficiency of the transmission of a pure spin current. While this may initially seem counter-intuitive, it is important to note that the symmetry-protected surface state has been observed at room temperature [135]. Therefore, any transmission of spin angular momentum through the surface state should persist at all temperatures. Similarly, the absorption of a pure spin current within the bulk of the TI seems to occur across the full temperature range, suggesting that the spin flip scattering does not have a strong temperature dependence.

7.6 Conclusion

This chapter has concerned the fabrication and characterisation of trilayer magnetic heterostructures incorporating a topological insulator, based on the tradi-

tional spin valve device architecture. Through VNA-FMR and XFMR, the spin dynamics of this novel heterostructure have been studied, aiming to understand the spin transfer processes mediated by the TI. Varying the thickness of the TI spacer layer, it was observed that the TI functions as an efficient angular momentum sink. XFMR measurements, however, confirmed the presence of a weak interaction between the two ferromagnets, able to persist for at least 8 nm, and possibly mediated by the topological surface state. The maximum spin mixing conductance of the $Co_{50}Fe_{50}$/TI interace was calculated to be $\tilde{g}_{\uparrow\downarrow} = (2.49 \pm 0.1) \times 10^{15}$ cm^{-2}, while that of the $Ni_{81}Fe_{19}$/TI interface was $\tilde{g}_{\uparrow\downarrow} = (4.2 \pm 0.5) \times 10^{15}$ cm^{-2}, comparable with that of a good spin conductor such as Ag.

To study the coupling in more detail, measurements of resonance linewidth were performed as a function of bias field angle. By bringing the resonances of the two layers into close proximity, it was possible to observe anti-damping torques that lead to a narrowing of linewidth, a characteristic of spin pumping. This suggets that the interaction across the TI is a dynamic exchange mediated by spin pumping, as opposed to a self-coupling of the surface state or a similar unusual mechanism. Temperature dependent measurements of Gilbert damping showed no significant variation down to 10 K, indicating that a suppression of the bulk conduction channels of the TI does not fundamentally alter its spin-transfer properties.

These results show the great potential of TIs for device applications, as these effects can be observed at room temperature and low magnetic fields, as well as being a fertile ground for investigation of fundamental physical phenomena. Further work is required to improve understanding of the FM/TI interface and separate bulk and surface conduction, but these initial results show that FMR is a valuable tool to develop greater understanding of this new materials class.

Chapter 8

Anisotropy Imprinting Through Spin Pumping

8.1 Motivation

This chapter details an investigation into the spin transfer properties of Cr, studying how the static and dynamic exchange interactions can be controlled in spin valves with Cr interlayers. While the oscillatory nature of the static interaction in such systems is well known (see, for example, Refs. [30,139]), interest in spin pumping in Cr has developed in recent years [61,140]. Furthermore, mechanisms for angular control of spin pumping have started to recieve more attention [53,141–143], as a way to fine tune applications of spintronic devices and to gain a deeper understanding of spin transfer in magnetic multilayers. The investigation outlined here aims to combine a study of angular control of spin pumping with a detailed examination at how static and dynamic coupling can compete and combine to modify the magnetodynamics of spin valves.

Spin valve samples were fabricated by MBE, with one magnetic layer being epitax-

ial, with well-defined magnetocrystalline easy and hard axes ($Co_{50}Fe_{50}$) and the other being polycrystalline, resulting in isotropic magnetic behaviour ($Ni_{81}Fe_{19}$). The thickness of the Cr interlayer was varied between 1 nm and 10 nm, tuning the strength of both the static and dynamic interactions. SQUID-VSM and VNA-FMR are used to quantify the strength and nature of the static interaction, as it changes from preferring parallel to antiparallel alignment. Analysis of the change in resonance linewidth as a function of Cr thickness reveals the presence of spin pumping, while the angular variation of the linewidth is used to determine the anisotropic component of the dynamic interaction. Finally, XFMR is used to measure the layer-resolved precessional dynamics, showing how the angular variation of spin pumping modifies the spin transfer torque experienced by the layer absorbing the pure spin current.

8.1.1 Angular Control of Spin Pumping

Gilbert damping can have a large anisotropy, as discussed in the case of the doped films discussed in chapter 4. Aside from the additional damping induced by rare earth impurities, several other contributions are possible, including two-magnon scattering [50], wherein the uniform FMR mode scatters into higher order excitations, mosaic broadening due to sample inhomogeneities [17, 50, 144], and anisotropic Gilbert damping arising due to canting of magnetisation away from the applied magnetic field [17].

Spin pumping can also have a pronounced angular dependence, making unambiguous determination of the origin of any anisotropy of Gilbert damping rather challenging. The most prominent mechanism by which an anisotropy of spin pumping can arise is a misalignment of the magnetisation of the two magnetic layers in the heterostructure [53, 141, 145]. The absorption of the pumped angular momentum is more efficient when the two layers are aligned antiparallel, as compensation of

the pumped angular momentum drops [142]. For the same reason, spin pumping tends to be larger when the modes precess in anti-phase as angular momentum compensation again drops. Therefore, it is theoretically possible to modulate the damping further by switching the optical/acoustic character of the resonances of the two layers [146]. This can be achieved in trilayers with a sufficiently strong static coupling to transfer precession between the two layers, and suitable magnetocrystalline anisotropy to change which modes occur at high or low frequency. However, layer-resolved measurements of amplitude and phase of precession cast some doubt on this interpretation, as the modulation of phase along a hard axis makes straightforward interpretation of the character of the resonances difficult. It has also been suggested that stray fields from domain walls in the spin sink layer can provide an effective dipolar field that acts as an additional damping term on the precession of the free layer [143].

Another possible cause of an apparent angular variation of spin pumping, distinct from those outlined above, is the presence of anti-damping torques from mutual spin pumping [107]. This effect was studied in topological insulator spin valves in section 7.4. As spin pumping drives angular momentum out of the spin source layer, and into the spin sink layer, it has both damping and anti-damping characteristics. When the resonance fields of the two layers are well separated the source layer experiences only damping, and the sink layer only anti-damping. However, in the case where both layers are simultaneously on resonance, both experience both damping and anti-damping effects, leading to partial or total compensation of the pumped spin angular momentum, and corresponding apparent reduction in Gilbert damping. Thus, for broad resonances with a significant angular variation, points of near crossing can also lead to an angular variation of linewidth, as the in-plane anisotropy of the resonant field causes the separation of the modes to decrease as a function of the angle of the applied magnetic field. One can see that

unambiguous identification of an angle-dependent component of spin pumping requires a careful, multi-technique study.

8.2 Sample Fabrication

Spin valve samples were prepared by molecular beam epitaxy in the μ-MBE (see section 3.1 and Ref. [78]) system on epi-ready MgO (001) substrates. The full structure is: MgO/$Co_{50}Fe_{50}$(5)/Cr(t_{Cr})/$Ni_{81}Fe_{19}$(5)/Ag(2) (thicknesses in nm), with t_{Cr} = 1, 1.5, 2, 5, 10 nm. The substrates were first annealed at 700°C to improve surface quality, before being cooled to 500°C for the deposition of stoichiometric $Co_{50}Fe_{50}$ (also referred to as CoFe) from effusion cells. The sample was then further cooled to room temperature for the deposition of the Cr and $Ni_{81}Fe_{19}$ (also referred to as NiFe) layers. This step is designed to inhibit intermixing of the layers, and further reduce the in-plane magnetic anisotropy of the NiFe by ensuring it has a polycrystalline structure. Reflection high energy electron diffraction was performed throughout the process to monitor crystal quality. Epitaxial growth was observed for the $Co_{50}Fe_{50}$, while the low-temperature deposition of Cr and NiFe yielded the desired polycrystalline material. This means that any observed angular variation must arise within the CoFe layer, or from a coupling to it.

8.3 Determining the Static Exchange

Figure 8.1 shows hysteresis loops measured by SQUID-VSM for samples with t_{Cr} = 1, 1.5, and 2 nm, in which three distinct coupling regimes can be clearly observed. For the 1 nm Cr layer [Fig. 8.1(a)] the strong ferromagnetic (F) interaction between the layers aligns the two magnetisations, leading to a single switching step

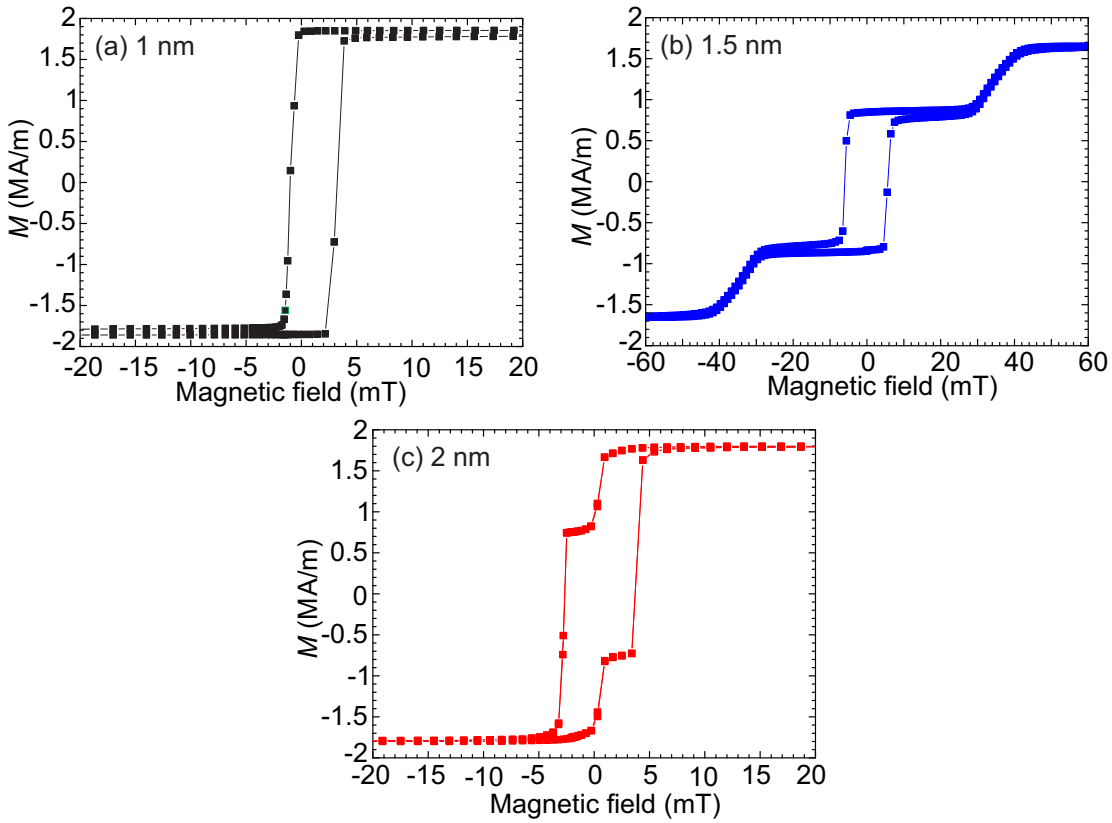


Figure 8.1: SQUID-VSM measurements of hysteresis loops for spin valves with t_{Cr} = 1 (a), 1.5 (b), and 2 nm (c). As the thickness of the Cr layer increases from 1 to 1.5 nm the coupling changes from F to AF, before being suppressed at t_{Cr} = 2 nm.

with a coercive field of 2 mT. For t_{Cr} = 1.5 nm [Fig. 8.1(b)], however, the coupling becomes antiferromagnetic (AF), with the NiFe and CoFe layers preferring antiparallel alignment. This oscillatory interlayer coupling is characteristic of the RKKY interaction, and has previously been observed by, e.g., Refs. [30, 139]. For t_{Cr} = 2 nm [Fig. 8.1(c)] the coupling is suppressed, with two distinct switching steps as the layers reverse independently.

Further insight into the effects of the static coupling can be gained by using XMCD to measure layer-specific hysteresis loops, as shown in Fig. 8.2. The incident photon energy was tuned to the L_3 edge of Co, Ni and Fe, with positive circular polarisation. The applied magnetic field was then swept from saturation in the positive (aligned with the beam) to saturation in the negative (aligned against

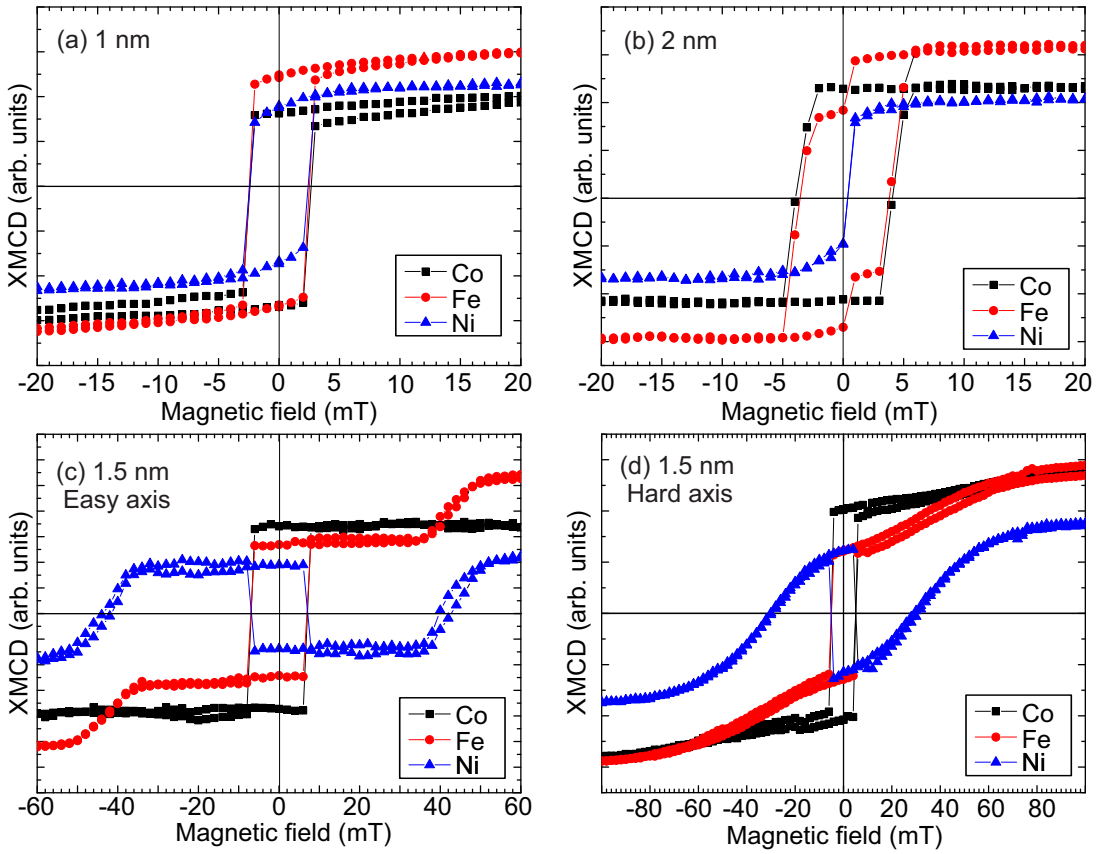


Figure 8.2: XMCD-hysteresis measurements of magnetisation reversal for spin valves with $t_{\mathrm{Cr}} = 1$ (a), 2 (b), and 1.5 nm (c,d), demonstrating the different switching behaviours induced by the static exchange coupling. Particular attention is paid to the case of $t_{\mathrm{Cr}} = 1.5$ nm, showing measurements with the magnetic field applied along the easy (c) and hard (d) axes of the CoFe layer.

the beam) and back. This was then repeated for negative polarisation, and the difference of the two curves taken. The Co and Ni signals measure each layer individually, while the Fe gives a weighted average over the whole structure.

Figure 8.2(a) shows the case of $t_{\mathrm{Cr}} = 1$ nm, where there is a strong ferromagnetic coupling between the two layers, acting to align the magnetisations of the NiFe and CoFe. Consequently, there is only a single switching step, with a coercive field of $\sim$3 mT, and all elements move together. By contrast, the case of no coupling between the layers is shown in Fig. 8.2(b), where $t_{\mathrm{Cr}} = 2$ nm. Here, the magnetisations are entirely independent, with NiFe having a coercive field of almost zero, while CoFe has 5 mT. Therefore, at this thickness of Cr there is no

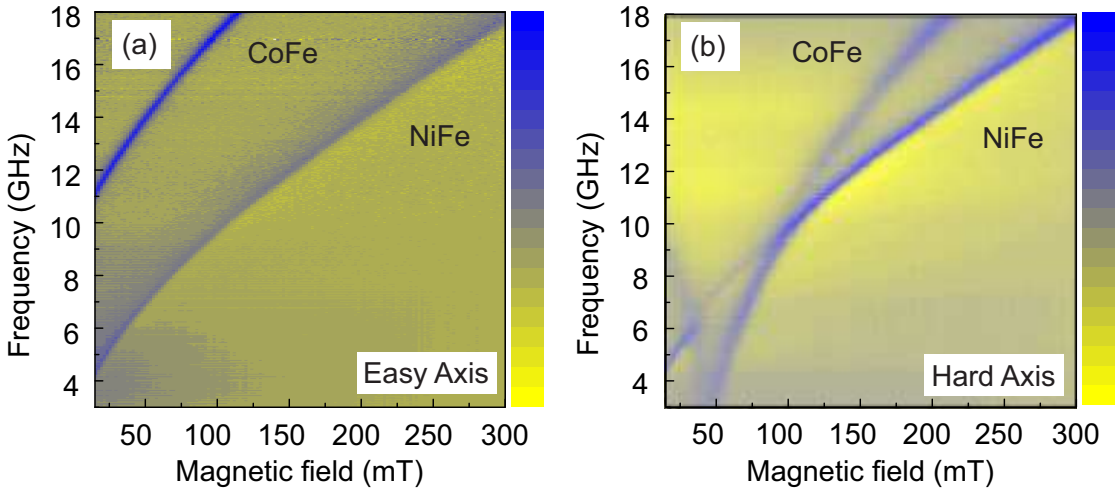


Figure 8.3: Field-frequency transmission maps, showing Kittel curves of two resonances of the $t_{\mathrm{Cr}} = 1$ nm sample with the magnetic field aligned along the easy (a) and hard (b) axis of the CoFe. The isotropic resonance is driven by the NiFe layer, while the anisotropic resonance showing the inflection point on the hard axis is dominated by the CoFe.

static interaction between the two layers.

When $t_{\mathrm{Cr}} = 1.5$ nm the interaction is strongly antiferromagnetic, acting to anti-align the two layers, as shown for field applied along the easy axis of CoFe in Fig. 8.2(c). Consequently, when the CoFe reorients at its coercive field of 8 mT, the NiFe also reverses its direction, thereby preserving the antiparallel alignment. A field of 50 mT is required to force the two layers into parallel alignment. This produces a hysteresis loop with one sharp step at the coercive field of the CoFe, and one curving step as the NiFe rotates. This effect is exacerbated when the magnetic field is applied along the hard axis, as shown in Fig. 8.2(d), wherein the NiFe undergoes a continuous reorientation all the way from the CoFe reversal up to full alignment of the two layers at 80 mT.

VNA-FMR measurements of field-frequency transmission maps are shown in Fig. 8.3(a,b) with the magnetic field applied along the easy and hard axes of the CoFe, respectively. The effects of the magnetocrystalline anisotropy of the CoFe can be seen when the external field is aligned along the hard axis: there is a kink in the Kittel

Layer	t_{Cr} nm	$Kc_{\parallel}$ kJ/m^3	$Ku_{\parallel}$ kJ/m^3	A_{ex} μJ/m^2
$Co_{50}Fe_{50}$	1	45.0 ± 0.1	6.5 ± 0.9	58.2 ± 0.3
	2	37.0 ± 0.2	9 ± 2	3.3 ± 0.6
	5	36.2 ± 0.4	7.9 ± 0.4	31 ± 1
	10	48.5 ± 0.2	7 ± 3	5 ± 1
$Co_{50}Fe_{50}$ reference	0	41.4 ± 0.3	3.0 ± 0.2	N/A
$Ni_{81}Fe_{19}$	1	1.1 ± 0.1	0.17 ± 0.05	58.2 ± 0.3
	2	1.2 ± 0.1	0.7 ± 0.9	3.3 ± 0.6
	5	1.0 ± 0.2	5 ± 2	31 ± 1
	10	2.1 ± 0.2	5 ± 2	5 ± 1
$Ni_{81}Fe_{19}$ reference	0	1.6 ± 0.1	1.9 ± 0.1	N/A

Table 8.1: Magnetocrystalline anisotropy parameters and exchange coupling for the CoFe and NiFe layers of the heterostructures, determined by fitting the angle- and frequency-dependent FMR field for multilayer samples with indicated Cr thicknesses. A_{ex} is a common parameter shared by both layers.

curve at ∼50 mT. By contrast, the NiFe mode appears to be entirely isotropic, with no significant variation in resonance field.

Numerical values for the interlayer exchange coupling, A_{ex} can be determined by fitting the angle- and frequency-dependence of the resonance field using the Kittel equation (2.15), with M_{s} as determined by the SQUID-VSM measurements. The presence of static exchange coupling modifies the LLG, as described in section 2.2.4. The value of the interlayer exchange constant is the same for both layers, but the strength of the exchange field they experience is modified by layer thickness and saturation magnetisation, see equation (2.20). Thus the static exchange interaction has a greater impact on the NiFe than the CoFe. Example results for $t_{\mathrm{Cr}} = 1$ nm are shown in Fig. 8.4(a). The CoFe resonance field varies by ±50 mT, due to its strong magnetocrystalline anisotropy, while the NiFe resonance field has a much weaker variation of ±5 mT, driven by a small magnetocrystalline anisotropy and exchange coupling with the CoFe layer. Figure 8.4(b) shows A_{ex} as a function of t_{Cr}, the expected oscillatory behaviour between FM and AFM coupling is observed [139]. These calculations show that $t_{\mathrm{Cr}} = 2$ nm represents a

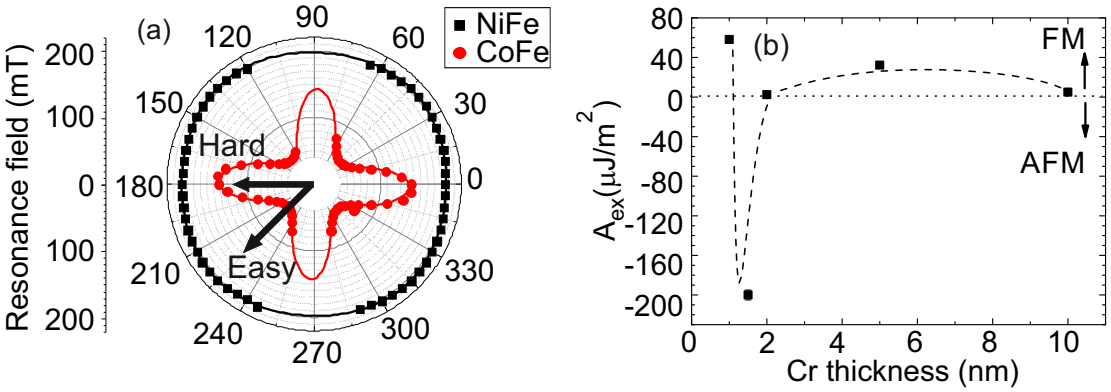


Figure 8.4: (a) Angular dependence of the two resonances at driving frequency 14 GHz. Solid lines are fits to the data using the Kittel equation. (b) Extracted interlayer exchange coupling, A_{ex}, as a function of Cr interlayer thickness, demonstrating the expected transition through AFM coupling before being suppressed for large t_{Cr}. Error bars are comparable to the point size.

transition point, rather than truly uncoupled layers, as there is still an interaction at $t_{\mathrm{Cr}} = 5$ nm.

Table 8.1 shows numerical values for the cubic and uniaxial magnetocrystalline anisotropy parameters, $Kc_{\parallel}$ and $Ku_{\parallel}$, for each layer, and the interlayer exchange constant, A_{ex}. No systematic variation of magnetocrystalline anisotropy as a function of t_{Cr} is observed in either layer.

8.4 Spin Pumping Through a Cr Barrier

With the relation between t_{Cr} and A_{ex} established, it is possible to study the dynamic interaction of spin pumping in more detail. The variation of linewidth as a function of excitation frequency was studied for varying external magnetic field angle, and fitted according to equation (2.21). Fits were performed only at fields above those required to align the magnetisations of the two layers, as confirmed by calculations of the equilibrium orientation of magnetisation, equation (2.11). Further, care was taken to exclude regions where the two modes crossed, to negate

the effect of anti-damping due to simultaneous resonance.

8.4.1 Attenuation of a Pure Spin Current in Cr

Measurements of spin pumping damping as a function of t_{Cr} are shown in Fig. 8.5 for the CoFe and NiFe layers, with the magnetic field applied along the easy axis of the CoFe. A decrease in damping for both layers with increasing Cr thickness is observed, indicative of spin pumping. This arises as spins pumped from the precessing ferromagnetic layer are unable to reach the efficient spin sink of the second FM, instead scattering in the spacer layer or flowing back to the spin source, where they are absorbed and exert an anti-damping torque.

The spin pumping damping is more significant in the NiFe layer, but both layers show the expected exponential drop in spin pumping as the thickness of the interlayer increases. Fits to extract the spin diffusion length were performed using equation (2.27), using the Drude model for the Fermi velocity in Cr ($v_{\mathrm{F}} = 1.56\times10^{-6}$ ms^{-1}), which yields a spin diffusion length of 8 nm. This is somewhat less than the 13 nm reported by Du *et al.* using inverse spin Hall effect measurements [140], but some variation between sample series is to be expected, with the nature of the interfaces and crystallinity of the materials themselves playing a key role. It should be noted that this approach implicitly assumes perfect transmission of spins in the case of a 1 nm Cr barrier, but as it proved impossible to fabricate a continuous Cr layer below this thickness, the data set could not be extended.

8.4.2 Angular Dependence of Spin Pumping

Further information can be obtained by considering the angle-dependence of spin pumping in the Cr spin valves. Figure 8.6 shows the Gilbert damping as a function of t_{Cr} for both layers, measured with the magnetic field applied along the easy and

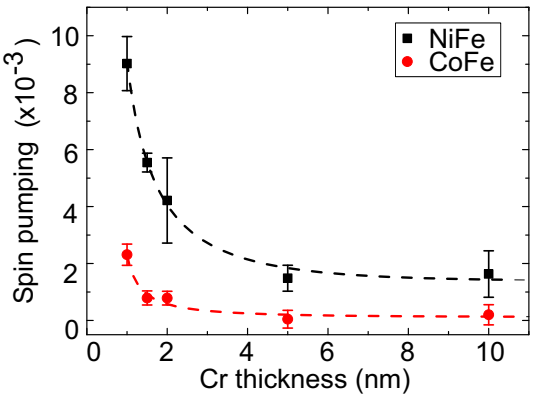


Figure 8.5: Decay of spin pumping with increasing t_{Cr} for the NiFe (black squares) and CoFe (red circles) layers, with the magnetic field applied along the easy axis of the CoFe. Dashed lines are fits to the data using equation (2.27)

hard axes of the CoFe. Figure 8.6(a) shows that damping is anisotropic in the CoFe layer, being significantly higher when the magnetic field is applied along the magnetocrystalline hard axis.

Damping in the NiFe layer [Fig. 8.6(a)] shows a strong anisotropy for low t_{Cr}, however by t_{Cr} = 5 nm the angular variation is significantly reduced, and at t_{Cr} = 10 nm the damping is entirely isotropic, within error. This is rather striking, as a polycrystalline layer should have no preferred orientations and no angular variation of parameters. Furthermore, the anisotropy of damping that develops matches that observed in the CoFe layer, suggesting that the two are linked. This is shown in more detail in Fig. 8.7, plotting the Gilbert damping of both layers as a function of the angle of the applied field with respect to the hard axis of the CoFe. For the thinnest Cr layer there is a strong four-fold anisotropy that correlates with the anisotropy of the CoFe, but as t_{Cr} increases this anisotropy is reduced, moving towards an isotropic damping as would be expected of polycrystalline NiFe. There are several possible explanations for the observed angular variation of damping, including a change in the relative alignment of the two orientations, a modification of the crystal structure of the NiFe with increasing Cr thickness, a transfer of properties mediated by the static interaction, and an anisotropic

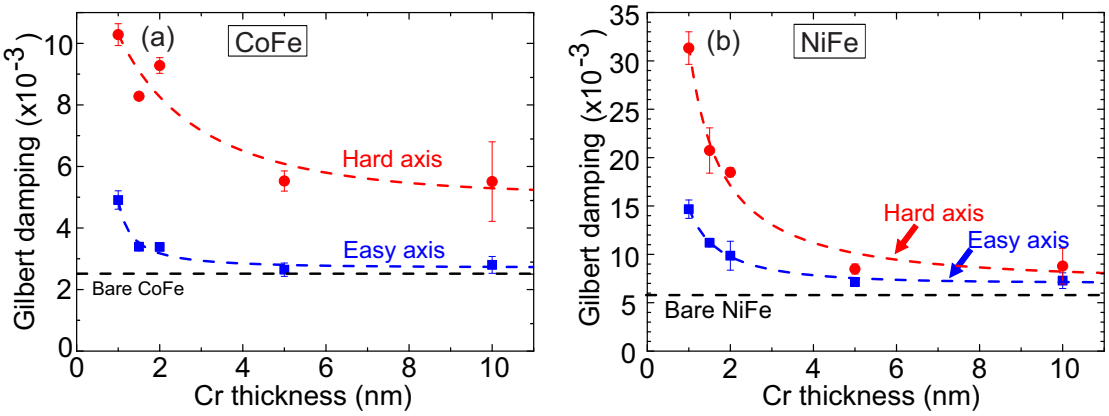


Figure 8.6: Extracted total Gilbert damping for CoFe (a) and NiFe (b) layers, measured along the easy and hard axes of the CoFe layer. A pronounced anisotropy of damping can be observed. Dashed lines are fits to the data using equation (2.27), while the flat line indicates the damping of the bare ferromagnets along the easy axis.

character to spin pumping itself.

If the static magnetisations of the two FM layers are non-collinear, the efficiency of spin pumping is reduced due to increased backflow of spin angular momentum and partial cancellation of damping [141, 145]. This can lead to an in-plane variation of spin pumping, particularly in the case of antiparallel alignment [142,143]. However, in the case of these results, fits to extract α were performed at fields above the anisotropy field of the CoFe, ensuring that the magnetisations of the two layers are collinear. This was confirmed by calculations of the equilibrium orentation of magnetisation from the free energy derivative, using equation (2.11). Another possible source of anisotropic damping was outlined by Timopheev *et al.* [146], whereby a change in the optical/acoustic character of the modes, combined with spin pumping, causes a sharp increase in damping. To exclude this effect, fits to extract α were restricted to the region above the crossing point of the resonances; this also avoids confusion due to anti-damping arising from overlapping resonances [107].

As the decay of anisotropy of damping is tied to increasing Cr thickness, it is also

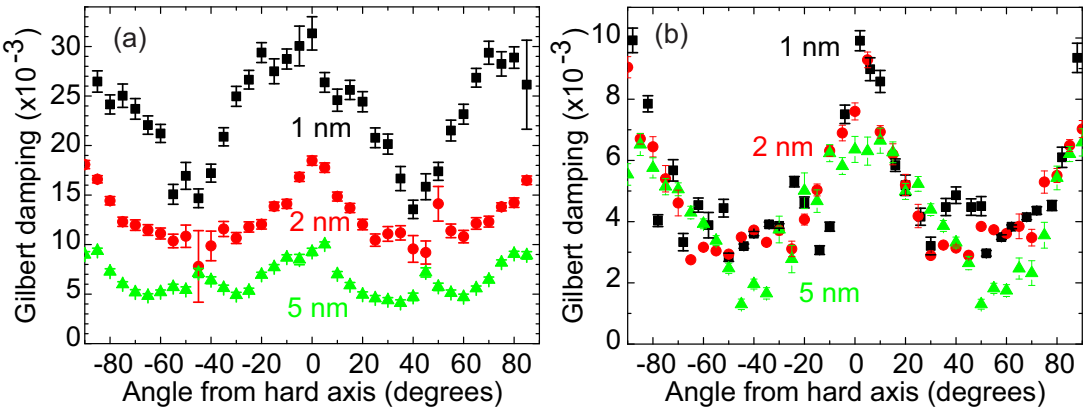


Figure 8.7: Angle-dependent Gilbert damping of the NiFe (a) and CoFe (b) layers as a function of magnetic field angle with respect to the hard axis of the CoFe layer.

possible that the NiFe layer itself is changed by having more Cr beneath it. It might be thought that some of the structural properties of the CoFe base layer could transfer to the NiFe for thin Cr layers, while the samples with thicker Cr remain truly polycrystalline. However, RHEED measurements performed during sample growth confirmed an identical crystal structure in all NiFe layers. Furthermore, as table 8.1 shows, there is no systematic variation of magnetocrystalline anisotropy constants, as would be expected from a change in crystal structure.

When studying such coupled magnetodynamics, the hybridising effects of the static exchange coupling must always be considered, and is therefore a possible source of the observed angular variation. However, the trend in anisotropy of damping as a function of t_{Cr} does not match the trend observed in the static coupling. The damping anisotropy follows a monotonic decrease with increasing t_{Cr}, while A_{ex} changes sign and oscillates over the same range. It is important to note that the damping anisotropy is present for $t_{\mathrm{Cr}} = 2$ nm, where the static exchange coupling is close to zero [$A_{\mathrm{ex}} = (3.3 \pm 0.6) \times 10^{-6}$ J m^{-2}].

These results therefore suggest that the in-plane damping anisotropy of the CoFe layer leads to an anisotropic absorption of the pumped spin current. Transmis-

sion of the spin current at the Cr/CoFe interface is then modified by the same mechanism that leads to anisotropic damping within the CoFe layer. The highest spin pumping damping is achieved when the static magnetisation is aligned with the direction of maximum damping in the CoFe, which in this case matches the magnetocrystalline hard axis. Damping is maximized along the hard axis as most of the pumped spins are absorbed by the CoFe, which acts as a spin sink for the pure spin current ejected from the on-resonance NiFe layer. Along the easy axis, the spin current is partially reflected at the Cr/CoFe interface and returns to the NiFe, where it is re-absorbed and exerts an anti-damping torque on the precessing magnetisation. This raises the possibility of fine control of spin pumping through modification of sink layer damping parameters and engineering of the NM/FM interfaces.

8.5 Layer-Resolved Magnetodynamics

A deeper insight into the anisotropy of damping can be gained by performing layer resolved measurements of precession. XFMR allows determination of not only the spin pumping out of the spin source layer, but also the absorption of the pure spin current by the spin sink layer, through determination of off-resonance precession induced by the spin transfer torque. Further, through modelling of the phase of precession it is possible to separate the effects of static exchange, Gilbert damping and spin transfer torque.

Figure 8.8 shows the layer-resolved amplitude and phase of precession at 4 GHz across the NiFe resonance for $t_{\mathrm{Cr}} = 1$ nm, with the magnetic field applied along the easy axis of the CoFe. The resonance field is at 14 mT, with the expected phase shift of almost 180° across the resonance in the NiFe. The CoFe also shows a weak peak in the amplitude, and a phase shift of approximately 90° across the

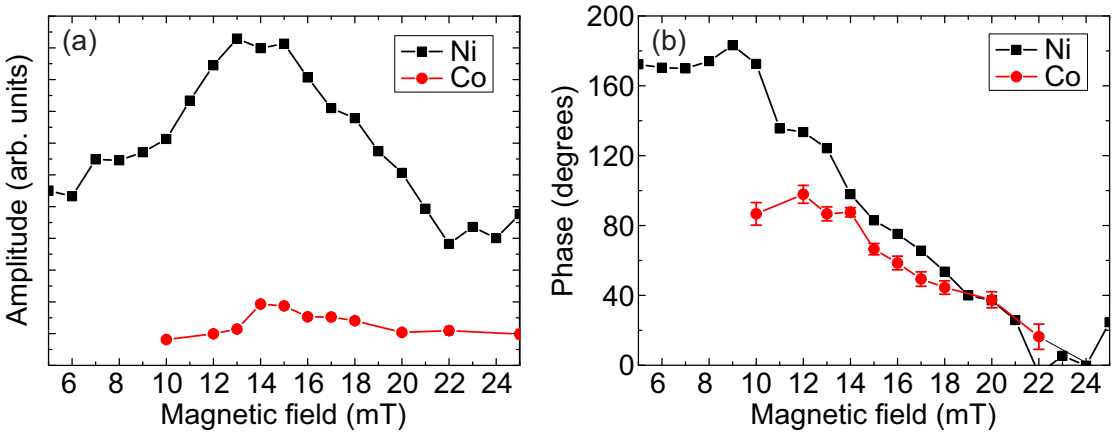


Figure 8.8: Amplitude (a) and phase (b) of precession across resonance at 4 GHz for $t_{\mathrm{Cr}} = 1$ nm, for both layers in the spin valve. The magnetic field is applied along the easy axis of the CoFe.

resonance. This transfer of anisotropy arises from both the static and dynamic exchange couplings across the thin Cr barrier.

As the interlayer exchange constant, A_{ex}, is isotropic, it is possible to study the anisotropy of spin pumping by examining the phase of the induced precession in the CoFe layer as a function of the alignment of the magnetisations of the two layers. As the spin pumping increases as the magnetisation rotates towards the hard axis, the dynamic component of the induced precession should increase, leading to a more bipolar-like feature in the phase. This is studied in Fig. 8.9, showing the phase of the induced precession in the CoFe for magnetisation aligned along the easy, intermediate (22° away from the easy) and hard axes of the CoFe. A significant increase in the curvature of the phase shift is visible from the easy to intermediate axis, indicative of increased spin pumping, and thus increased spin transfer torque. The data along the hard axis is of lower quality due to the geometry of the measurement reducing the effective shortening of the magnetisation vector along the beam, thus reducing the XMCD signal. However, the trend appears to continue, with the phase shift moving towards that expected of a primarily dynamic coupling.

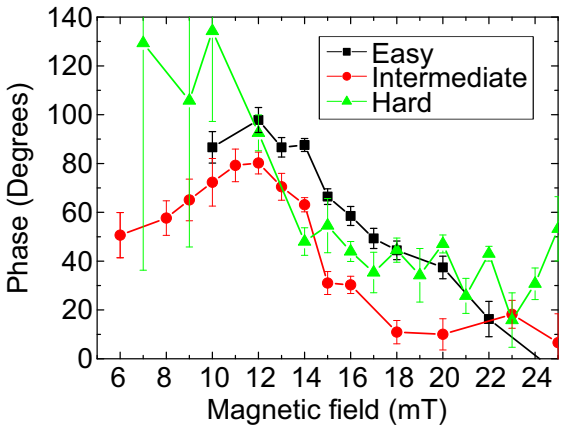


Figure 8.9: Phase of precession of the CoFe magnetisation at 4 GHz, with the magnetisation aligned along the easy, intermediate (22° away from the easy) and hard axes of the CoFe.

The changing character of the net coupling between the two layers can be more rigorously examined by application of the modelling outlined in section 5.3. Figure 8.10 shows the phase of precession across the NiFe resonances at 4 GHz for both the NiFe and CoFe layers, with fits to the data obtained using parameters extracted by fitting of Kittel curves (table 8.1) and damping (Fig. 8.7). By examining precession induced in the off-resonance layer, this approach captures the distinct effects of static exchange, spin pumping, and intrinsic Gilbert damping. As discussed in section 5.3.2, static coupling leads to a unipolar feature in the phase, while dynamic coupling leads to a bipolar feature, while the combination of the two leads to an asymmetric step-like feature; examples are shown in Fig. 8.4(d).

The close agreement with the XFMR data confirms the presence of strongly anisotropic spin pumping, as opposed to increased intrinsic damping, and shows the importance of considering both exchange mechanisms when modelling coupled magnetodynamics. As spin pumping increases the phase shift curvature increases, transitioning from static exchange-dominated unipolar, to dynamic exchange-dominated bipolar. This behaviour is indicative of an increase in STT exerted on the Co moments.

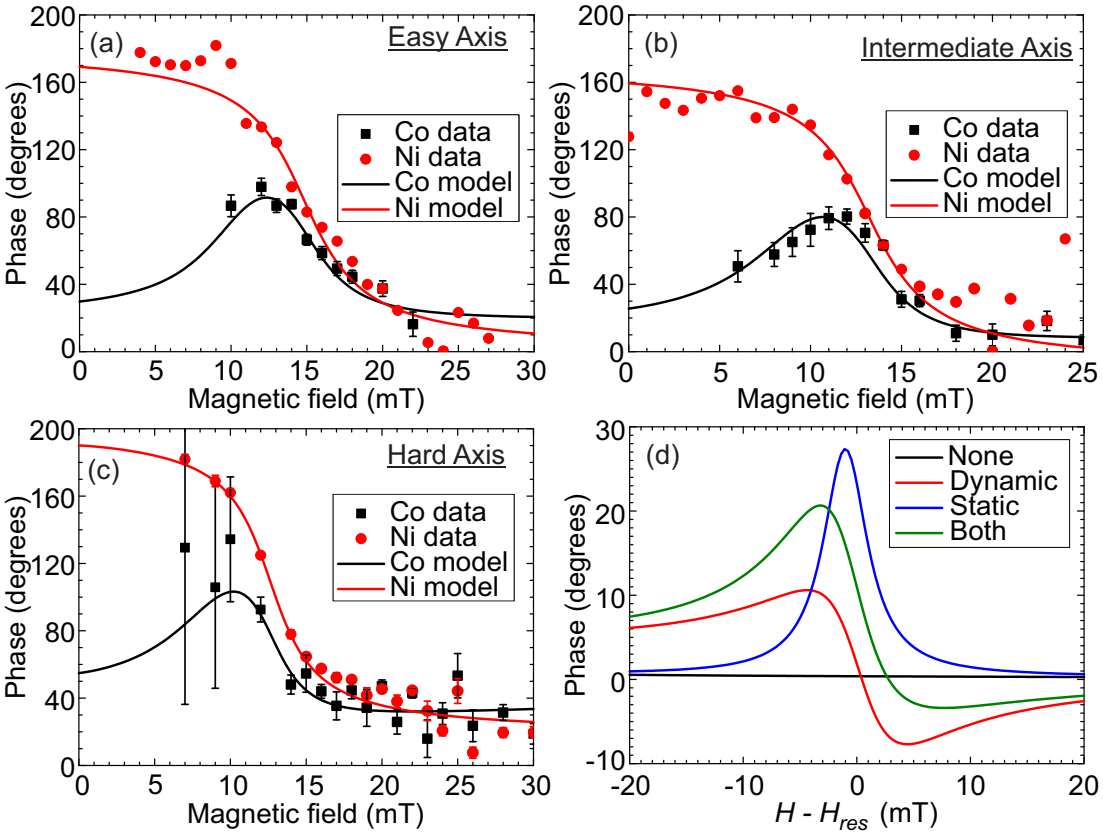


Figure 8.10: Phase of precession for Co (black squares) and Ni (red dots) moments as measured by XFMR for the $t_{Cr} = 1$ nm sample with the bias field along the easy (a), intermediate (22° away) (b) and hard (c) axes of the CoFe layer. Solid lines are model calculations using parameters extracted by fitting of Kittel curves (table 8.1) and damping (Fig. 8.7). (d) Differing effects of static and dynamic exchange on induced precession.

The XFMR results therefore corroborate the VNA-FMR measurements, confirming that spin pumping in effect imprints the anisotropy of damping in the spin sink layer back onto the spin source layer. This can be thought of in terms of the spin sink's ability to absorb the pumped angular momentum being related to its own intrinsic damping. This could be due to partial reflection of the pumped spins at the Cr/CoFe interface, with the spins that are not absorbed travelling back across the Cr layer to exert an anti-damping torque on the NiFe. However, this interpretation must be treated with some caution, as the fact the anisotropy persists to 5 nm would suggest that the reflected spin angular moment has crossed a total distance of 10 nm by the time it is re-absorbed by the NiFe, longer than the

calculated spin diffusion length in Cr. It could be, rather, that the process is more akin to tunnelling magnetoresistance, where the transmission probability from the initial states is determined by the available final states. Further work is required to conclusively determine the origin of this surprising result. Nevertheless, the implications for device optimisation through engineerable anisotropies and tuning of sink layer damping parameters are profound, suggesting several avenues of enquiry through which to further develop the technique of anisotropy imprinting.

8.6 Conclusion

This chapter has presented a multitechnique study of static and dynamic coupling in Cr spin valves, showing how the strength of both interactions can be modified by varying the Cr thickness. The preferred relative orientation can be tuned to aligned (t_{Cr} = 1, 5 nm) or anti-aligned (t_{Cr} = 1.5 nm), while the layers are decoupled for a careful choice of a crossing point between the two regimes, and for suitably thick Cr (t_{Cr} = 2, 10 nm). The dynamic interaction of spin pumping follows the expected exponential decay with increasing Cr thickness, and fits to the data yield a spin coherence length of 8 nm. The most important finding of this investigation, however, is that spin pumping from the polycrystalline NiFe layer is anisotropic, with an in-plane angular dependence that follows the anisotropy of Gilbert damping within the epitaxial CoFe layer. This anisotropy is unaffected by the strength or character of the static exchange coupling, but is suppressed as t_{Cr} exceeds the spin diffusion length in Cr.

This anisotropy imprinting appears to originate in angle-dependent transmission and reflection of spins at the Cr/CoFe interface. XFMR measurements confirm the angular variation of the spin pumping, through measurements of the precession induced in the CoFe layer by on-resonance NiFe. The spin transfer torque exerted

by the pumped spins increases in strength as the magnetisation rotates from the easy axis of the CoFe to the hard axis. Modelling of the data using parameters extracted from VNA-FMR measurements yields good fits to the data, confirming the validity of this interpretation.

These surprising results suggest several routes to further optimise spintronic devices, for example through engineering angular dependence of damping through nanoscale patterning or strain control of magnetocrystalline anisotropy parameters and crystal structure. Further, if modification of the sink layer damping increases the effective spin pumping, techniques such as dilute rare earth doping, as examined in chapter 4, could be used to further increase the efficiency of spin transfer. While a detailed theory of the origin and limitations of the anisotropy imprinting is still lacking, this study makes clear the benefits of a multi-technique, layer-resolved approach to magnetodynamics, and again underlines the importance of high-quality thin films to gain a deep insight into fundamental physical processes. It is hoped that these findings will lead to new concepts in both basic science and practical applications of spin transfer in magnetic multilayers.

Chapter 9

Conclusion

This thesis has presented a study of the magnetoydnamics of thin films and heterostructures, exploring mechanisms by which magnetic relaxation can be modified. Particular attention was paid to the development of angular control of damping, and the role of interfacial couplings. To this end, a multi-technique approach has been employed, combining the lab-based methods of FMR and SQUID-VSM with the synchrotron techniques of XMCD and XFMR. Findings have included the discovery of highly anisotropic damping in Dy-doped Fe, the study of the injection of a pure spin current into a topological insulator and the imprinting of damping anisotropy across a thin Cr barrier. These results have diverse implications for the field of spintronics, as they offer several ways to optimise devices, and shed new light on established spin transfer phenomena. Future work on these topics should travel in two directions, firstly aiming to build on the new understanding of physical phenomena that has been developed and, secondly, working to incorporate the findings into devices with practical applications.

9.1 Summary of Results

Chapter 4 detailed a study of dilute Dy doping of Fe thin films, without loss of crystal quality. The use of rare earth metals as dopants in thin ferromagnetic films has been well-studied over the past decade, and shown to lead to a significant enhancement of Gilbert damping through the mechanism of slow-relaxing impurities. However, there is comparatively little work on high quality samples, and next to no studies have considered the angle-dependence of magnetic relaxation. Here, it was shown that as the Dy content increases from 0.1 % to 5 % the Gilbert damping increases by a factor of 3, and develops a significant anisotropy of damping when comparing the magnetocrystalline easy and hard axes. Application of the XMCD sum rules showed that this change is accompanied by a quenching of the orbital moment, and overall reduction in the ratio of orbital to spin moments. These results provide a demonstration of a method for angular engineering of Gilbert damping, and a further test of the slow-relaxing impurity model for RE-doped FM films.

From chapter 6 the focus shifted from single FM layer to trilayer structures, studying the coupling mechanisms that arise for FM layers separated by a thin NM barrier. $Co_{50}Fe_{50}$/MgO(x)/Ni structures were fabricated by MBE, with $x = 0.5$, 1, 1.5, 2 nm. It was found that the insulating MgO barrier permits a weak static interaction between the two FM layers, but suppresses the dynamic interaction of spin pumping in under 1 nm. SQUID-VSM hysteresis measurements showed the shift from strongly coupled layers switching together to isolated layers switching independently. However, for all but the thinnest barrier no transfer of precessional amplitude was observed, indicating that the static and dynamic behaviour of the layers is rather different.

Chapter 7 studies the spin transfer dynamics of the novel materials class of topo-

logical insulators. In TIs, the large spin-orbit coupling of the bulk leads to a band inversion, and surface states that are topologically protected and robust against backscattering from non-magnetic impurities, making them of great interest for spintronic applications. VNA-FMR studies showed that they have great capacity to absorb angular momentum, in line with other work that has shown they can exert a large spin-orbit torque. However, XFMR found evidence of an interaction between the ferromagnetic layers, across 8 nm of TI, a surprising result, particularly when compared to the results from MgO, or literature studies of insulators and semiconductors. The nature of this interaction was initially unclear, but measurements of the anti-damping torques that arise when both layers are on resonance suggested that a pure spin current is able to persist across the TI barrier. This study was the first of its kind, investigating spin transfer in a TI spin valve architecture, and showcased the rich physics that occurs at the FM-TI interface. That these effects are all observable at room temperature further reinforces the appeal of TIs for device applications.

Chapter 8 combines the twin themes of spin transfer and angular control of magnetodynamics, studying the coupled motion of $Co_{50}Fe_{50}/Cr(t_{Cr})/Ni_{81}Fe_{19}$ trilayers as a function of t_{Cr}. Depending on the barrier thickness, the layers experience a strong ferromagnetic or anti-ferromagnetic coupling, and are completely separated for a sufficiently thick barrier. FMR measurements revealed a significant anisotropy of spin pumping from the NiFe layer, arising from an anisotropy of Gilbert damping in the CoFe layer. This anisotropy is unaffected by the strength or character of the static exchange coupling, but is suppressed as t_{Cr} exceeds the spin diffusion length in Cr, which was found to be 8 nm. A possible explanation for this unexpected effect is anisotropic transmission and reflection of spins at the Cr/CoFe interface. Layer-resolved measurements of induced precession in the CoFe at the NiFe resonance at 4 GHz confirm this observation, revealing the

competition between static and dynamic exchange that occurs in such spin valves. These results shed new light on the increasingly important topic of the anisotropic generation and detection of spin currents. Furthermore, they suggest the possibility of further control of spin pumping through magnetisation alignment, as well as suggesting new concepts to manipulate spin pumping, through modification of the damping mechanisms in the spin sink layer.

9.2 Perspective and Outlook

In reviewing the incidents of this research, though unconscious of intentional omissions, it is nevertheless sensible to consider the suggestions for new studies the findings imply, and their place in the wider field. For example, in the case of Dy-doped Fe films it was found that increasing dopant concentration lead to a quenching of the orbital moment. However, studies on Nd or Gd found the reverse to be true, suggesting that the location of the dopant within the lanthanide series is important, even if they all produce the same effect on the Gilbert damping. This of course merits further study, particularly in the case of Tb, where some of the highest damping enhancements to date has been achieved.

Similarly, the work on spin transfer in TIs represents only the beginning of the effort to understand and functionalise these exciting new materials, bringing them out of the laboratory and into devices. This is currently an area of intense study, in particular magnetotransport studies, so it is anticipated that the field will be unrecognisable in five years, when compared to the snapshot captured here. Future work in this theme should aim to improve the fabrication of such devices, and to explore the effects of using other TI layers, such as Bi_2Te_3 or Sb_2Te_3.

A new thrust in spintronic research is the aim to incorporate antiferromagnets into devices, as their compensated magnetic moments are minimise stray fields

and offer superior thermal stability. Unfortunately, the resonance frequencies of such antiferromagnets are typically on the order of THz, and thus outside the range of the FMR techniques employed here. Synthetic antiferromagnets formed of anti-aligned ferromagnetic layers, however, combine the benefits of natural antiferromagnets with the ease of use of ferromagnets, and can be achieved easily, making them an excellent testbed for such spin transfer phenomena. The antiferromagnetically coupled Cr spin valve presented in chapter 8 is one such synthetic structure, and in itself merits significant further study. Initial XFMR results have shown sharp phase jumps associated with magnetic reversal, and that the precession induced by this coupling is in anti-phase. While these findings are outside the scope of this thesis, they represent a natural extension of the work conducted here, and an excellent lead-in to a new field of research.

Appendix A

Derivation of the AC Magnetic Susceptibility with Static and Dynamic Exchange Coupling

This appendix provides an outline of the derivation of the equations for AC magnetic susceptibility of a structure with two ferromagnetic layers, coupled by both static exchange coupling and dynamic exchange driven by spin pumping. These equations were used to model the amplitude and phase of precession of magnetisation measured by XFMR.

The derivation is based upon the modified form of the LLG equation including spin pumping, as outlined in, for example, Heinrich *et al.* [107] and static exchange, as provided by Arena *et al.* [32]. The derivation itself closely follows that outlined in Appendix 3 of Max Marcham's PhD thesis [35], but does not require that the magnetisation be aligned along a magnetocrystalline easy axis, explicitly including both cubic and uniaxial magnetocrystalline anisotropies.

We consider two ferromagnetic layers, denoted 1 and 2, with magnetic parameters

K^i_{U}, K^i_{C}, M^i_{s}, and γ^i, the in-plane uniaxial and cubic magnetocrystalline anisotropy parameters, saturation magnetisation and gyromagnetic ratio, respectively. The static coupling between the two layers is defined as [31, 32]:

$$\beta_i = \frac{A_{\mathrm{ex}}}{M^i_{\mathrm{s}} d^i} \cos(\phi^i_{\mathrm{M}} - \phi^j_{\mathrm{M}}) \tag{A.1}$$

with d^i the thickness of the magnetic layer.

From this starting point, we write the LLG:

$$\begin{aligned} -\frac{\partial \boldsymbol{m}^i}{\partial t} = \boldsymbol{m}^i \times \left[\gamma^i \boldsymbol{H}^i_{\mathrm{eff}} + \beta^i M^j_{\mathrm{s}} m^j - (\alpha^i_0 + \alpha^i_{ii}) \frac{\partial \boldsymbol{m}^i}{\partial t} \right] \\ + \alpha^i_{ij} \boldsymbol{m}^j \times \frac{\partial \boldsymbol{m}^j}{\partial t}, \end{aligned} \tag{A.2}$$

where superscripts denote magnetic layer, and $\boldsymbol{H}^i_{\mathrm{eff}}$ is the effective field acting on layer i. The intrinsic Gilbert damping is α^i_0, while α^i_{mn} are spin source (m=n) and spin sink ($m \neq n$) terms.

We use the co-ordinate system outlined in Fig. 2.1, a thin film with z oriented out of the plane, external field $\boldsymbol{H}_0$ oriented along x and RF field $\boldsymbol{h}(t)$ oriented along y. Both layers are free (unpinned) with their own cubic and uniaxial magnetocrystalline anisotropy axes, which are not necessarily aligned. All in-plane angles are defined relative to ϕ^1_C. As before, static magnetisations are not necessarily aligned with ϕ_H, their position is instead found by minimizing the free energy. We take the thin film approximation, $N_{xx} = N_{yy} = 0$, $N_{zz} = 1$, and therefore include the demagnetisation field, $H^i_{\mathrm{demag}} = -m^i_z$ as part of the general anisotropy field $\boldsymbol{H}^i_{\mathrm{anis}}$ for simplicity. Finally, we note that for completeness one should also include the imaginary components of the spin mixing conductance, δ_{mn}, but these are typically negligible so are neglected here.

FMR is driven by energy supplied by the effective field, which in this formulation

is written as:

$$\boldsymbol{H}^i_{\text{eff}} = \boldsymbol{H}_0 + \boldsymbol{H}^i_{\text{anis}} + \boldsymbol{h}(t). \tag{A.3}$$

Writing individual components explicitly:

$$\boldsymbol{H}_0 = H_0 \cos(\phi^i_M - \phi_H)\hat{x} \qquad , \tag{A.4}$$

$$\boldsymbol{h}(t) = h(t)\hat{y} \qquad , \tag{A.5}$$

$$\boldsymbol{H}^i_{\text{anis}} = H^i_x\hat{x} + H^i_y\hat{y} + H^i_z\hat{z} \qquad . \tag{A.6}$$

The anisotropy field has components:

$$\begin{aligned} H_x = \frac{K_C}{2M_s^4} \big[& M_x^3(\cos 4(\phi_M - \phi_C) + 3) - 3m_x^2 m_y \sin 4(\phi_M - \phi_C) \\ & + 3m_x m_y^2(1 - \cos 4(\phi_M - \phi_C)) + m_y^3 \sin 4(\phi_M - \phi_C)\big] \\ + \frac{K_U}{M_s^2} & \left[m_x(1 + \cos 2(\phi_M - \phi_U)) - m_y(\sin 2(\phi_M - \phi_U)\right] \end{aligned} \tag{A.7}$$

$$\begin{aligned} H_y = -\frac{K_C}{2M_s^4} \big[& m_x^3 \sin 4(\phi_M - \phi_C) - 3m_x^2 m_y(1 - \cos 4(\phi_M - \phi_C)) \\ & - 3m_x m_y^2(1 + \sin 4(\phi_M - \phi_C)) - m_y^3(\cos 4(\phi_M - \phi_C) + 3)\big] \\ - \frac{K_U}{M_s^2} & \left[m_x(\sin 2(\phi_M - \phi_U) - m_y(1 - \cos 2(\phi_M - \phi_U))\right] \end{aligned} \tag{A.8}$$

$$H_z = -M_{\text{s}} m_z + \frac{2K_C}{M_s^4} m_z^3 \qquad . \tag{A.9}$$

We now re-write the LLG component-wise, calculating the cross products as re-

quired:

$$
\begin{aligned}
-\frac{1}{\gamma^i}\frac{\partial m_x^i}{\partial t} =& m_y^i\left(H_{eff,z}^i + \beta^i M_s^j m_z^j - \frac{\alpha_0^i + \alpha_{ii}^i}{\gamma^i}\frac{\partial m_z^i}{\partial t}\right) \\
& - m_z^i\left(H_{eff,y}^i + \beta^i M_s^j m_y^j - \frac{\alpha_0^i + \alpha_{ii}^i}{\gamma^i}\frac{\partial m_y^i}{\partial t}\right) \\
& - \frac{\alpha_{ij}^i}{\gamma^i}\left(m_y^j\frac{\partial m_z^j}{\partial t} - m_z^j\frac{\partial m_y^j}{\partial t}\right)
\end{aligned} \tag{A.10}
$$

$$
\begin{aligned}
-\frac{1}{\gamma^i}\frac{\partial m_y^i}{\partial t} =& m_z^i\left(H_{eff,x}^i + \beta^i M_s^j m_x^j - \frac{\alpha_0^i + \alpha_{ii}^i}{\gamma^i}\frac{\partial m_x^i}{\partial t}\right) \\
& - m_x^i\left(H_{eff,z}^i + \beta^i M_s^j m_z^j - \frac{\alpha_0^i + \alpha_{ii}^i}{\gamma^i}\frac{\partial m_z^i}{\partial t}\right) \\
& - \frac{\alpha_{ij}^i}{\gamma^i}\left(m_z^j\frac{\partial m_x^j}{\partial t} - m_x^j\frac{\partial m_z^j}{\partial t}\right)
\end{aligned} \tag{A.11}
$$

$$
\begin{aligned}
-\frac{1}{\gamma^i}\frac{\partial m_z^i}{\partial t} =& m_x^i\left(H_{eff,y}^i + \beta^i M_s^j m_y^j - \frac{\alpha_0^i + \alpha_{ii}^i}{\gamma^i}\frac{\partial m_y^i}{\partial t}\right) \\
& - m_y^i\left(H_{eff,x}^i + \beta^i M_s^j m_x^j - \frac{\alpha_0^i + \alpha_{ii}^i}{\gamma^i}\frac{\partial m_x^i}{\partial t}\right) \\
& - \frac{\alpha_{ij}^i}{\gamma^i}\left(m_x^j\frac{\partial m_y^j}{\partial t} - m_y^j\frac{\partial m_x^j}{\partial t}\right)
\end{aligned} \tag{A.12}
$$

At this point, we make the small angle approximation to linearise the equations. As the static magnetisation is aligned along x, and the oscillations about this direction are small, we can rewrite:

$$
\boldsymbol{m} = \hat{x} + m_y(t)\hat{y} + m_z(t)\hat{z} \tag{A.13}
$$

where $m_y(t)$, $m_z(t) \ll M_s$. Note, also, that as m_x is constant in time:

$$
\frac{\partial m_x}{\partial t} = 0\ . \tag{A.14}
$$

Making this linear approximation, we can cancel terms that are nonlinear in $m_y(t)$, $m_z(t)$, $h(t)$:

$$0 = m_y^i(H_{eff,z}^i + \beta^i M_s^j m_z^j) - m_z^i(H_{eff,y}^i + \beta^i M_s^j m_y^j) \tag{A.15}$$

$$\begin{aligned} -\frac{1}{\gamma^i}\frac{\partial m_y^i}{\partial t} =& m_z^i(H_{eff,x}^i + \beta^i M_s^j) \\ &- \left(H_{eff,z}^i + \beta^i M_s^j m_z^j - \frac{\alpha_0^i + \alpha_{ii}^i}{\gamma^i}\frac{\partial m_z^i}{\partial t}\right) \\ &+ \frac{\alpha_{ij}^i}{\gamma^i}\frac{\partial m_z^j}{\partial t} \end{aligned} \tag{A.16}$$

$$\begin{aligned} -\frac{1}{\gamma^i}\frac{\partial m_z^i}{\partial t} =& \left(H_{eff,y}^i + \beta^i M_s^j m_y^j - \frac{\alpha_0^i + \alpha_{ii}^i}{\gamma^i}\frac{\partial m_y^i}{\partial t}\right) \\ &- m_y^i\left(H_{eff,x}^i + \beta^i M_s^j\right) \\ &- \frac{\alpha_{ij}^i}{\gamma^i}\frac{\partial m_y^j}{\partial t} \end{aligned} \tag{A.17}$$

The next step is to expand out the H_{eff}^i terms. This leads to unwieldy expressions, so we define:

$$\begin{aligned} \mathcal{B}_{\text{eff}} =& H_0\cos(\phi_M - \phi_H) + M_s \\ &+ \frac{K_C}{2M_s}\left[3 + \cos 4(\phi_M - \phi_C)\right] + \frac{K_U}{M_s}\left[1 + \cos 2(\phi_M - \phi_U)\right] \end{aligned} \tag{A.18}$$

$$\begin{aligned} \mathcal{H}_{\text{eff}} =& H_0\cos(\phi_M - \phi_H) \\ &+ \frac{2K_C}{M_s}\cos 4(\phi_M - \phi_C) + \frac{2K_U}{M_s}\cos 2(\phi_M - \phi_U) \end{aligned} \tag{A.19}$$

Note that these terms can also be used to write the resonance condition, as dis-

cussed in section 2.2:

$$\left(\frac{\omega}{\gamma}\right)^2 = \mathcal{B}_{\text{eff}}\mathcal{H}_{\text{eff}}|_{H_{\text{res}}} \tag{A.20}$$

evaluated at the resonance frequency. This is equivalent to equation (2.15). With these definitions we expand the H^i_{eff} terms and linearise the results, to yield:

$$\begin{aligned} -\frac{1}{\gamma^i}\frac{\partial m^i_y}{\partial t} =& m^i_z\left[\mathcal{B}_{\text{eff}} + \beta^i M^j_s\right] + \frac{\alpha^i_0 + \alpha^i_{ii}}{\gamma^i}\frac{\partial m^i_z}{\partial t} \\ & -\beta^i M^j_s m^j_z + \frac{\alpha^i_{ij}}{\gamma^i}\frac{\partial m^j_z}{\partial t} \end{aligned} \tag{A.21}$$

$$\begin{aligned} -\frac{1}{\gamma^i}\frac{\partial m^i_z}{\partial t} =& m^i_y\left[\mathcal{H}_{\text{eff}} - \beta^i M^j_s\right] - \frac{\alpha^i_0 - \alpha^i_{ii}}{\gamma^i}\frac{\partial m^i_y}{\partial t} \\ & -\beta^i M^j_s m^j_y + \frac{\alpha^i_{ij}}{\gamma^i}\frac{\partial m^j_y}{\partial t} + h\ . \end{aligned} \tag{A.22}$$

Now we seek harmonic solutions to these equations, using the form $m(t) = m\exp(-i\omega t)$, $h(t) = h\exp(-i\omega t)$:

$$\begin{aligned} 0 =& m^i_z\left(\mathcal{B}_{\text{eff}} + \beta^i M^j_s - (\alpha^i_0 + \alpha^i_{ii})\frac{i\omega}{\gamma^i}\right) \\ & -m^j_z\left(\beta^i M^j_s - \alpha^i_{ij}\frac{i\omega}{\gamma^i}\right) - \frac{i\omega}{\gamma^i}m^i_y \end{aligned} \tag{A.23}$$

$$\begin{aligned} hm^i_s = & -m^i_y\left(\mathcal{H}_{\text{eff}} + \beta^i M^j_s + (\alpha^i_0 + \alpha^i_{ii})\frac{i\omega}{\gamma^i}\right) \\ & +m^j_y\left(\beta^i M^j_s - \alpha^i_{ij}\frac{i\omega}{\gamma^i}\right) + \frac{i\omega}{\gamma^i}m^i_z\ . \end{aligned} \tag{A.24}$$

Thus far we have considered only one layer, so we now exploit symmetry of $i \leftrightarrow j$

interchange to write out the matrix form of the linearised coupled equations:

$$\begin{pmatrix} 0 \\ h \\ 0 \\ h \end{pmatrix} = \begin{pmatrix} -\frac{i\omega}{\gamma^1} & H_{\mathrm{a}}^1 & 0 & H_{\mathrm{c}}^1 \\ -H_{\mathrm{b}}^1 & \frac{i\omega}{\gamma^1} & -H_{\mathrm{c}}^1 & 0 \\ 0 & H_{\mathrm{c}}^2 & -\frac{i\omega}{\gamma^2} & H_{\mathrm{a}}^2 \\ -H_{\mathrm{c}}^2 & 0 & -H_{\mathrm{b}}^2 & \frac{i\omega}{\gamma^2} \end{pmatrix} \begin{pmatrix} m_y^1 \\ m_z^1 \\ m_y^2 \\ m_z^2 \end{pmatrix} \tag{A.25}$$

where:

$$\begin{aligned} H_{\mathrm{a}}^i &= \mathcal{B}_{\mathrm{eff}} + \beta^i M_s^j - (\alpha_0^i + \alpha_{ii}^i)\frac{i\omega}{\gamma^i} \\ H_{\mathrm{b}}^i &= \mathcal{H}_{\mathrm{eff}} + \beta^i M_s^j + (\alpha_0^i + \alpha_{ii}^i)\frac{i\omega}{\gamma^i} \\ H_{\mathrm{c}}^i &= \alpha_{ij}^i \frac{i\omega}{\gamma^i} - \beta^i M_s^j \ , \end{aligned} \tag{A.26}$$

which gives the relation between the microwave field and the magnetisation dynamics:

$$\boldsymbol{h}\boldsymbol{M}_s = \boldsymbol{A}\boldsymbol{m} \ . \tag{A.27}$$

We can therefore see that $\boldsymbol{A}$ is the inverse magnetic susceptibility tensor:

$$\boldsymbol{A}^{-1}\boldsymbol{h}\boldsymbol{M}_s = \boldsymbol{\chi}\boldsymbol{h}\boldsymbol{M}_s = \boldsymbol{m} \ . \tag{A.28}$$

Thus it is possible to calculate desired components of the AC magnetic susceptibility tensor by calculating the inverse of the matrix $\boldsymbol{A}$. This was performed in Python, yielding the complex susceptibility. The amplitude of this complex number is directly proportional to the amplitude of precession of magnetisation, while the phase gives the phase of precession relative to the driving microwave field.

Appendix B

List of of Abbreviations and Acronyms

AC	Alternating Current
AF	Anti-Ferromagnetic (in the context of exchange coupling)
ALS	Advanced Light Source
ARPES	Angle Resolved Photo-Emission Spectroscopy
BiSe	Bi_2Se_3
CB	Conduction Band
CoFe	$Co_{50}Fe_{50}$
CPW	Coplanar Waveguide
DC	Direct Current
DLS	Diamond Light Source
F	Ferromagnetic (in the context of exchange coupling)
FM	Ferromagnet (in the context of a ferromagnetic material or layer)
FMR	Ferromagnetic Resonance
FY	Fluorescence Yield
GMR	Giant Magnetoresistance
HWHM	Half Width Half Maximum
ISHE	Inverse Spin Hall Effect
LaMBE	Lanthanide Molecular Beam Epitaxy (machine)

LIA	Lock In Amplifier
LLG	Landau-Lifshitz-Gilbert (equation)
MBE	Molecular Beam Epitaxy
MSG	Magnetic Spectroscopy Group
MTJ	Magnetic Tunnel Junction
MRAM	Magnetic Random Access Memory
μ-MBE	micro-Molecular Beam Epitaxy (machine)
NiFe	$Ni_{81}Fe_{19}$
NM	Non-Magnetic (in the context of non-magnetic material or layer)
OOMMF	Object-Oriented Micromagnetic Framework [101]
POMS	Portable Octupole Magnet System
QCM	Quartz Crystal Microbalance
RE	Rare Earth
RF	Radio Frequency
RGA	Residual Gas Analyser
RHEED	Reflection High Energy Electron Diffraction
RKKY	Ruderman-Kittel-Kasuya-Yosida (interaction)
SQUID	Superconducting Quantum Interference Device
STT	Spin Transfer Torque
TEY	Total Electron Yield
TI	Topological Insulator
TMR	Tunnelling Magnetoresistance
TSS	Topological Surface State
UHV	Ultra-High Vacuum
VB	Valence Band
VNA	Vector Network Analyser
VSM	Vibrating Sample Magnetometer
XAS	X-ray Absorption Spectroscopy
XFMR	X-ray Detected Ferromagnetic Resonance
XMCD	X-ray Magnetic Circular Dichroism
XRD	X-ray Diffraction

Appendix C

Publications Arising from this Work

The following publications have arisen in full, or in part, as a result of the work conducted over the course of this thesis research.

Anisotropic Absorption of Pure Spin Currents; AA Baker, AI Figueroa, CJ Love, SA Cavill, T Hesjedal, G van der Laan; *Phys. Rev. Lett.* **117** 047201 (2016)

Enhanced Curie temperature of Cr-doped Bi_2Se_3 thin films by magnetic-proximity effect; AA Baker, AI Figueroa, K. Kummer, LJ Collins-McIntyre, G van der Laan, T Hesjedal; *Phys. Rev. B.* **92** 094420 (2015)

Tailoring of magnetic properties of ultrathin epitaxial Fe films by Dy doping; AA Baker, AI Figueroa, G van der Laan, T Hesjedal; *AIP Advances.* **5** 077117 (2015)

Spin pumping in Ferromagnet Topological Insulator Ferromagnet Heterostructures; AA Baker, AI Figueroa, LJ Collins-McIntyre, G van der Laan, T Hesjedal; *Scientific Reports. 5* 7097 (2015)

An ultra-compact, high-throughput molecular beam epitaxy growth system; AA Baker, W Braun, G Gassler, S Rembold, A Fischer, T Hesjedal; *Rev. Sci. Instrum.* **86**, 043901 (2015)

Spin pumping through a topological insulator probed by x-ray detected ferromagnetic resonance; AI Figueroa, AA Baker, LJ Collins-McIntyre, G van der Laan, T Hesjedal; *J. Magn. Magn. Mater.*. **in press** doi:10.1016/j.jmmm.2015.07.013 (2015)

X-ray magnetic circular dichroism on $La_{2/3}Ca_{1/3}Mn_{0.97}Fe_{.03}O_3$ *thin films* AI Figueroa, GE Campillo, AA Baker, JA Osorio, OL Arnache, G van der Laan *Superlattice Microst* **87** 42 (2015)

Study of Dy-doped Bi_2Te_3*: thin film growth and magnetic properties* SE Harrison, LJ Collins-McIntyre, SL Zhang, AA Baker, AI Figueroa, AJ Kellock, A Pushp, SS Parkin, JS Harris, G van der Laan, T Hesjedal *J. Phys.: Condens. Matter* **27** 245602 (2015)

Universal Magnetic Hall Circuit Based on Paired Spin Heterostructures S Zhang, AA Baker, J-Y Zhang, G Yu, S Wang, T Hesjedal; *Adv. Elec. Mater.* **1** 6 (2015)

Modelling ferromagnetic resonance in magnetic multilayers: Exchange coupling and demagnetisation-driven effects; AA Baker, CS Davies, AI Figueroa, LR Shelford, G van der Laan, T Hesjedal; *Journal of Applied Physics* **115** 17D140 (2014)

Three dimensional magnetic abacus memory; S-L Zhang, J Zhang, AA Baker, S Wang, G Yu, T Hesjedal; *Scientific Reports* **4** (2014)

Engineering of BiSe nanowires by laser cutting; P Schönherr, AA Baker, T Hesjedal, P Kusch, S Reich; *EPJ Applied Physics* **66** 10401 (2014)

Magnetic Cr doping of Bi_2Se_3*: Evidence for divalent Cr from x-ray spectroscopy*; AI Figueroa, G van der Laan, LJ Collins-McIntyre, S-L Zhang, AA Baker, SE

Harrison, P Schönherr, G Cibin, and T Hesjedal; *Physical Review B* **90** 134402 (2014)

X-ray magnetic spectroscopy of MBE-grown Mn-doped Bi_2Se_3 thin films; LJ Collins-McIntyre, MD Watson, AA Baker, SL Zhang, AI Coldea, SE Harrison, A Pushp, AJ Kellock, SSP Parkin, G van der Laan and T Hesjedal; *AIP Advances* **4** 127136 (2014)

Study of Gd-doped Bi_2Te_3 thin films: Molecular beam epitaxy growth and magnetic properties; SE Harrison, LJ Collins-McIntyre, S Li, AA Baker, LR Shelford, Y Huo, A Pushp, SSP Parkin, JS Harris, E Arenholz, G van der Laan and T Hesjedal *J. Appl. Phys.* **115**, 023904 (2014)

References

[1] S. A. Wolf, D. D. Awschalom, R. A. Buhrman, J. M. Daughton, S. von Molnar, M. L. Roukes, A. Y. Chtchelkanova, and D. M. Treger, Science **294**, 1488 (2001).

[2] S. A. Wolf, A. Y. Chtchelkanova, and D. M. Treger, IBM J. Res. Dev. **50**, 101 (2006).

[3] M. N. Baibich, J. M. Broto, A. Fert, F. N. Van Dau, F. Petroff, P. Etienne, G. Creuzet, A. Friederich, and J. Chazelas, Phys. Rev. Lett. **61**, 2472 (1988).

[4] G. Binasch, P. Grünberg, F. Saurenbach, and W. Zinn, Phys. Rev. B **39**, 4828 (1989).

[5] S. Yuasa and D. D. Djayaprawira, J. Phys. D: Appl. Phys. **40**, R337 (2007).

[6] J. C. Sankey, Y.-T. Cui, J. Z. Sun, J. C. Slonczewski, R. A. Buhrman, and D. C. Ralph, Nat. Phys. **4**, 67 (2008).

[7] J. A. Katine and E. E. Fullerton, J. Magn. Magn. Mater. **320**, 1217 (2008).

[8] I. L. Prejbeanu, M. Kerekes, R. C. Sousa, H. Sibuet, O. Redon, B. Dieny, and J. P. Nozières, J Phys: Cond. Matt. **19**, 165218 (2007).

[9] J. Slaughter, Annu. Rev. Mat. Res. **39**, 277 (2009).

[10] A. D. Kent and D. C. Worledge, Nat. Nanotechnol. **10**, 187 (2015).

[11] M. D. Stiles and A. Zangwill, Phys. Rev. B **66**, 014407 (2002).

[12] N. Locatelli, V. Cros, and J. Grollier, Nat. Mater. **13**, 11 (2014).

[13] S. Urazhdin, V. E. Demidov, H. Ulrichs, T. Kendziorczyk, T. Kuhn, J. Leuthold, G. Wilde, and S. Demokritov, Nat. Nanotechnol. **9**, 509 (2014).

[14] G. Woltersdorf. *Spin-pumping and two-magnon scattering in magnetic multilayers*. PhD thesis, Simon Fraser University, (2004).

[15] M. K. Marcham, L. R. Shelford, S. A. Cavill, P. S. Keatley, W. Yu, P. Shafer, A. Neudert, J. R. Childress, J. A. Katine, E. Arenholz, N. D. Telling, G. van der Laan, and R. J. Hicken, Phys. Rev. B **87**, 180403 (2013).

[16] G. Woltersdorf and B. Heinrich, Phys. Rev. B **69**, 184417 (2004).

[17] K. Zakeri, J. Lindner, I. Barsukov, R. Meckenstock, M. Farle, U. von Hörsten, H. Wende, W. Keune, J. Rocker, S. S. Kalarickal, K. Lenz, W. Kuch, K. Baberschke, and Z. Frait, Phys. Rev. B **76**, 104416 (2007).

[18] W. Bailey, P. Kabos, F. Mancoff, and S. Russek, IEEE Trans. Magn. **37**, 1749 (2001).

[19] A. A. Baker, A. I. Figueroa, G. van der Laan, and T. Hesjedal, AIP Adv. **5**, 077117 (2015).

[20] A. Brataas, Y. Tserkovnyak, G. E. W. Bauer, and B. I. Halperin, Phys. Rev. B **66**, 060404 (2002).

[21] Y. Tserkovnyak, A. Brataas, and G. E. W. Bauer, Phys. Rev. B **66**, 224403 (2002).

[22] Y. Tserkovnyak, A. Brataas, G. E. W. Bauer, and B. I. Halperin, Rev. Mod. Phys. **77**, 1375 (2005).

[23] B. Kardasz and B. Heinrich, Phys. Rev. B **81**, 094409 (2010).

[24] A. I. Figueroa. *Magnetic Nanoparticles: A Study by Synchrotron Radiation and RF Transverse Susceptibility*. Springer, (2014).

[25] C. H. Du, H. L. Wang, Y. Pu, T. Meyer, P. M. Woodward, F. Y. Yang, and P. C. Hammel, Phys. Rev. Lett. **111**, 247202 (2013).

[26] M. Jamali, J. S. Lee, J. S. Jeong, F. Mahfouzi, Y. Lv, Z. Zhao, B. K. Nikolic, K. A. Mkhoyan, N. Samarth, and J.-P. Wang, Nano Lett. **15**, 7126 (2015).

[27] L. Liu, T. Moriyama, D. C. Ralph, and R. A. Buhrman, Phys. Rev. Lett. **106**, 036601 (2011).

[28] A. A. Baker, A. I. Figueroa, C. J. Love, S. A. Cavill, T. Hesjedal, and G. van der Laan, Phys. Rev. Lett. **116**, 047201 (2016).

[29] D. A. Arena, Y. Ding, E. Vescovo, S. Zohar, Y. Guan, and W. E. Bailey, Rev. Sci. Inst. **80**, 083903 (2009).

[30] A. Azevedo, C. Chesman, S. M. Rezende, F. M. de Aguiar, X. Bian, and S. S. P. Parkin, Phys. Rev. Lett. **76**, 4837 (1996).

[31] G. B. G. Stenning, L. R. Shelford, S. A. Cavill, F. Hoffmann, M. Haertinger, T. Hesjedal, G. Woltersdorf, G. J. Bowden, S. A. Gregory, C. H. Back, P. A. J. de Groot, and G. van der Laan, New J. Phys. **17**, 013019 (2015).

[32] D. A. Arena, E. Vescovo, C.-C. Kao, Y. Guan, and W. E. Bailey, Phys. Rev. B **74**, 064409 (2006).

[33] O. Mosendz, J. E. Pearson, F. Y. Fradin, S. D. Bader, and A. Hoffmann, Appl. Phys. Lett. **96**, 022502 (2010).

[34] J. Goulon, A. Rogalev, F. Wilhelm, N. Jaouen, C. Goulon-Ginet, G. Goujon, J. Ben Youssef, and M. Indenbom, J. Exp. Theor. Phys. **82**, 696–701 (2005).

[35] M. Marcham. *Phase-Resolved Ferromagnetic Resonance Studies of Thin Film Ferromagnets*. PhD thesis, University of Exeter, (2012).

[36] E. Beaurepaire, H. Bulou, L. Joly, and F. Scheurer. *Magnetism and Synchrotron Radiation: Towards the Fourth Generation Light Sources*. Springer, (2013).

[37] G. van der Laan and A. I. Figueroa, Coord. Chem. Rev. **277**, 95 (2014).

[38] G. van der Laan, J. Phys.: Conf. Ser. **430**, 012127 (2013).

[39] P. Carra, B. Thole, M. Altarelli, and X. Wang, Phys. Rev. Lett. **70**, 694 (1993).

[40] B. T. Thole, P. Carra, F. Sette, and G. van der Laan, Phys. Rev. Lett. **68**, 1943 (1992).

[41] G. S. Abo, Y. K. Hong, J. Park, J. Lee, W. Lee, and B. C. Choi, IEEE Trans. Magn. **49**, 4937–4939 (2013).

[42] B. Heinrich and J. A. C. Bland. *Ultrathin Magnetic Structures II: Measurement Techniques and Novel Magnetic Properties*. Springer, (1994).

[43] S. Mizukami, Y. Ando, and T. Miyazaki, Phys. Rev. B **66**, 104413 (2002).

[44] T. L. Gilbert, Phys. Rev. **100**, 1243 [Abstract Only] (1955).

[45] M. Farle, Rep. Prog. Phys. **61**, 755 (1998).

[46] F. Hoffman. *Magnetic anisotropies of (Ga,Mn)As films and nanostructures*. PhD thesis, Universitat Regensburg, (2010).

[47] C. Kittel, Phy. Rev. **73**, 155 (1948).

[48] A. Caprile, A. Manzin, M. Coisson, M. Pasquale, H. W. Schumacher, N. Liebing, S. Sievers, R. Ferreira, S. Serrano-Guisan, and E. Paz, IEEE Trans. Magn. **51**, 1 (2015).

[49] T. A. Ostler, R. Cuadrado, R. W. Chantrell, A. W. Rushforth, and S. A. Cavill, Phys. Rev. Lett. **115**, 067202 (2015).

[50] G. Woltersdorf, M. Buess, B. Heinrich, and C. H. Back, Phys. Rev. Lett. **95**, 037401 (2005).

[51] Y. Tserkovnyak, A. Brataas, and G. E. W. Bauer, Phys. Rev. Lett. **88**, 117601 (2002).

[52] M. Tokaç, S. A. Bunyaev, G. N. Kakazei, D. S. Schmool, D. Atkinson, and A. T. Hindmarch, Phys. Rev. Lett. **115**, 056601 (2015).

[53] T. Chiba, G. E. W. Bauer, and S. Takahashi, Phys. Rev. B **92**, 054407 (2015).

[54] K. Lenz, H. Wende, W. Kuch, K. Baberschke, K. Nagy, and A. Jánossy, Phys, Rev. B **73**, 144424 (2006).

[55] S. S. Kalarickal, P. Krivosik, M. Wu, C. E. Patton, M. L. Schneider, P. Kabos, T. Silva, and J. P. Nibarger, J. Appl. Phys. **99**, 093909 (2006).

[56] B. Heinrich, R. Urban, and G. Woltersdorf, J. Appl. Phys. **91**, 7523 (2002).

[57] Z. Diao, Z. Li, S. Wang, Y. Ding, A. Panchula, E. Chen, L.-C. Wang, and Y. Huai, J. Phys.: Condens. Matter **19**, 165209 (2007).

[58] G. Woltersdorf, M. Kiessling, G. Meyer, J.-U. Thiele, and C. H. Back, Phys. Rev. Lett. **102**, 257602 (2009).

[59] M. K. Marcham, W. Yu, P. S. Keatley, L. R. Shelford, P. Shafer, S. A. Cavill, H. Qing, A. Neudert, J. R. Childress, J. A. Katine, E. Arenholz, N. D. Telling, G. van der Laan, and R. J. Hicken, Appl. Phys. Lett. **102**, 062418 (2013).

[60] A. A. Baker, A. I. Figueroa, L. J. Collins-McIntyre, G. van der Laan, and T. Hesjedal, Sci. Rep. **5**, 7907 (2015).

[61] R. Kukreja, S. Bonetti, Z. Chen, D. Backes, Y. Acremann, J. A. Katine, A. D. Kent, H. A. Dürr, H. Ohldag, and J. Stöhr, Phys. Rev. Lett. **115**, 096601 (2015).

[62] C. Burrowes, B. Heinrich, B. Kardasz, E. A. Montoya, E. Girt, Y. Sun, Y.-Y. Song, and M. Wu, Appl. Phys. Lett. **100**, 092403 (2012).

[63] G. Schütz, M. Knülle, R. Wienke, W. Wilhelm, W. Wagner, P. Kienle, and R. Frahm, Zeitschrift für Physik B Condensed Matter **73**, 67.

[64] C. T. Chen, Y. U. Idzerda, H.-J. Lin, N. V. Smith, G. Meigs, E. Chaban, G. H. Ho, E. Pellegrin, and F. Sette, Phys. Rev. Lett. **75**, 152 (1995).

[65] C. T. Foxon and J. Orton. *Molecular Beam Epitaxy: A Short History.* Oxford University Press, USA, (2015).

[66] B. A. Joyce, Rep. Prog. Phys. **48**, 1637 (1985).

[67] R. Farrow. *Molecular Beam Epitaxy: Applications to Key Materials.* Noyes, (1995).

[68] A. Y. Cho, J. Appl. Phys. **41**, 2780 (1970).

[69] W. P. McCray, Nat. Nanotechnol. **2**, 259 (2007).

[70] J. R. Arthur, Surf. Science **500**, 189 (2002).

[71] M. Henini, editor. *Molecular Beam Epitaxy — From Research to Mass Production.* Elsevier, (2013).

[72] H. Y. Hwang, Y. Iwasa, M. Kawasaki, B. Keimer, N. Nagaosa, and Y. Tokura, Nat. Mater. **11**, 103 (2012).

[73] R. Dingle, A. C. Gossard, and W. Wiegmann, Phys. Rev. Lett. **34**, 1327 (1975).

[74] J. Faure-Vincent, C. Tiusan, E. Jouguelet, F. Canet, M. Sajieddine, C. Bellouard, E. Popova, M. Hehn, F. Montaigne, and A. Schuhl, Appl. Phys. Lett. **82**, 4507 (2003).

[75] F. Katmis, R. Calarco, K. Perumal, P. Rodenbach, A. Giussani, M. Hanke, A. Proessdorf, A. Trampert, F. Grosse, R. Shayduk, R. Campion, W. Braun, and H. Riechert, Cryst. Growth & Design **11**, 4606–4610 (2011).

[76] D. J. Eaglesham, J. Appl. Phys. **77**, 3597–3617 (1995).

[77] W.-X. Ni, J. O. Ekberg, K. B. Joelsson, H. H. Radamson, A. Henry, G.-D. Shen, and G. V. Hansson, J. Cryst. Growth **157**, 285 (1995).

[78] A. A. Baker, W. Braun, G. Gassler, S. Rembold, A. Fischer, and T. Hesjedal, Rev. Sci. Inst. **86**, 043901 (2015).

[79] L. Collins-McIntyre. *Transition-Metal Doped Bi_2Se_3 and Bi_2Te_3 Topological Insulator Thin Films*. PhD thesis, University of Oxford, (2015).

[80] C. Thomas, P. Dudin, and M. Hoesch, Opt. Commun. **359**, 171 (2016).

[81] J.-M. L. Beaujour, A. D. Kent, D. W. Abraham, and J. Z. Sun, J. Appl. Phys **103**, 07B519 (2008).

[82] E. Arenholz and S. O. Prestemon, Rev. Sci. Inst. **76**, 083908 (2005).

[83] A. I. Figueroa, A. A. Baker, L. J. Collins-McIntyre, T. Hesjedal, and G. van der Laan, J. Magn. Magn. Mater. **400**, 178 (2015).

[84] G. Boero, S. Mouaziz, S. Rusponi, P. Bencok, F. Nolting, S. Stepanow, and P. Gambardella, New J. Phys. **10**, 013011 (2008).

[85] S. E. Russek, P. Kabos, R. D. McMichael, C. G. Lee, W. E. Bailey, R. Ewasko, and S. C. Sanders, J. Appl. Phys. **91**, 8659 (2002).

[86] S. G. Reidy, L. Cheng, and W. E. Bailey, Appl. Phys. Lett. **82**, 1254 (2003).

[87] C. Luo, Z. Feng, Y. Fu, W. Zhang, P. K. J. Wong, Z. X. Kou, Y. Zhai, H. F. Ding, M. Farle, J. Du, and H. R. Zhai, Phys. Rev. B **89**, 184412 (2014).

[88] W. Zhang, S. Jiang, P. K. J. Wong, L. Sun, Y. K. Wang, K. Wang, M. P. de Jong, W. G. van der Wiel, G. van der Laan, and Y. Zhai, J. Appl. Phys. **115**, 17A308 (2014).

[89] J. H. Van Vleck and R. Orbach, Phys. Rev. Lett. **11**, 65 (1963).

[90] M. Li, Z. Shi-Ming, M. Jun, and J. Yong, Chin. Phys. B **24**, 017101 (2015).

[91] A. S. van der Goot and K. H. J. Buschow, J. Less-Common Met. **21**, 151 (1970).

[92] C. M. Boubeta, J. L. Costa-Krämer, and A. Cebollada, J. Phys.: Condens. Mater. **15**, R1123 (2003).

[93] H. Song, L. Cheng, and W. E. Bailey, J. Appl. Phys. **95**, 6592 (2004).

[94] Y. Park, E. E. Fullerton, and S. D. Bader, Appl. Phys. Lett. **66**, 2140 (1995).

[95] M. Brockmann, M. Zölfl, S. Miethaner, and G. Bayreuther, J. Magn. Magn. Mater. **198**, 384 (1999).

[96] Q.-F. Zhan, S. Vandezande, K. Temst, and C. van Haesendonck, New J. Phys. **11**, 063003 (2009).

[97] B. H. Clarke, Br. J. Appl. Phys. **18**, 727 (1967).

[98] J. F. Dillon Jr and J. W. Nielsen, Phys. Rev. Lett. **3**, 30 (1959).

[99] A. G. Gurevich, A. N. Ageev, and M. I. Klinger, J. Appl. Phys. **41**, 1295 (1970).

[100] P. S. Keatley, V. V. Kruglyak, A. Neudert, E. A. Galaktionov, R. J. Hicken, J. R. Childress, and J. A. Katine, Phys. Rev. B **78**, 214412 (2008).

[101] M. J. Donahue and D. G. Porter. *Interagency Report NISTIR 6376*. National Institute of Standards and Technology, Gaithersburg, MD.

[102] V. V. Kruglyak, P. S. Keatley, A. Neudert, R. J. Hicken, J. R. Childress, and J. A. Katine, Phys. Rev. Lett. **104**, 027201 (2010).

[103] T. Pramanik, U. Roy, M. Tsoi, L. F. Register, and S. K. Banerjee, J. Appl. Phys. **115**, 17D123 (2014).

[104] A. A. Baker, C. S. Davies, A. I. Figueroa, L. R. Shelford, G. van der Laan, and T. Hesjedal, J. Appl. Phys. **115**, 17D140 (2014).

[105] R. Meckenstock, I. Barsukov, O. Posth, J. Lindner, A. Butko, and D. Spoddig, Appl. Phys. Lett. **91**, 2507 (2007).

[106] T. Moriyama, R. Cao, X. Fan, G. Xuan, B. K. Nikolić, Y. Tserkovnyak, J. Kolodzey, and J. Q. Xiao, Phys. Rev. Lett. **100**, 067602 (2008).

[107] B. Heinrich, Y. Tserkovnyak, G. Woltersdorf, A. Brataas, R. Urban, and G. E. Bauer, Phys. Rev. Lett. **90**, 187601 (2003).

[108] Y. Tserkovnyak, T. Moriyama, and J. Q. Xiao, Phys. Rev. B **78**, 020401 (2008).

[109] J. Xiao, G. E. W. Bauer, and A. Brataas, Phys. Rev. B **77**, 180407 (2008).

[110] J. Ventura, J. M. Teixeira, J. P. Araujo, J. B. Sousa, P. Wisniowski, and P. P. Freitas, Phys. Rev. B **78**, 024403 (2008).

[111] L. Lari, S. Lea, C. Feeser, B. W. Wessels, and V. K. Lazarov, J. Appl. Phys. **111**, 07C311 (2012).

[112] S. G. Wang, R. C. C. Ward, T. Hesjedal, X.-G. Zhang, C. Wang, A. Kohn, Q. L. Ma, J. Zhang, H. F. Liu, and X. F. Han, J. Nanosci. Nanotechnol. **12**, 1006 (2012).

[113] D. L. Li, Q. L. Ma, S. G. Wang, R. C. C. Ward, T. Hesjedal, X.-G. Zhang, A. Kohn, E. Amsellem, G. Yang, J. L. Liu, J. Jiang, H. X. Wei, and X. F. Han, Sci. Rep. **4** (2014).

[114] C. L. Kane and E. J. Mele, Phys. Rev. Lett. **95**, 146802 (2005).

[115] B. A. Bernevig, T. L. Hughes, and S.-C. Zhang, Science **314**, 1757 (2006).

[116] Y. L. Chen, J. G. Analytis, J.-H. Chu, Z. K. Liu, S.-K. Mo, X. L. Qi, H. J. Zhang, D. H. Lu, X. Dai, Z. Fang, S. C. Zhang, I. R. Fisher, Z. Hussain, and Z.-X. Shen, Science **325**, 178 (2009).

[117] Y. L. Chen, J.-H. Chu, J. G. Analytis, Z. K. Liu, K. Igarashi, H.-H. Kuo, X. L. Qi, S. K. Mo, R. G. Moore, D. H. Lu, M. Hashimoto, T. Sasagawa, S. C. Zhang, I. R. Fisher, Z. Hussain, and Z. X. Shen, Science **329**, 659 (2010).

[118] C.-Z. Chang, J. Zhang, X. Feng, J. Shen, Z. Zhang, M. Guo, K. Li, Y. Ou, P. Wei, L.-L. Wang, Z.-Q. Ji, Y. Feng, S. Ji, X. Chen, J. Jia, X. Dai, Z. Fang, S.-C. Zhang, K. He, Y. Wang, L. Lu, X.-C. Ma, and Q.-K. Xue, Science **340**, 167 (2013).

[119] X.-L. Qi, R. Li, J. Zang, and S.-C. Zhang, Science **323**, 1184–1187 (2009).

[120] W.-K. Tse and A. H. MacDonald, Phys. Rev. Lett. **105**, 057401 (2010).

[121] J. R. Williams, A. J. Bestwick, P. Gallagher, S. S. Hong, Y. Cui, A. S. Bleich, J. G. Analytis, I. R. Fisher, and D. Goldhaber-Gordon, Phys. Rev. Lett. **109**, 056803 (2012).

[122] D. Kong, Y. Chen, J. J. Cha, Q. Zhang, J. G. Analytis, K. Lai, Z. Liu, S. S. Hong, K. J. Koski, S.-K. Mo, Z. Hussain, I. R. Fisher, Z.-X. Shen, and Y. Cui, Nature Nanotech. **6**, 705 (2011).

[123] J. E. Moore, Nature **464**, 194 (2010).

[124] M. H. Fischer, A. Vaezi, A. Manchon, and E.-A. Kim, arXiv preprint arXiv:1305.1328 (2013).

[125] Y. Fan, P. Upadhyaya, X. Kou, M. Lang, S. Takei, Z. Wang, J. Tang, L. He, L.-T. Chang, M. Montazeri, G. Yu, W. Jiang, T. Nie, R. N. Schwartz, Y. Tserkovnyak, and K. L. Wang, Nat. Mater. **13**, 699 (2014).

[126] Y. Shiomi, K. Nomura, Y. Kajiwara, K. Eto, M. Novak, K. Segawa, Y. Ando, and E. Saitoh, Phys. Rev. Lett. **113**, 196601 (2014).

[127] T. Yokoyama, J. Zang, and N. Nagaosa, Phys. Rev. B **81**, 241410 (2010).

[128] Z. Ren, A. A. Taskin, S. Sasaki, K. Segawa, and Y. Ando, Phys. Rev. B **82**, 241306 (2010).

[129] C. H. Li, O. M. J. van't Erve, J. T. Robinson, Y. Liu, L. Li, and B. T. Jonker, Nat. Nanotechnol. **9**, 218 (2014).

[130] J. Tian, I. Childres, H. Cao, T. Shen, I. Miotkowski, and Y. P. Chen, Solid State Commun. **191**, 1 (2014).

[131] A. R. Mellnik, J. S. Lee, A. Richardella, J. Grab, P. J. Mintun, M. H. Fischer, A. Vaezi, A. Manchon, E.-A. Kim, N. Samarth, and D. C. Ralph, Nature **511**, 449 (2014).

[132] L. J. Collins-McIntyre, S. E. Harrison, P. Schönherr, N.-J. Steinke, C. J. Kinane, T. R. Charlton, D. Alba-Veneroa, A. Pushp, A. J. Kellock, S. S. P. Parkin, J. S. Harris, S. Langridge, G. van der Laan, and T. Hesjedal, Europhys. Lett. **107**, 57009 (2014).

[133] L. J. Collins-McIntyre, W. Wang, B. Zhou, S. C. Speller, Y. L. Chen, and T. Hesjedal, Phys. Status Solidi B **252**, 1334 (2015).

[134] P. Deorani, J. Son, K. Banerjee, N. Koirala, M. Brahlek, S. Oh, and H. Yang, Phys. Rev. B **90**, 094403 (2014).

[135] Y. Zhang, K. He, C.-Z. Chang, C.-L. Song, L.-L. Wang, X. Chen, J.-F. Jia, Z. Fang, X. Dai, W.-Y. Shan, S.-Q. Shen, Q. Niu, X.-L. Qi, S.-C. Zhang, X.-C. Ma, and Q.-K. Xue, Nature Phys. **6**, 584 (2010).

[136] M. Brahlek, N. Koirala, M. Salehi, N. Bansal, and S. Oh, Phys. Rev. Lett. **113**, 026801 (2014).

[137] G. Wu, H. Chen, Y. Sun, X. Li, P. Cui, C. Franchini, J. Wang, X.-Q. Chen, and Z. Zhang, Sci. Rep **3**, 1233 (2013).

[138] V. Kamberskỳ, Phys. Rev. B **76**, 134416 (2007).

[139] R. Topkaya, M. Erkovan, A. Öztürk, O. Öztürk, B. Aktaş, and M. Özdemir, J. Appl. Phys. **108**, 023910 (2010).

[140] C. Du, H. Wang, F. Yang, and P. C. Hammel, Phys. Rev. B **90**, 140407 (2014).

[141] T. Taniguchi and H. Imamura, Phys. Rev. B **76**, 092402 (2007).

[142] X. Joyeux, T. Devolder, J.-V. Kim, Y. G. De La Torre, S. Eimer, and C. Chappert, J. Appl. Phys. **110**, 063915 (2011).

[143] R. Salikhov, R. Abrudan, F. Brüssing, K. Gross, C. Luo, K. Westerholt, H. Zabel, F. Radu, and I. Garifullin, Phys. Rev. B **86**, 144422 (2012).

[144] J. Lindner, K. Lenz, E. Kosubek, K. Baberschke, D. Spoddig, R. Meckenstock, J. Pelzl, Z. Frait, and D. Mills, Phys. Rev. B **68**, 060102 (2003).

[145] J.-V. Kim and C. Chappert, J. Magn. Magn. Mater **286**, 56 (2005).

[146] A. A. Timopheev, Y. G. Pogorelov, S. Cardoso, P. P. Freitas, G. Kakazei, and N. A. Sobolev, Phy. Rev. B **89**, 144410 (2014).